MBE Growth and Characterization of $Ge_{1-x}Mn_xTe$ Ferromagnetic semiconductors

CHEN WENQIAN

(M. Eng., Tianjin University, P. R. China)

A THESIS SUBMITTED

FOR THE DEGREE OF DOCTOR OF PHILOSOPHY

DEPARTMENT OF ELECTRICAL & COMPUTER ENGINEERING

NATIONAL UNIVERSITY OF SINGAPORE

2008

Acknowledgement

I would like to take this opportunity to express my sincere gratitude and appreciation to my supervisors A/P Teo Kie Leong, A/P Thomas Liew and A/P Mansoor Abdul Jalil. I would like to thank A/P Teo Kie Leong for his kind and consistent concern, support and guidance in the project and also all the valuable discussion on the experimental results. I am also grateful to A/P Thomas Liew and A/P Mansoor Abdul Jalil for their valuable advices for the project analysis.

I am also grateful to be in a caring, supportive and cooperative research team. I thank Mr. M. G. Sreenivasan, Mr. Ko Viloane, Ms. Hou Xiu Juan, Mr. Lim Sze Ter, Miss. Sim Cheow Hin, and Mr. Bi Jing Feng for their support and help in this project. I would like to thank Seng Ghee, Randall, Sunny, Yingzi, Saurabh, Jon, Jaron, Zhen Zhou and the whole Spintronic group for the valuable discussion and all the fun.

I would like to express my appreciation for all the staffs in DSI and ISML for their help in carrying out the experiments, especially to Ms. Loh Fong Leong, Mr. Alaric Wong, Ms Tan Bee Ling, Mr. Zhao Haibao, Dr. Song Wendong, Dr Guo Zaibing and Mr. Chong Joon Fatt. I would like to thank the students, Mr Li Hongliang, Mr Liu Tie and Mr. Wang Hao Ming, who have helped me even in their busy study.

Last but not least, I would like to thank all of friends and my family for their supports during my Ph.D study period.

Table of Contents

Summary

Diluted magnetic semiconductor (DMS) has attracted considerable attention recently since its important applications in the field of spintronics. It is generally believed that free charge carriers in the semiconductor host mediate the interaction between magnetic ions, therefore to cause the ferromagnetism in DMS. In contrary to III–V and II-VI based DMS which have been popularly studied, the investigation of the IV-VI based DMS is relatively less so far. In this work, we focus on understanding of the origin of ferromagnetism in $Ge_{1-x}Mn_xTe$ material.

We attempt to fabricate the $Ge_{1-x}Mn_xTe$ ferromagnetic semiconductor on BaF_2 (111) substrate by solid-source molecular-beam epitaxy. The growth conditions are optimized by the the flux ratio of Te/Mn and Te/Ge and the growth temperature. The $Ge_{1-x}Mn_xTe$ films with composition range of $0.14<x<0.98$ are successfully grown. The X-ray diffraction provides the clear evidence that the grown $Ge_{1-x}Mn_xTe$ films crystallize in the NaCl phase with (111) orientation preferred for all x. No secondary phases are observed from the XRD measurement. However, the HRTEM results show that the non-uniformity exists in the film, which indicate the samples are not homogeneous and may contain clusters or grains with different sizes and compositions. The optical absorption measurement shows that the band-gap of magnetic semiconductor $Ge_{1-x}Mn_xTe$ with $0.14<x<0.98$ in a manner qualitatively similar to the nonmagnetic semiconductor counterpart GeTe and MnTe.

We also investigate the magnetic and transport properties of the $Ge_{1-x}Mn_xTe$. The dependence of Curie temperature T_C on x tends to follow a quadratic behavior. This phenomenon can be attributed to the increase of antiferromagnetic interaction since MnTe is an antiferromagnet. The highest T_C is achieved around 150 K at x=0.55. The carrier concentration of $Ge_{1-x}Mn_xTe$ films are in the range of 1×10^{20} cm^{-3} to 1×10^{22} cm^{-3}. The observed Anomalous Hall effect of $Ge_{1-x}Mn_xTe$ thin film is the combination of the carrier-induced ferromagnetism with the effect of the clusters, which is ascribed to extrinsic skew scattering. The temperature-dependent resistivity measurement exhibits an upturn at low temperature which can be related to the ferromagnetic transition. The resistivity and M-T behaviors can be attributed to weak localization effect of disordering. The magnetoresistance (MR) of $Ge_{1-x}Mn_xTe$ displays very clear hysterestic loop at low temperature which reseumbles that of giant-magnetoresistance (GMR) granular system in solids. The negative MR behaviors may be accounted for the bound magnetic polaron (BMPs) model. We correlate the observation of the isotropy of MR and M-H curves with the formation of $Ge_{1-x}Mn_xTe$ FM clusters embedded in GeTe matrix.

List of Figures

List of Tables

CHAPTER 1 INTRODUCTION

1.1 Background

In current semiconductor technology, the current conduction in a semiconductor occurs via free electrons and holes, is collectively known as charge carriers. The applications of the semiconductor materials such as Si and GaAs range from the integrated circuits (IC) [1], solar cell and light emitting diodes (LED) [2]. On the other hand, ferromagnetic devices have been developed utilizing the electron spin of the magnetic materials. The devices applications include read heads, hard drives, solenoid switches and sensors etc. However, only the spin of the electrons in metallic 3d transition elements such as Fe, Co, Ni and compound magnets such as ferrite magnet (Fe_3O_4) [3] and rare earth magnet ($Nd_2Fe_{14}B$) [4] have been investigated. It is quite natural to ask whether the charge and spin of electrons can be used together to further enhance the performance of the devices. For this reason, the new field of spintronics has emerged with the discovery of Giant Magnetoresistance (GMR) in 1988 [5]. In this technology, both the electron charges and the spins are utilized to carry information, and this offers an opportunity to initiate a new generation of devices which combine the standard microelectronics with the spin-dependent effects that arise from the interaction between spin of the carrier and magnetic properties of the materials. For instance, spin-FET (field effect transistor), spin-LED (light-emitting diode), spin-RTD (resonant tunneling device), optical switches operating at terahertz frequency, and quantum bits for quantum computation and communications have

stimulated tremendous interest in this rapidly growing field. Spintronics hold great promises, bring about the possibility of non-volatility, increased processing speed, decreased power consumption, and also increased transistor density compared to conventional semiconductor devices [6].

Spintronics is a very broad field in which the GMR-based electronics or magnetoelectronics and semiconductor-based spintronics are two main research directions. Although the development of GMR-based spintronics devices have made great progress recently, the lack of the ability in charge control of the ferromagnetic material layers limits their further applications. Moreover, the spin injection efficiency can be affected by the conductivity mismatch at the metal/semiconductor interfaces and connections, not to mention problems that may arise from stray electromagnetic radiation or heat dissipation [7, 8]. This ultimately led to the research and development of a new type of material called ferromagnetic semiconductors which combine the magnetic and semiconducting properties in one material.

The research on the ferromagnetic semiconductors started back in the 1960s and early 1970s. The initial stage of the ferromagnetic semiconductor research focuses on the materials which have both ferromagnetic and semiconducting properties, with a periodic array of magnetic elements. Examples are semiconducting spinels and europium chalcogenides [9]. However, these materials are not suitable for spintronics application since they have low Curie temperature and poor semiconducting transport properties.

In 1996, Ohno and co-workers discovered that Mn doped GaAs was ferromagnetic

with a Curie temperature of 110K [10]. DMSs refer to the semiconductors, in which the cation sites of the host semiconductors are substituted by the transition magnetic ions. It was demonstrated that the material must have p-type conductivity to possess ferromagnetic behavior. This led authors to infer that the ferromagnetism was hole (carrier) induced, which make it possible to control the magnetism electrically or optically through the field-gating of transistor or optical excitation to alter the carrier density. Recently, several breakthroughs have been achieved based on (In, Mn)As and (Ga, Mn)As, including electrical-field controlled magnetization [11], spin injection [12], current-induced domain-wall switching [13] and optical control of magnetization [14].

Although the applications based on the (In, Mn)As and (Ga, Mn)As DMS have been made lot of progress, the highest Curie temperature of GaMnAs and InMnAs are ~170K [15] and ~50K [16] only, which make the device only be able to operate in the cryostate. The search for DMS with high Curie temperature is thus a very attractive area in spintronics research. A theoretical prediction by Dietl et al. [17] demonstrated that the Curie temperature can be realized above room temperature in some p-type DMS as shown in Fig. 1-1. Great efforts have been devoted to the synthesis and characterization of different types of DMS materials. Although room temperature ferromagnetism has been reported in many systems, such as GaN:Mn [18] GaN:Cr [19] TiO_2:Co [20] ZnO:Co [21] $CdGeP_2$:Mn [22] and ZnO:Mn [23] and the reported T_C can be as high as 940K [24]; those results are not well-verified because the existence of ferromagnetic precipitates cannot be possibly ignored. The research of

the DMSs material range from the III-V, II-VI, IV-VI, IV, oxides based and nitride based semicondutors etc. In most of the DMSs, transition metals (TM) that have partially filled d states (Sc, Ti, V, Cr, Mn, Fe, Co, Ni, and Cu) and rare earth elements that have partially filled f states (Eu, Gd and Er etc.) have been used as magnetic atoms. The partially filled d states or f states contain unpaired electrons, in terms of their spins, which are responsible for them to exhibit ferromagnetic behaviors. DMS holds great interests in the field of spintronic applications due to the fact that it offers a possibility of studying the magnetic phenomena in crystals with a simple band structure and excellent magneto-optical and transport properties. It is also possible to tune the magnetic properties of DMS not only by an external magnetic field but also by varying the band structure and/or carrier, impurity and magnetic ion concentrations.

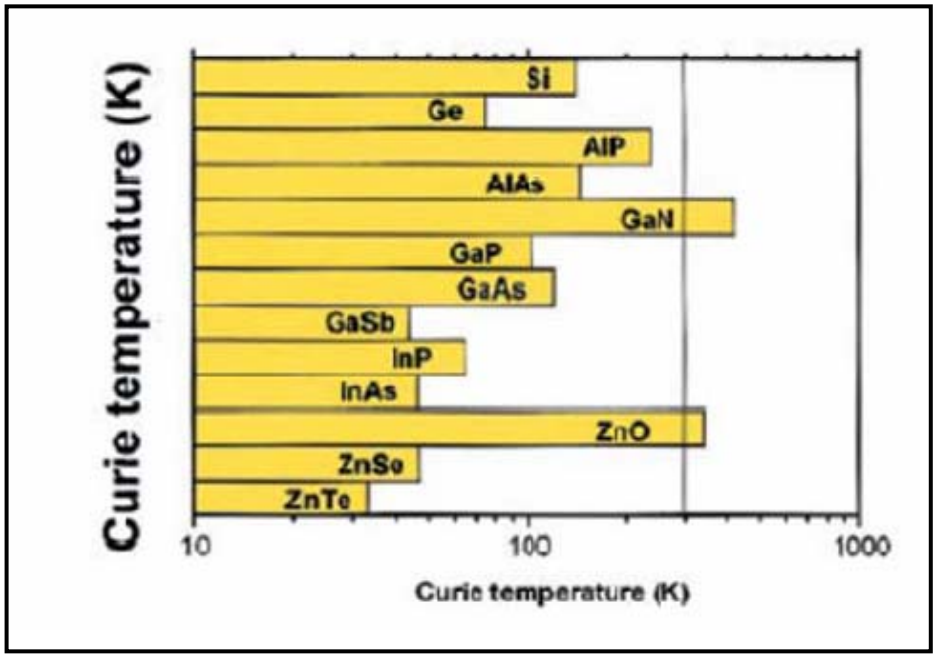

Figure 1-1 Compound values of the Curie temperature Tc for various p-type semiconductors containing 5% of Mn and 3.5×10^{20} holes per cm^{-3} [Ref. 17].

1.2 Research motivation

As mentioned above, DMS has attracted considerable attention recently because of its important applications in the field of spintronics. It is generally believed that free charge carriers in the semiconductor host mediate the interaction between magnetic ions [17,25,26], at least in II-VI and III–V based DMS doped with Mn [10,27,28]. In contrary to III–V semiconductors which have been popularly studied, the investigation of the IV-VI based DMS is relatively less so far. Only a few compounds are reported to have ferromagnetic ordering among the transition metal doped IV-VI semiconductors. For example, the highest T_C reported so far for Mn doped SnTe [29] and PbSnTe [30] are 4 K and 6 K, respectively. Specifically, It has been reported that $Ge_{1-x}Mn_xTe$ (x~0.51) exhibits a relatively high T_C ~ 150 K and 140 K for bulk sample [31] and for thin film [32], respectively. Recently, there is also a report of T_C > 200 K on MBE grown $Ge_{0.66}Mn_{0.34}$ single layer and superlattice consisting of 40 × [86 nm $Ge_{0.68}Mn_{0.32}Te$ / 0.5 nm MnTe] [33]. Thus, $Ge_{1-x}Mn_xTe$ seems to be a good IV-VI DMS candidature to realize relatively high Curie temperature. This is our first motivation.

In DMS system, the magnetic transition metal may not thermodynamically stable in the semiconductor host and tends to segregate [34]. For many semiconductor materials, the bulk solid solubility for magnetic or electronic dopants is not favorable for the coexistence of carriers and spins in high densities. Thus, a key aspect in the DMS work is to achieve soluble concentrations of the transition-metal ions well above the equilibrium solubility limit. In this sense, IV-VI ferromagnetic $Ge_{1-x}Mn_xTe$ can

serve as an interesting model to study ferromagnetism due to its high solubility limit of more than 95% Mn can be incorporated into the GeTe host lattice [35]. Generally, the preparation methods such as molecular beam epitaxy (MBE) are under the nonequilibrium condition. It is possible to enhance the solubility limit of magnetic ions in semiconductors under the nonequilibrium growth condition. MBE also has the unique advantage that the growth occurs under ultra high vaccum conditions. Thus the background concentration of gases such as O_2, H_2O, and CO is very low. Moreover, the very high degree control of the growth condition can also lead to very abrupt changes in composition. While ionized-cluster beam [32, 35] and rf sputtering techniques [36] have been widely used, there are only a few attempts to grow $Ge_{1-x}Mn_xTe$ using the molecular-beam epitaxy (MBE) technique [33, 37]. To fabricate the $Ge_{1-x}Mn_xTe$ thin films using MBE technique is our second motivation.

IV–VI compounds also can offer a good opportunity to study ferromagnetic properties in DMS since magnetic ions and the carrier concentration can be introduced and controlled independently. It is well known that crystalline GeTe is a narrow band-gap (0.1 to 0.2 eV) degenerate semiconductor with a high carrier concentration $\left(10^{20}-10^{21}\,\mathrm{cm}^{-3}\right)$ resulting from the presence of both Ge vacancy and Ge-Te disorder type of defects [38, 39]. Consequently, it is possible to control the carrier concentrations by changing the stoichiometric composition. On this basis, Fukuma *et al.* [40] has shown that it is possible to control the carrier concentrations by changing the stoichiometric composition.

So far, the correlation between the magnetic properties and carrier concentrations

in III-V DMS is not fully understood. For instance, Mn acts as an acceptor in $Ga_{1-x}Mn_xAs$ [41], so that in $Ga_{1-x}Mn_xAs$ Mn ions bring both the carriers and the localized spins. Therefore, this material appears to be difficult for systematic study of the dependence of the magnetic property on the carrier concentration experimentally. However, in IV-VI material such as $Ge_{1-x}Mn_xTe$, since Mn ions are incorporated into GeTe host as electrically neutral Mn^{2+} [31], it offers a good opportunity to study the correlation between magnetic properties and carrier concentrations. This is our third motivation.

1.3 Objectives

The objectives of this project are summarized as follows:

The first objective is to deposit the $Ge_{1-x}Mn_xTe$ thin films by MBE. MBE is a novel approach for the GeTe based ferromagnetic semiconductor growth. In MBE technique, the films can be grown under the nonequilibrium conditions. Thus it is possible to enhance the solubility limit of magnetic ions in semiconductor hosts. In addition, MBE allows the high degree control of the growth rate and composition. We will make use of MBE growth technique to investigate systematically the influence of the controllable growth parameters on the film properties.

The second objective is to characterize the structural, magnetic and electrical properties of $Ge_{1-x}Mn_xTe$ thin films. A DMS system should possess both the semiconductor and magnetic behavior. To verify the crystal properties of the films, the reflection high-energy electron diffraction (RHEED), X-ray diffraction (XRD) and

high-resolution transmission electron microscopy (HRTEM) are employed. X-ray photoelectron spectroscopy (XPS) and optical absorption spectra are used to analyze the compostion and optical band-gap of the materials, respectively. To determine the magnetic properties, commercial super-conducting quantum interference device (SQUID) is used. Hall effect, temperature-dependent resistivity (R-T), anomalous hall effect (AHE) and magnetoresistance (MR) measurements are conducted to determine the transport properties of the films.

The third objective is to investigate the ferromagnetism mechanism of $Ge_{1-x}Mn_xTe$ thin films. It is necessary to provide some understanding for the magnetic behaviours of $Ge_{1-x}Mn_xTe$ thin films since there is no consensus on the origin of ferromagnetism yet. Our studies aimed to answer some of the following unsettled questions in the $Ge_{1-x}Mn_xTe$ system: (i) How do the Mn compositions affect the magnetic properties of the films? (ii) Are there any precipitates or clusters can be observed from the structural analysis which indicates disordering and what are their roles of affecting the ferromagnetic properties? (iii) Are the films semiconducting, metallic or insulating, and what is the behavior of the transport properties?

1.4 Organization of thesis

The outline of the thesis is as follows:

Chapter 1 gives a brief introduction to spintronics materials research area. Some theoretical background about the DMS is provided. The current issues of GeTe based DMS materials are discussed. The motivation and the objectives of the research are also highlighted in the chapter.

Chapter 2 provides the review of the theoretical background of the ferromagnetism mechanisms in DMS. The literature review of the DMS family is given. The research work done on GeMnTe DMS is also summarized.

Chapter 3 describes the MBE experimental procedures used in this project, including the MBE system set-up, samples preparations and flux control of the cell sources.

Chapter 4 gives an overview of the tools used for structural, magnetic and transport characterization of our samples. The experimental equipments and setup are also discussed.

Chapter 5 presents the results and discussion on the structural and optical properties of $Ge_{1-x}Mn_xTe$ films. The growth conditions of the MBE growth of $Ge_{1-x}Mn_xTe$ films ($0.14<x<0.98$) are discussed and a suggestion of an optimum experimental condition for synthesizing the $Ge_{1-x}Mn_xTe$ thin films is provided.

Chapter 6 presents the results and discussion of the magnetic and transport properties of $Ge_{1-x}Mn_xTe$ films. We investigate the ferromagnetic properties through the magnetic and transport measurement of the films. The ferromagnetic ordering can be realized for $Ge_{1-x}Mn_xTe$ deposited with $0.14<x<0.98$.

Last but not the last, chapter 7 gives the conclusions by summarizing the main results obtained in the work and recommendations for the future work is also given.

References:

[1] B. G. Streetman, Solid state electronic devices, 4th ed. (Prentice Hall,

Englewood Cliffs, N.J.,1995).

[2] S. Nakamura, G. Fasol, and S. J. Pearton, The blue laser diode: the complete story, 2nd updated and extended ed. (Springer, Berlin; London, 2000).

[3] http://en.wikipedia.org/wiki/Ferrite_(magnet)

[4] http://en.wikipedia.org/wiki/Rare-earth_magnet

[5] M. N. Baibich, J. M. Broto, A. Fert, F. N. Van Dau, F. Petroff, P. Eitenne, G. Greuzet, A. Friederich, and J. Chazelas, "Giant Magnetoresistance of (001)Fe/(001)Cr Magnetic Superlattices", Phys. Rev. Lett., **61**, 2472 (1988).

[6] S. A. Wolf, D. D. Awschalom, R. A. Buhrman, J. M. Daughton, S. Von Molnar, M. L. Roukes, A. Y. Chtchelkanova and D. M. Treger, "Spintronics: A spin-based electronics vision for the future", Science, **294**, 1488 (2001)

[7] S. Gardelis, C. G. Smith, C. H. W. Barnes, E. H. Linfield, and D. A. Ritchie, "Spin-valve effects in a semiconductor field-effect transistor: A spintronic device", Phys. Rev. B, **60,** 7764 (1999).

[8] P. R. Hammar, B. R. Bennet, M. J. Yang, and M. Johnson, "Observation of Spin Injection at a Ferromagnet-Semiconductor Interface", Phys. Rev. Lett., **83,** 203 (1999).

[9] A. Mauger and C. Godart, "The Magnetic, Optical, and Transport-Properties of Representatives of a Class of Magnetic Semiconductors-The Europium Chalcogenides", Phys. Rev., **141,** 51 (1986).

[10] H. Ohno, A. Shen, F. Matsukura, A. Oiwa, A. Endo, S. Katsumoto, and Y. Iye, "(Ga,Mn)As: A new diluted magnetic semiconductor based on GaAs", Appl. Phys.

Lett., **69,** 363 (1996).

[11] H. Ohno, D. Chiba, F. Matsukura, T. Omiya, E. Abe, T. Dietl, Y. Ohno, and K. Ohtani, "Electric-field control of ferromagnetism", Nature, **408**, 944 (2000).

[12] Y. Ohno, D. K. Young, B. Beschoten, F. Matsukura, H. Ohno, and D. D. Awschalom, "Electrical spin injection in a ferromagnetic semiconductor heterostructure", Nature, **402**, 790 (1999).

[13] M. Yamanouchi, D. Chiba, F. Matsukura, and H. Ohno, "Current-induced domainwall switching in a ferromagnetic semiconductor structure", Nature, **428**, 539 (2004).

[14] S. Koshihara, A. Oiwa, M. Hirasawa, S. Katsumoto, Y. Iye, C. Urano, H. Takagi, and H. Munekata, "Ferromagnetic order Induced by photogenerated carriers in magnetic III-V semiconductor heterostructures of (In,Mn)As/GaSb", Phys. Rev. Lett., **78**, 4617 (1997).

[15] K. Y. Wang, R. P. Campion, K. W. Edmonds, M. Sawicki, T. Dietl, C. T. Foxon, and B. L. Gallagher, AIP conf. proceedings, Melville, New York, **772**, 333 (2005).

[16] H. Munekata, H.Ohno, S. von Molnar, A. Segmuller, L. L. Chang, and L. Esaki, "Diluted magnetic III-V semiconductors", Phys. Rev. Lett., **63,** 1849 (1989).

[17] T. Dietl, H. Ohno, F. Matsukura, J. Cibert, and D. Ferrand, "Zener model description of ferromagnetism in Zinc-Blende magnetic semiconductors", Science, **287**, 1019 (2000).

[18] M. L. Reed, N. A. El-Masry, H. H. Stadelmaier, M. K. Ritums, M. J. Reed, C. A. Parker, J. C. Roberts, and S. M. Bedair, "Room temperature ferromagnetic properties

of (Ga, Mn)N", Appl. Phys. Lett., **79**, 3473 (2001).

[19] S. E. Park, H. J. Lee, Y. C. Cho, S. Y. Jeong, C. R. Cho, and S. Cho, "Room-temperature ferromagnetism in Cr-doped GaN single crystals", Appl. Phys. Lett., **80**, 4187 (2002).

[20] Y. Matsumoto, M. Murakami, T. Shono, T. Hasegawa, T. Fukumura, M. Kawasaki, P. Ahmet, T. Chikyow, S. Koshihara, and H. Koinuma, "Room-temperature ferromagnetism in transparent transition metal-doped titanium dioxide", Science, **291**, 854 (2001).

[21] K. Ueda, H. Tabata, and T. Kawai, "Magnetic and electric properties of transition-metal-doped ZnO films", Appl. Phys. Lett., **79**, 988 (2001).

[22] G. A. Medvedkin, T. Ishibashi, T. Nishi, K. Hayata, Y. Hasegawa, and K. Sato, "Room temperature ferromagnetism in novel diluted magnetic semiconductor $Cd_{1-x}Mn_xGeP_2$", Jpn. J. Appl. Phys., **39**, L949 (2000).

[23] S. W. Jung, S. J. An, G. C. Yi, C. U. Jung, S. I. Lee, and S. Cho, "Ferromagnetic properties of $Zn_{1-x}Mn_xO$ epitaxial thin films", Appl. Phys. Lett. **80**, 4561 (2002).

[24] S. Sonoda, S. Shimizu, T. Sasaki, Y. Yamamoto, and H. Hori, "Molecular beam epitaxy of wurtzite (Ga,Mn)N films on sapphire(0001) showing the ferromagnetic behaviour at room temperature", J. Cryst. Growth, **237–239**, 1358 (2002).

[25] T. Jungwirth, J. Konig, J. Sinova, J. Kucera, and A. H. MacDonald, "Curie temperature trends in (III,Mn)V ferromagnetic semiconductors", Phys. Rev. B, **66**, 012402 (2002).

[26] S. Das Sarma, E. H. Hwang, and D. J. Priour, Jr., "Enhancing Tc in ferromagnetic

semiconductors", Phys. Rev. B, **70**, 161203(R) (2004).

[27] S. J. Potashnik, K. C. Ku, S. H. Chun, J. J. Berry, N. Samarth, and P. Schiffer, "Effects of annealing time on defect-controlled ferromagnetism in $Ga_{1-x}Mn_xAs$", Appl. Phys. Lett., **79**, 1495 (2001).

[28] K. C. Ku, S. J. Potashnik, R. F. Wang, S. H. Chun, P. Schiffer, N. Samarth, M. J. Seong, A. Mascarenhas, E. Johnston-Halperin, R. C. Myers, A. C. Gossard, and D. D. Awschalom, "Highly enhanced Curie temperature in low-temperature annealed [Ga,Mn]As epilayers", Appl. Phys. Lett., **82**, 2302 (2003).

[29] A. J. Nadolny, J. Sadowski, B. Taliashvili, M. Arciszewska, W. Dobrowolski, V. Domukhovski, E. Łusakowska, A. Mycielski, V. Osinniy, T. Story, K. Świątek, R. R. Gałązka and R. Diduszko, "Carrier induced ferromagnetism in epitaxial Sn1-xMnxTe layers", J. Magn. Magn. Mater., **248,** 134 (2002).

[30] T. Story and R. R. Calazka, R. B. Frankel and P. A. Wolff, "Carrier-concentration induced ferromagnetism in PbSnMnTe", Phys. Rev. Lett., **56**, 777, (1986).

[31] R. W. Cochrane, M. Plischke and J. O. Strom-olsen "Magnetization studies of $(GeTe)_{1-x}(MnTe)_x$ pseudobinary alloys", Phys. Rev. B, **9** 3013 (1974)

[32] Y. Fukuma, M. Arifuku, H. Asada, and T. Koyanagi, "Correlation between magnetic properties and carrier concentration in $Ge_{1-x}Mn_xTe$", J. Appl. Phys., **91**, 7502 (2002).

[33] R. T. Lechner, G. Springholz, R. Kirchschlager, T. Schwarzl and G. Bauer, Annual report, Institute for Semiconductor and Solid State Physics, 2006; Johannes Kepler University, Altenbergerstr. 69, A-4040 Linz

www.hlphys.jku.at/files/annual_report_2006.pdf.

[34] S. Das Sarma, E. H. Hwang, A. Kaminski, "How to make semiconductors ferromagnetic: a first course on spintronics", Solid State Commun., **127**, 99, (2003).

[35] Y. Fukuma, T. Murakami, H. Asada and T. Koyanagi, "Film growth of $Ge_{1-x}Mn_xTe$ using ionized-cluster beam technique", Physica E **10,** 273 (2001);

[36] Y. Fukuma, H. Asada, N. Nishimura, and T. Koyanagi, "Ferromagnetic properties of IV-VI diluted magnetic semiconductor $Ge_{1-x}Mn_xTe$ films prepared by radio frequency sputtering", J. Appl. Phys., **93**, 4034 (2003).

[37] W. Knoff, P. Dziawa, V. Oshinniy, B. Taliashvili, V. Domuchowski, T. Story "Ferromagnetic transition in $Ge_{1-x}Mn_xTe$ semiconductor layers" Materials Science-Poland, **25**, No. 2, (2007).

[38] R. Tsu, W. E. Howard, and L. Esaki, "Optical and Electrical Properties and Band Structure of GeTe and SnTe" Phys. Rev. **172**, 779 (1968).

[39] S. K. Bahl and K. L. Chopra, "Amorphous versus Crystalline GeTe Films. III. Electrical Properties and Band Structure", J. Appl. Phys., **41**, 2196 (1970).

[40] Y. Fukuma, H.Asada, M. arifuku, and T. Koyanagi, "Carrier-induced ferromagnetism in $Ge_{1-x}Mn_xTe$" Appl. Phys. Let., **80,** 1013 (2002).

[41] M. Linnarsson, E. Janzen, B. Monemar, M. Kleverman, and A. Thilderkvist, "Electronic structure of the GaAs:Mn-Ga center", Phys. Rev. B, **55,** (1997), 6938

CHAPTER 2 LITERATURE REVIEW

2.1 Theoretical Review of origin of the DMS properties

2.1.1 s(p)–d(f) exchange interactions

The understanding of the origin of the properties of DMS can be started with a model of their band structure [1], in which two electronic subsystems are distinguished: one containing delocalized, band electrons built primarily of outer s and p orbital of constituting atoms, and the other consisting of the magnetic impurity electrons with magnetic moments localized in the ionic open 3d (or 4f) shell. Both the localized magnetic moments (d-d) interaction and the strong spin dependent sp–d(f) exchange interactions between these two subsystems may account for the magnetic properties observed in DMS system.

Two independent exchange mechanisms, namely the direct Coulomb exchange and the hybridization-mediated kinetic exchange, are responsible for the spin-dependent interactions between band carriers and localized impurity magnetic moments in DMS [2]. In general, spin-dependent Kondo Hamiltonian is used to describe the spin interactions, which represents the low energy dynamics of the quantum many-electron system. The original spin-dependent Kondo Hamiltonian is put in the form: $\hat{H}_{ex} = -2\sum_{k,k'} J_{kk'} e^{i(\vec{k}'-\vec{k})\vec{R}_I} \vec{\vec{S}}_I \cdot \vec{\vec{S}}_{kk'}$, (2-1)

where $J_{kk'}$ is the exchange constant, $\vec{\vec{S}}_I$ is the spin operator of the state L of the impurities at position R and $\vec{\vec{S}}_{kk'}$ is the spin operator for the band electron.

The direct Coulomb exchange is a first-order perturbation effect. Liu reported that the direct Coulomb exchange leads to a ferromagnetic Kondo Hamiltonian with the total spin of magnetic impurity S for the s-like conduction bands and for transition metal ions with the open d shell [3]. The same models have been shown by Kossut et al. for the coupling between the localized magnetic moment and the electron in the p-like band of zinc-blende III-V and II-VI compounds [4, 5]. To account for the many magnetic ions in the DMS crystal, the molecular field approximation was introduced [6], which consists in configurational and thermodynamical averaging of the Hamiltonian, i.e. replacing the spin operators by their averages. Therefore, the carrier-ion direct exchange Hamiltonian is represented as:

$$H_{ex} = -xN_0\alpha\langle S_{//}\rangle s_{//}, \tag{2-2}$$

where $s_{//}$ and $\langle S_{//}\rangle$ are the components along the magnetic field of the band electron spin and the thermodynamical average of the impurity spin, respectively; xN_0 is the concentration of magnetic ions and α is the exchange constant for s-like electrons. Most optical, transport and magnetic properties of the band electrons in DMS were successfully interpreted within the virtual crystal and mean field approximations.

It was proved by Schrieffer and Wolf [7, 8] that the hybridization terms in the Anderson Hamiltonian also led to the Kondo Hamiltonian involving the total spin of the impurity, but with opposite sign of the exchange constant. It was suggested by Dietl [9] and Bhattacharjee *et al* [10] that the hybridization mediated p–d kinetic exchange is responsible for the observed sign and magnitude of the constant β in Mn-based II–VI DMS. The spin dependence of the hybridization-induced interactions results from the

Pauli principle, which allows only for virtual transitions decreasing the total spin of the ion by either removing the electron spin from the d orbital or adding one with opposite spin, which leads to an antiferromagnetic, Kondo-like interaction [11, 12].

2.1.2 Spin-spin (d-d) interactions between magnetic ions

The interactions that couple the spins of magnetic ions are also responsible for DMS with magnetic properties. There are several microscopic mechanisms that lead to the spin–spin (d–d) interactions between two magnetic ions. In two main mechanisms, namely superexchange and the double exchange, the interaction can be considered as a virtual transition between the ions and neighbouring anions.

The super-exchange is a mechanism in which the spins of two ions are correlated due to the spin-dependent kinetic exchange interaction between each of the two ions and the *s, p* band. Larson *et al*. [11] have shown that for group II–VI DMS the dominant spin–spin interaction responsible for the magnetic behavior comes from the super-exchange. The double exchange interaction occurs when the magnetic ions in DMS contains the same chemical but different charge state [13]. The double exchange implies the coupling of magnetic ions in different charge state by the virtual hopping of an 'extra' electron from one ion to the other through interactions with the *p*-orbitals. This mechanism was proposed by Zener [14] in the 1950s and was applied to interpret ferromagnetism caused by the coexistence of the Mn^{2+} and Mn^{3+} in ZnO [15] and $CdGeP_2$ [16].

2.1.3 RKKY interaction

RKKY interaction can be used to describe the ion-ion interaction in DMS only when a high concentration of free carriers is present. It can be understood as the interaction between a local magnetic impurity and the surrounding electron gas [17]. Carriers are polarizable medium that transmit spin polarization from one atomic site to another. In the vicinity of a spin-polarized impurity ion, spin-up and spin-down electrons feel a different potential which means that spin-up and spin-down electrons are scattered differently. Due to different phase shift, the oscillation of the spin-up electron density is shifted relative to the oscillation of the spin-down density. The superposition of these two charge densities yields an oscillatory magnetization which decays according to the dimensionality of impurity considered. RKKY-interaction explains that atoms at a given distance from the impurity feel either a positive or a negative polarization and consequently have magnetic moment of respective orientation. The RKKY interaction is carrier-induced, sufficiently long range to account for the magnetic interaction in dilute systems, and has been put forward to explain the carrier (hole)-induced ferromagnetism observed in Mn-based III-V [18] and IV-VI thin films [19, 20].

2.1.4 Zener model

It was shown by Dietl *et al* [21, 22] that when the mean ion–ion distance is small with respect to $1/k_F$, the Zener model has to be invoked to explain the observed properties of Mn-based III–V and II–VI thin films and heterostructures. This is due to the importance of the kp, spin–orbit and carrier–carrier interactions, which are

difficult to take into account within the RKKY model. When these interactions are neglected, the mean-field values of the ordering temperature deduced from the Zener equals to the RKKY model.

In Zener model [23], the spin polarization of the localized spins results in a spin splitting of the bands and in this situation the exchange coupling between the carriers and the localized spins leads to ferromagnetism. The redistribution of the carriers between the spin sub-bands lowers the energy of the holes carriers, which at sufficiently low temperatures overcompensates an increase of the free energy associated with a decrease in Mn entropy. Dietl *et al* [21] suggested that the holes in the extended or weakly localized states mediate the long range interactions between the localized spins on both sides of the Anderson–Mott metal–insulator transition (MIT) in the Mn doped II-VI and III-V DMS. They also showed that the holes transmit magnetic information efficiently between the Mn spins due to the large density of states in the valence band and strong spin-dependent p–d hybridization. The p-d Zener model has been successful in explaining a number of properties observed in ferromagnetic DMS, particular (Ga,Mn)As and (In, Mn)As, including the ferromagnetic transition temperature T_C [24], magnetocrystalline anisotropy [25], the anomalous Hall effect [26] and so on.

2.1.5 Porlaron Percolation theory

The porlaron percolation theory has been developed to understand the ferromagnetic ordering of the DMS with strongly localized carriers. The formation of

bound magnetic polarons (BMP) results from the exchange interaction of those strongly localized carriers with magnetic impurities. Since the carrier concentration is much less than the magnetic impurities density, a localized hole is surrounded by the impurity spins in a BMP as shown in Fig. 2-1 [27]. Even though the direct exchange interaction of the localized carriers may be antiferromagnetic, the interaction between bound magnetic polarons can be ferromagnetic [28] if the concentration of the magnetic impurities is large enough. The localized holes (large arrows) produce an effective field for the impurity spins (small arrows). The maximum of this effective magnetic field is achieved when the spins of the localized holes are parallel. When the direction of impurity spins is parallel to the effective field, the energy minimum and the field maximum are also achieved. Therefore at low temperatures the system should eventually reach the state where the spins of all holes point in the same direction, and all impurity spins point in the same or in the opposite direction, depending on the sign of the impurity-hole exchange interaction.

Taking into account the high defect concentration in a typical magnetic semiconductor material, the localized charge carrier density in the systems is highly inhomogeneous too. Since the exchange interaction between magnetic impurities is transmitted through the charge carriers, this interaction must also be highly inhomogeneous [29]. When the temperature is lowered, in the regions with higher charge-carrier density, the ferromagnetic transition will first occur locally (align a spin in parallel or antiparallel with all the impurity spins in the vicinity), leading to the formation of a BMP. As temperature falls further, the polaron grows in size until its

radius overlaps that of neighbouring polarons, enabling long-range interactions between TM ions and ferromagnetic ordering in low carrier density systems. BMP begins to form at a certain temperature and their diameter will increase with decreasing temperature and eventually spreads over the whole system at the Curie temperature to produce ferromagnetism.

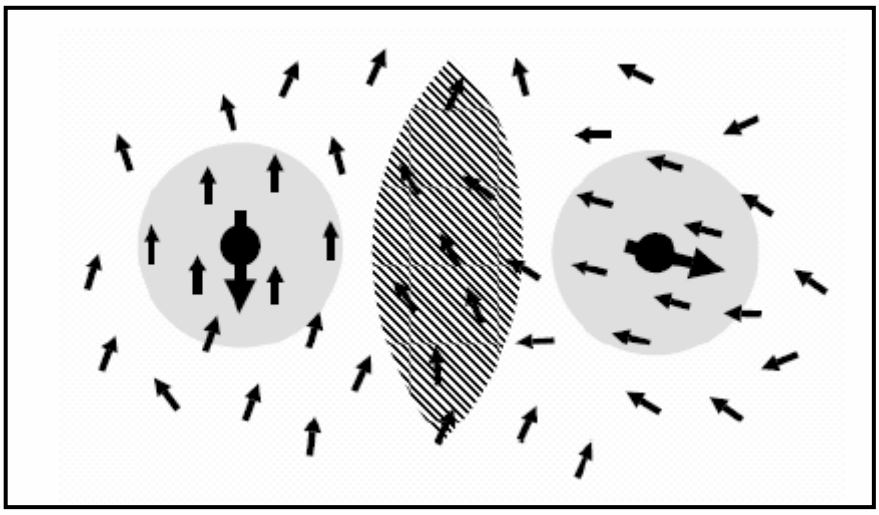

Figure 2-1 Interaction of two bound magnetic polarons. The polarons are shown with gray circles. Small and large arrows show impurity and hole spins, respectively. [Ref. 27]

2.1.6 Secondary phases and spinodal decomposition

If the mean density of the magnetic consitutent exceeds the solubility at given growth or thermal processing conditions, the film will decompose into nanoregions with low and high concentrations of magnetic ions constitutes, which occurs as a generic property of many DMS and diluted magnetic oxides (DMO) [30, 31]. This decomposition can either form the nonrandom precipitate of secondary phases which normally have different crystal properties from DMS or result in the spinodal

decomposition which does not usually involve any precipitation of other crystallographic phases. The spinodal decomposition is not easy to detect experimentally; nonetheless sometimes Transmission Electron Microscopy (TEM) can provide such information. It has been reported that both hexagonal and zinc-blende Mn-rich (Ga,Mn)As nanocrystals are clearly observed by TEM in annealed (Ga,As)Mn, which corresponds to precipitation of other phases and spinodal decomposition, respectively [32, 33].

Owing to the high concentration of the magnetic constituent, the nanocrystals forming by spinodal decomposition usually have high spin ordering temperature, typically above the room temperature. Therefore, it is reasonable to suppose the high apparent Curie temperatures come from the coherent nanocrystals with a large concentration of magnetic constituent in some DMS systems. Especially, it is able to explain the origin of the ferromagnetic response in those DMS, in which the average magnetic ions is below the percolation limit for the nearest neighbour coupling and at the same time, the free carrier density is too low to mediate an efficient long-range exchange interactions.

In general, the mechanism for the observed magnetic behaviour is complex and the exact origin of ferromagnetism in DMS remains incompletely understood so far. The main reason is that experimental results are strongly influenced by many factors, leading to controversial results even for the same type of DMS materials. These factors include growth or process conditions (temperature, source material of dopant and dopant concentrations) and also growth techniques difference (MBE, MOCVD,

pulsed laser deposition, rf sputtering) which may also result in different physical, electronic and magnetic properties. Sometimes, the experimental results may also contradict with the theoretical studies and predictions. Therefore, single mechanism may not be adequate to explain the mechanism of ferromagnetism behavior observed in DMS systems. When assigning the origin of ferromagnetism, decision needs to be taken on a case-by-case basis.

2.2 Review of Different Groups of DMS

2.2.1 Group II-VI

Extensive studies of DMSs started in the late 1970s, when appropriately purified Mn was employed to grow bulk II-VI Mn-based alloys by various modifications of the Bridgman method [4, 9]. Since the valence of the cations in II-VI semiconductors matches that of the common magnetic ions such as Mn, it makes these DMSs relatively easy to prepare in bulk form as well as in thin epitaxial layers. However, doping of II-VI compounds is often difficult and usually one conduction type is available, which made the material less attractive for applications. Moreover, the magnetic interaction in II-VI DMSs is dominated by the antiferromagnetic exchange among the Mn spins, which results in the paramagnetic, antiferromagnetic, or spin-glass behavior of the material. The breakthrough was made by the advances in technology for doping in II-VI semiconductor to achieve carrier density in excess of 10^{19} cm^{-3} [34]. Shortly after a theory of ferromagnetic transition based on p-d exchange interactions was put forward [35], ferromagnetism was observed below 1.8 K in modulation doped p type

$Cd_{0.975}Mn_{0.025}Te$ quantum well [36]. Ferromangetism has also been found in p type $Zn_{1-x}Mn_xTe$ [37, 38] and $Be_{1-x}Mn_xTe$ [39], however, those Mn doped II-VI DMS have very low T_C, normally less than 5K. Recently, the Cr-based II-VI DMS has attracted interests since the observation of ferromagnetism below 100K in (Zn, Cr)Se [40] although it is believed that the ferromagnetism may come from the precipitates, such as spinel semiconductor $ZnCr_2Se_4$. (Zn, Cr)Te with 20% of Zn have been reported to have above room temperature ferromagnetism [41].

2.2.2 Group III-V

III-V-based diluted magnetic semiconductors have attracted much attention as candidate materials for spintronic applications since III-V semiconductors such as GaAs are already in use in a wide variety of electronic and optoelectronic devices. The major obstacle in making III-V semiconductors magnetic has been the low solubility of magnetic elements (such as Mn) in the compounds compared with II-VI DMS. A breakthrough was made by using molecular beam epitaxy (MBE), a thin-film growth technique in vacuum that allows one to work far from equilibrium. Up to now, (In,Mn)As [42-45] and (Ga,Mn)As [46, 47] are the two well-studied semiconductors. The common feature of these two semiconductors is the existence of ferromagnetic order induced by holes supplied by the Mn acceptors [48, 49]. In 1989, Munekata et al. used low temperature MBE method and succeeded in epitaxial growth of (In,Mn)As [42]. For a given Mn composition, (Ga,Mn)As exhibits a higher Curie temperature than (In,Mn)As, whereas (In,Mn)As can accommodate a larger amount of Mn atoms into the host crystal lattice [42, 43, 48, 49, 50]. The growth of (Ga, Mn)As with highest

Tc~110K was reported in 1990s [51]. The mean-field Zener model predictes that Tc of (Ga, Mn)As is proportional to the Mn concentration [22, 49]. However, it is difficult to grow the substantial Mn due to the easy formation of MnAs clusters when the Mn doping concentration is above the solubility limit. Recently, by carefully controlling the growth conditions and the post-growth annealing, the highest T_C~173K has been obtained [24].

2.2.3 Group IV and wide band gap Ferromagnetic Semiconductors

Group IV Si and Ge based diluted magnetic semiconductor have attracted lots of interests owing to their compatibility with current semiconductor technology. Observation of ferromagnetism has been reported in Ge single doped with Mn-[52-54], Cr-[55] and Fe-[56]. Co-doped (Mn, Co), (Mn, Fe) Ge increases the Curie temperature up to 270K [57] and 350K [58], respectively. Vacuum evaporated Mn_xSi_{1-x}, has been reported to show the ferromagnetism [59]. A Curie temperature above room temperature is reported recently for Mn- implanted Si as well [60].

Other groups of the diluted magnetic semiconductor; namely, wide band gap group III-nitrides, phosphides and semiconductor oxides have made remarkable progress since the appearance of the Dietl et al. paper [22], which predicts above room temperature Tc for materials, such as GaN and ZnO, containing 5% of Mn and a high hole concentration. Several systems have been investigated, such as Mn-doped GaN [61-63], Mn-doped GaP [64], Cr-doped GaN [65], transition metal-doped ZnO [66, 67] and Co-doped TiO_2 [68, 69]. Although most of the system are found to have

above room temperature Tc, the origin of the ferromagnetism needs further investigation to confirm, as discussed in 2.1.6.

2.2.4 Group IV-VI

Diluted magnetic cubic IV-VI compounds which crystallize in the rock salt structure have attracted considerable interest in recent years. In PbTe, PbSe, PbS and GeTe, the group IV element has been replaced by transition metal (such as Mn^{2+}) or rare earth element (such as Eu^{2+} [70]). Back in the 1970s, the observation of ferromagnetic ordering has already been reported in $Sn_{1-x}Mn_xTe$ [71], $Ge_{1-x}Mn_xTe$ [72] and PbGeMnTe [73] systems with high carrier concentrations $p=10^{20}$ to 10^{21} cm^{-3}. In 1986, T. Story first demonstrated the effect of carrier concentration on the magnetic properties of semimagnetic semiconductors in PbGeMnTe [74]. It shows that the magnetic properties are determined by both the magnetic-ion concentration and charge-carrier concentration. Moreover, the indirect exchange via carriers (RKKY interaction) seems to be sufficiently long range to account for the ferromagnetism of PbGeMnTe. The superexchange dominates in the IV-VI DMS like in the II-VI DMS despite the crystal structure difference [75, 76].

The magnetic properties of GeTe based diluted mangetic semiconductors with 3d transition metals from Ti to Ni have been investigated by Fukuma [77]. But only Cr, Mn and Fe doped GeTe films are ferromagnetic, whereas the Ti, V, Co and Ni doped films are paramagnetic. The highest Curie temperature reported for Cr, Mn and Fe doped GeTe thin films are 180K [78], 200K [79], and 100K [77], respectively.

2.3 Review of GeMnTe Ferromagnetic Semiconductors

The first magnetic studies of $(GeTe)_{1-x}(MnTe)_x$ alloy were carried out by Rodot et al. in 1960s who reported that the system orders ferromagnetically even though MnTe itself is antiferromagnetic [80]. In 1970s, R. W. Cochrane and his group presented the measurement and analysis of the magnetic and transport properties of $(GeTe)_{1-x}(MnTe)_x$ for $0<x<0.5$ [72, 81]. The samples were prepared by mixing GeTe and MnTe in the desired proportions in an evacuated sealed quartz ampoule. The measurement shows that for $x<0.15$, ferromagnetic ordering temperature varied linearly with concentration at the rate 4.4K per at.% MnTe, which corresponds to the RKKY theory with an exchange constant J_{pd} 0.8~0.9 eV between the free carriers and the manganese ions. For $x>0.2$, the experimental results suggests the inhomogeneities in Mn distributions.

More recently, Y. Fukuma et al. published a few papers on the growth and characterization of the single crystal diluted magnetic semiconductor $Ge_{1-x}Mn_xTe$ [82-87]. They successfully used ionized-cluster beam and rf sputtering methods to grow the ferromagnetic $Ge_{1-x}Mn_xTe$ thin films up to $x=0.96$. The highest T_C obtained is 140K with $x=0.51$. The temperature dependence of spontaneous magnetization suggests the existence of multiple mangnetic interactions. The authors also investigated the correlation between the magnetic properties and carrier concentrations and they suggested that at the low carrier concentration, cluster of spins aligned by short-range ferromagnetic interaction tends to be formed. With the

increase of the carrier concentration, the long-range ferromagnetic interaction (RKKY interaction) between Mn ions appears in magnetic behavior. The photoemission of XMCD spectroscopy analyses were carried out in terms of the study of electronic structure and suggested that Mn 3d states are nearly localized with the divalent character [88-90].

First-principle calculations have been done on the $Ge_{1-x}Mn_xTe$ diluted magnetic semiconductors with different composition by Z. Xie et al. [91]. They confirmed Fukuma et al.'s spectroscopy results and found that Ge atoms and Mn atoms play competitive role in the occurrence of ferromagnetism. Therefore $Ge_{1-x}Mn_xTe$ with a moderate composition (x=0.51) of Mn atoms is supposed to have highest Curie temperature, which is consistent with the experimental study. In Adrian Ciucivara et al.'s density functional study of $Ge_{1-x}Mn_xTe$ [92], it is found that each Mn creates two holes and magnetization increases monotonically with hole density and reach the highest about x=0.5. More recently, Zhao et al. reported a half-metallicity in $Ge_5Mn_2Te_8$ ternary compound by the full-potential density-functional method [93].

Besides the theoretical and experimental study on the single crystal $Ge_{1-x}Mn_xTe$ thin films, Fukuma's group also studied the ferromagnetic fine patterns in the $Ge_{1-x}Mn_xTe$ films by the phase change method [94]. The amorphous films which are paramangetic are crystallized into the ferromagnetic films by annealing. Recently, there is also a report of $Ge_{0.66}Mn_{0.34}$ single layer and superlattice consisting of 40 × [86 nm $Ge_{0.68}Mn_{0.32}Te$ / 0.5 nm MnTe] with T_C > 200 K grown by MBE [79].

References:

[1] S.V. Vonsovskii, Magnetism, John Wiley & Sons: New York, (1974).

[2] P. Kacman, "Spin interactions in diluted magnetic semiconductors and magnetic semiconductor structures", Semicond. Sci. Technol., **16**, R25 (2001).

[3] H. Liu, "Exchange Interaction between Conduction Electrons and Magnetic Shell Electrons in Rare-Earth Metals", Phys. Rev., **121**, 451 (1961).

[4] J. K. Furdyna and J. Kossut J (ed) 1988 Diluted Magnetic Semiconductors, Semiconductors and Semimetals vol 25 (New York: Academic)

[5] J. Kossut, Phys. Status Solidi b, **78**, 536 (1976).

[6] J. A. Gaj, R. Planel and G. Fishman, "Relation of magneto-optical properties of free excitons to spin alignment of Mn^{2+} ions in $Cd_{1-x}Mn_xTe$", Solid State Commun., **29**, 435 (1979).

[7] J. R. Schrieffer and P. Wolf, "Relation between the Anderson and Kondo Hamiltonians", Phys. Rev., **149**, 491 (1966).

[8] J. R. Schrieffer, "The Kondo Effect—The Link Between Magnetic and Nonmagnetic Impurities in Metals?" J. Appl. Phys., **38**, 1143 (1967).

[9] T. Dietl 1981 Physics in High Magnetic Fields (Springer Series in Solid-State Physics vol 24) ed M Miura (Berlin: Springer).

[10] A. K. Bhattacharjee, G. Fishman and B. Coqblin "Virtual bound-state model for the exchange interaction in semimagnetic semiconductors such as $Cd_{1-x}Mn_xTe$", Physica B&C, **117**, 449 (1983).

[11] B. E. Larson, K. C. Hass, H. Ehrenreich and A. E. Carlsson, "Theory of exchange

interactions and chemical trends in diluted magnetic semiconductors", Phys. Rev. B, **37,** 4137 (1988).

[12] J. Blinowski and P. Kacman, "Spin-dependent interaction of a band electron with impurities", Acta Phys. Polon. A, **79**, 145 (1991).

[13] J. Blinowski and P. Kacman, "Double exchange in mixed-valency diluted magnetic semiconductors", Acta Phys. Polon., **90**, 731 (1996)

[14] C. Zener "Interaction between the d-Shells in the Transition Metals. II. Ferromagnetic Compounds of Manganese with Perovskite Structure**",** Phys. Rev., **82**, 403 (1951).

[15] K. Sato and H. Katayama-Yoshida, "Material design for transparent ferromagnets with ZnO-based magnetic semiconductors", Japan. J. Appl. Phys., **39**, L555 (2000)

[16] G. A. Medvedkin, T. Ishibashi, T. Nishi, K. Hayata, Y. Hasegawa and X. Sato, "Room temperature ferromagnetism in novel diluted magnetic semiconductor $Cd_{1-x}Mn_xGeP_2$", Japan. J. Appl. Phys., **39**, L949 (2000).

[17] P. Mohn, Magnetism in the Solid State (Spriger, New York, 2003).

[18] T. Dietl, J. Cibert, D. Ferrand and Y. Merle d'Aubign´e, "Carrier-mediated ferromagnetic interactions in structures of magnetic semiconductors", Mater. Sci. Eng. B, **63**, 103 (1999).

[19] Y. Fukuma, H. Asada, M. Arifuku, and T. Koyanagi, "Carrier-enhanced ferromagnetism in $Ge_{1-x}Mn_xTe$", Appl. Phys. Lett., **80**, 1013 (2002).

[20] P. Łazarczyk, T. Story, M. Arciszewska and R. R. Gał¸azka, "Magnetic phase diagram of $Pb_{1-x-y}Sn_yMn_xTe$ semimagnetic semiconductors", J. Magn. Magn. Mater.

169, 151 (1997).

[21] T. Dietl, H. Ohno and F. Matsukura, "Hole-mediated ferromagnetism in tetrahedrally coordinated semiconductors",

http://arxiv.org/PS_cache/cond-mat/pdf/0007/0007190v2.pdf

[22] T. Dietl, H. Ohno, F. Matsukura, J. Cibert and D. Ferrand , "Zener model description of ferromagnetism in zinc-blende magnetic semiconductors", Science **287**, 1019 (2000).

[23] C. Zener, "Interaction Between the *d* Shells in the Transition Metals " Phys. Rev. **81**, 440 (1950).

[24] T. Jungwirth, K. Y. Wang, J. Mašek, K. W. Edmonds, J. König, J. Sinova, M. Polini, N. A. Goncharuk, A. H. MacDonald, M. Sawicki, A. W. Rushforth, R. P. Campion, L. X. Zhao, C. T. Foxon, and B. L. Gallagher, "Low-temperature magnetization of (Ga,Mn)As semiconductors", Phys. Rev. B, **72**, 165204 (2006).

[25] K. Takamura, F. Matsukura, D. Chiba, and H. Ohno, "Magnetic properties of (Al,Ga,Mn)As", Appl. Phys. Lett. **81**, 2590 (2002).

[26] T. Jungwirth, J. Sinova, J. Mašek, J. Kučera, and A. H. MacDonald, "Theory of ferromagnetic (III,Mn)V semiconductors", Rev. Mod. Phys., **78**, 809 (2006).

[27] A. Kaminski and S. Das Sarma, "Polaron percolation in diluted magnetic semiconductors", Phys. Rev. Lett. **88**, 247202, (2002).

[28] P. A. Wolff, R. N. Bhatt, and A. C. Durst, "Polaron-polaron interactions in diluted magnetic semiconductors", J. Appl. Phys. **79**, 5196 (1996).

[29] A. Kaminski and S. Das Sarma, "Magnetic and transport percolation in diluted

magnetic semiconductors", Phys. Rev. B. **68**, 235210 (2003).

[30] T. Dietl, "Origin and control of ferromagnetism in dilute magnetic semiconductors and oxides", J. Appl. Phys., **103**, 07D111, (2008).

[31] T, Dietl, "Origin of ferromagnetism and nano-scale phase separations in diluted magnetic semiconductors", Physica E, **35**, 293, (2006).

[32] M. Moreno, A. Trampert, B. Jenichen, L. Daweritz and K. H. Ploog, "Correlation of structure and magnetism in GaAs with embedded Mn(Ga)As magnetic nanoclusters", J. Appl. Phys. **92**, 4672 (2002).

[33] M. Yokoyama, H. Yamaguchi, T. Ogawa, M. Tanaka M, "Zinc-blende-type MnAs nanoclusters embedded in GaAs", J. Appl. Phys., **97**, 10D317, (2005).

[34] T. Baron, S. Tatarenko, K. Saminadayar, N. Magnea, and J. Fontenille, "Plasma nitrogen doping of ZnTe, CdZnTe, and CdTe by molecular beam epitaxy," Appl. Phys. Lett., **65**, 1284 (1994).

[35] T. Dietl, A. Haury, and Y. Merle d'Aubigné, "Free carrier-induced ferromagnetism in structures of diluted magnetic semiconductors," Phys. Rev., B **55**, R3347 (1997).

[36] A. Haury, A. Wasiela, A. Arnoult, J. Cibert, S. Tatarenko, T. Dietl, and Y. Merle d'Aubigné, "Observation of a ferromagnetic transition induced by two-dimensional hole gas in modulation-doped CdMnTe quantum wells," Phys. Rev. Lett., **79**, 511 (1997).

[37] D. Ferrand, J. Cibert, C. Bourgognon, S. Tatarenko, A. Wasiela, G. Fishman, A. Bonanni, H. Sitter, S. Kolesnik, J. Jaroszynski, A. Barcz, and T. Dietl,

"Carrier-induced ferromagnetic interactions in p-doped ZnMnTe epilayers," J. Cryst. Growth, **214/215**, 387 (2000).

[38] D. Ferrand, J. Cibert, A. Wasiela, C. Bourgognon, S. Tatarenko, G. Fishman, S. Kolesnik, J. Jaroszynski, T. Dietl, B. Barabara, and D. Dufeu, "Carrier-induced ferromagnetic interactions and transport properties of ZnMnTe epilayers," J. Appl. Phys., **87**, 6451 (2000).

[39] L. Hansen, D. Ferrand, G. Richter, M. Thierley, V. Hock, N. Schwarz, G. Reuscher, G. Scmidt, A. Waag, and L.W. Molenkamp, "Epitaxy and magneto-transport properties of the diluted magnetic semiconductor p-$Be_{1-x}Mn_xTe$,", Appl. Phys. Lett. **79**, 3125 (2001).

[40] G. Karczewski, M. Sawicki, V. Ivanov, C. Ruester, G. Grabecki, F. Matsukura, L.W. Molenkamp, and T. Dietl, "Ferromagnetism in (Zn,Cr)Se layers grown by molecular beam epitaxy" J. Supercond., **16,** 55 (2003).

[41] H. Saito, V. Zayets, S. Yamagata, and K. Ando, "Room-temperature ferromagnetism in a II-VI diluted magnetic semiconductor $Zn_{1-x}Cr_xTe$", Phys. Rev. Lett. **90,** 207202 (2003).

[42] H. Munekata, H. Ohno, S. von Molnár, A. Segmüller, L. L. Chang, and L. Esaki, "Diluted Magnetic III-V Semiconductors", Phys. Rev. Lett., **63**, 1849 (1989);

[43] H. Ohno, H. Munekata, T. Penney, S. von Molnár, and L. L. Chang, "Magnetotransport Properties of p-type (In,Mn)As Diluted Magnetic III-V Semiconductors", Phys. Rev. Lett. **68**, 2664 (1992).

[44] S. Koshihara, A. Oiwa, M. Hirasawa, S. Katsumoto, Y. Iye, C. Urano, H. Takagi

and H. Munekata, "Ferromagnetic order induced by photogenerated carriers in magnetic III-V semiconductor heterostructures of (In,Mn)As/GaSb" Phys. Rev. Lett., **78**, 4617 (1997).

[45] H. Ohno, D. Chiba, F. Matsukura, T. Omiya, E. Abe, T. Dietl, Y. Ohno, and K. Ohtani, "Electric-field control of ferromagnetism", Nature **408**, 944 (2000).

[46] H. Ohno, "Properties of ferromagnetic III-V semiconductors", J. Magn. Magn. Mater. **200**, 110 (1999).

[47] H. Ohno and F. Matsukura, "A ferromagnetic III-V semiconductor: (Ga,Mn)As", Solid State Commun., **117**, 179 (2001).

[48] H. Ohno, "Making nonmagnetic semiconductors ferromagnetic", Science **281**, 951 (1998).

[49] T. Dietl, H. Ohno, F. Matsukura, "Hole-mediated ferromagnetism in tetrahedrally coordinated semiconductors", Phys. Rev. B, **63**, 195205 (2001).

[50] H. Munekata, A. Zaslavsky, P. Fumagali and R. J. Gambino, "Presparation of (In,Mn)As/(Ga,Al)Sb magnetic semiconductor heterostructures and their ferromagnetic characteristics", Appl. Phys. Lett., **63**, 2929 (1993).

[51] F. Matsukuram, H. Ohno, A. She, and Y. Sugawara, "Transport properties and origin of ferromagnetism in (Ga, Mn)As", Phys. Rev. B, **57,** R2037 (1998).

[52] Y. D. Park, A. T. Hanbicki, S. C. Erwin, C. S. Hellberg, J. M. Sullivan, J. E. Mattson, T. F. Ambrose, A. Wilson, G. Spanos, B. T. Jonker, "A Group-IV Ferromagnetic Semiconductor: Mn_xGe_{1-x}" Science, **295,** 651 (2002)

[53] S. Choi, S. C. Hong, K. Yunki J. B. Ketterson, B. J. Kim, Y. C. Kim and J. H.

Jung, "Ferromagnetism in Mn-doped Ge**",** Phys. Rev. B, **66**, 033303 (2002).

[54] A. Stroppa, S. Picozzi, and A. Continenza, A. J. Freeman, "Electronic structure and ferromagnetism of Mn-doped group-IV semiconductors**",** Phys. Rev. B, **68**, 155203 (2003).

[55] S. Choi, S. C. Hong, S. Cho, Y. Kim, J. B. Ketterson, C. U. Jung and K. Rhie, B. J. Kim and Y. C. Kim, "Ferromagnetism in Cr-doped Ge**",** Appl. Phys. Lett., **81**, 3606 (2002).

[56] S. Choi, S. C. Hong, S. Cho, Y. Kim, J. B. Ketterson, C. U. Jung and K. Rhie, B. J. Kim and Y. C. Kim,, "Ferromagnetic properties in Cr, Fe-doped Ge single crystals**"** J. Appl. Phys. **93**, 7670 (2003).

[57] F. Tsui, L. He, L. Ma, A. Tkachuk, Y. S. Chu, K. Nakajima, and T. Chikyow, "Novel Germanium-Based Magnetic Semiconductors", Phys. Rev. Lett. **91**, 177203 (2003)

[58] H. Braak R.R. Gareev, D.E. Bürgler, R. Schreiber, P. Grünberg and C.M. Schneider, "Magnetic characteristics of epitaxial Ge(Mn,Fe) diluted films —a new room temperature magnetic semiconductor?", J. Magn. Magn. Mater., **286**, 46 (2005).

[59] K. Schwinge, C. Muller, A. Mogilatenko, J. J. Paggel, P. Fumagalli, "Structure and magneto-optic Kerr measurements of epitaxial MnSi films on Si(111)", J. Appl. Phys., **97**, 103913 (2005).

[60] I. T. Yoon, C. J. ParK, T. W. Kang, "Magnetic and optical properties of Mn-implanted Si material", J. Magn. Magn. Mater., **311**, 693 (2007).

[61] G. T. Thaler, M. E. Overberg, B. Gila, R. Frazier, C. R. Abernathy, S. J. Pearton, J.

S. Lee, S. Y. Lee, Y. D. Park, Z. G. Khim, J. Kim, F. Ren, "Magnetic properties of n-GaMnN thin films", Appl. Phys. Lett., **80**, 3964 (2002).

[62] M. E. Overberg, B. P. Gila, G. T. Thaler, C. R. Abernathy, S. J. Pearton, N. A. Theodoropoulou, K. T. McCarthy, S. B. Arnason, A. F. Hebard, S. N. G. Chu, R. G. Wilson, J. M. Zavada, Y. D. Park, "Room temperature magnetism in GaMnP produced by both ion implantation and molecular-beam epitaxy", J. Vac. Sci. Technol. B, **20**, 969 (2002).

[63] M. E. Overberg, C. R. Abernathy, S. J. Pearton, N. A. Theodoropoulou, K. T. McCarthy, and A. F. Hebard, "Indication of ferromagnetism in molecular-beam-epitaxy-derived N-type GaMnN", Appl. Phys. Lett. **79**, 1312 (2001).

[64] N. Theodoropoulou, A. F. Hebard, M. E. Overberg, C. R. Abernathy, S. J. Pearton, S. N. G. Chu, and R. G. Wilson, "Unconventional carrier-mediated ferromagnetism above room temperature in ion-implanted (Ga,Mn)P:C", Phys. Rev. Lett., **89**, 107203 (2002).

[65] M. Hashimoto, Y. Z. Zhou, M. Kanamura, and H. Asahi, "High temperature (> 400 K) ferromagnetism, in III-V-based diluted magnetic semiconductor GaCrN grown by ECR molecular-beam epitaxy", Solid State Commun., **122**, 37 (2002).

[66] T. Wakano, N. Fujimura, Y. Morinaga, N. Abe, A. Ashida, and T. Ito, "Magnetic and magneto-transport properties of ZnO:Ni films", Physica E, **10**, 260 (2001).

[67] T. Fukumura, Z. Jin, A. Ohtomo, H. Koinuma, and M. Kawasaki, "An oxide-diluted magnetic semiconductor: Mn-doped ZnO", Appl. Phys. Lett., **75**, 3366 (1999).

[68] Chambers SA, Thevuthasan S, Farrow RFC, Marks RF, Thiele JU, Folks L, Samant MG, Kellock AJ, Ruzycki N, Ederer DL, Diebold U, "Epitaxial growth and properties of ferromagnetic co-doped TiO_2 anatase", Appl. Phys. Lett., **79**, 3467 (2001).

[69] Matsumoto Y, Murakami M, Shono T, Hasegawa T, Fukumura T, Kawasaki M, Ahmet P, Chikyow T, Koshihara S, Koinuma H, "Room-temperature ferromagnetism in transparent transition metal-doped titanium dioxide", Science, **291**, 854 (2001).

[70] P. Norton and M. Tacke, "MBE of $Pb_{1-x}Eu_xSe$ for the use in IR devices", J. Crystal Growth, **81**, 405 (1987).

[71] M. Escorne, A. Ghazalli, P. Leroux Hgon, Proc 12th Int. Conf. Phys. Semicond., Ed. M. H. Pilkuhn (Teubner, Stuttgart 1974).

[72] R. W. Cochrane, M. Plischke, and J. O. Ström-olsen, " Magnetization studies of $(GeTe)_{1-x}(MnTe)_x$ pseudobinary alloys" Phys. Rev. B, **9**, 3013 (1974).

[73] T. Hamasaki, "Magnetic properties of $(Ge, Pb)_{1-x}Mn_xTe$", Solid State Commun., **32**, 1069 (1979).

[74] T. Story and R. R. Calazka, R. B. Frankel and P. A. Wolff, "Carrier-concentration induced ferromagnetism in PbSnMnTe", Phys. Rev. Lett., **56**, 777, (1986).

[75] M. Gorska and J. R. Anderson, " Magnetic-susceptibility and exchange in IV-VI compound diluted magnetic semiconductors", Phys. Rev. B, **38**, 9120, (1988).

[76] Mukesh Jain, "Diluted magnetic semiconductors", Singapore: World Scientific, 1991.

[77] Y. Fukuma, H. Asada, J. Miyashita, N. Nishimura, and T. Koyanagi, "Magnetic

properties of IV–VI compound GeTe based diluted magnetic semiconductors", J. Appl. Phys., **93**, 7667 (2003).

[78] Y. Fukuma, H. Asada, N. Moritake, T. Irisa, T. Koyanagi, "Ferromagnetic semiconductor $Ge_{1-x}Cr_xTe$ with a Curie temperature of 180 K" Appl. Phys. Lett. **91**, 092501 (2007).

[79] R. T. Lechner, G. Springholz, R. Kirchschlager, T. Schwarzl and G. Bauer, Annual report, Institute for Semiconductor and Solid State Physics, 2006; Johannes Kepler University, Altenbergerstr. 69, A-4040 Linz www.hlphys.jku.at/files/annual_report_2006.pdf.

[80] M. Rodot, J. Lewis, H. Rodot, G. Villers, J. Cohen, and P. Mollard, J. Phys. Soc. Jap. Suppl., **21**, 627 (1966).

[81] R. W. Cochrane, M. Plischke, and J. O. Ström-olsen, "Exchange scattering in a ferromagnetic semiconductor", Phys. Rev. B, **8**, 4262 (1973).

[82] Y. Fukuma, T. Murakami, H. Asada, and T. Koyanagi, "Film growth of $Ge_{1-x}Mn_xTe$ using ionized-cluster beam technique" Physica E, **10,** 273 (2001).

[83] Y. Fukuma, M. Arifuku, H. Asada and T. Koyanagi, "Growth of ferromagnetic semiconductor $Ge_{1-x}Mn_xTe$ films on $BaF_2(111)$ by ionized cluster beam deposition" J. Appl. Phys., **97**, 07910 (2005).

[84] Y. Fukuma, H. Asada, M. Arifuku, T. Koyanagi, "Influence of carrier concentration on magnetic phase transition in $Ge_{1-x}Mn_xTe$" J. Mag. Mag. Mat., **272–276,** 2012 (2004).

[85] Y. Fukuma, H. Asada, N. Nishimura and T. Koyanagi, "Ferromagnetic properties

of IV-VI diluted magnetic semiconductor $Ge_{1-x}Mn_xTe$ films prepared by radio frequency sputtering" J. Appl. Phys., **91,** 4034 (2003).

[86] Y. Fukuma, M. Arifuku, H. Asada and T. Koyanagi, "Correlation between magnetic properties and carrier concentration in $Ge_{1-x}Mn_xTe$" J. Appl. Phys., **91**, 7502 (2002).

[87] Y. Fukuma, H.Asada, M. arifuku, and T. Koyanagi, "Carrier-induced ferromagnetism in $Ge_{1-x}Mn_xTe$" Appl. Phys. Let., **80,** 1013 (2002).

[88] S. Senba, K. Fujimoto, H. Sato, Y. Fukuma, M. Nakatake, M. Arita, K. Tsuji, H. Asada, T. Koyanagi, H. Namatame, M. Taniguchi, "Mn 3p-3d resonant photoemission spectroscopy of ferromagnetic semiconductor $Ge_{1-x}Mn_xTe$" J. of Elec. Spectroscopy and Related Phenomena, **144–147,** 629 (2005).

[89] H. Sato, K. Fujimoto, Y. Fukuma, K. Tsuji, A. Kimura, M. Taniguchi, S. Senba, A.Tanaka, H. Asada, T. Koyanagi, " Mn 3d states in ferromagnetic semiconductor $Ge_{1-x}Mn_xTe$ investigated by Mn 2p-3d soft X-ray magnetic circular dichroism spectroscopy" J. of Elec. Spectroscopy and Related Phenomena, **144–147,** 727 (2005).

[90] Y. Fukuma, H. Sato, K. Fujimoto, K. Tsuji, A. Kimura, M. Taniguchi, S. Senba, A.Tanaka, H. Asada and T. Koyanagi "local environment of Mn atoms in IV-VI ferromagnetic semiconductor $Ge_{1-x}Mn_xTe$", J. Appl. Phys., **99,** 08D510 (2006).

[91] Z. Xie, W. D Cheng, D. S. Wu, Y. Z. Lan, S. P. Huang, J. M. Hu and J. Shen " Ab initio study of ferromagnetic semiconductor $Ge_{1-x}Mn_xTe$", J. Phys.: Condens. Matter, **18,** 7171 (2006).

[92] Adrian Ciucivara, Bhagawan R. Sahu and Leonard Kleinman, "Density

functional study of $Ge_{1-x}Mn_xTe$", Phys. Rev. B, **75,** 241201(R) (2007).

[93] Y. H. Zhao and B. G. Liu, "High spin polarization in ternary Ge–Mn–Te compounds based on rocksalt semiconducting GeTe", J. Phys.: Condens. Matter **20,** 135225 (2008).

[93] Y. Fukuma, H. Asada, N. Nishimura and T. Koyanagi, "Appearance of ferromagnetism by crystallizing a-$Ge_{1-x}Mn_xTe$", Physica E, **10,** 268 (2001).

CHAPTER 3 EXPERIMENT PROCEDURES FOR EPITAXTIAL GROWTH

3.1 Molecular-beam epitaxy (MBE) as a tool for epitaxial growth

3.1.1 Introduction

Molecular beam epitaxy (MBE) is a widely used method to deposite high quality thin epitaxial semiconductor structures via the atom-atom interaction, which occurs on the surface of a heated crystalline substrate. It was invented in the late 1960s at Bell Telephone Laboratories by J. R. Arthur and A. Y. Cho [1-3] to grow the crystalline GaAs epitaxial layers. Since then, MBE has become one of the most important epitaxial growth techniques both in research and in production. The advances in MBE have ushered in a new era of growth concepts and device technology, such as bandgap engineering, quantum structures, quantum phenomena, delta doping, suerlattice and strained layer structure [4]. The major advantages that make MBE a supreme tool for basic researches as well as device productions are summarized as follows. Firstly, MBE allows a very precise control of layer thickness and dopant concentration down to the atomic scale. Secondly, MBE is one of the physical vapor deposition techniques. Compared with chemical vapor deposition growth techniques such as MOCVD [5] and Aerosol assisted CVD (AACVD) [6], there is no complicated chemical reaction on the substrate surface in MBE, which facilitates the analysis of growth processes such as surface migration and dopant incorporation. Last but not the least, the ultra

high vacuum (UHV) environment in the growth chamber allows the application of various *in-situ* measurement techniques to study the crystal growth processes. At the same time, these measurements can be used to implement real-time feedback loops for growth control.

3.1.2 Epitaxial growth mechanism

Epitaxy is a process to grow oriented or single-crystalline thin film on a monocrystalline substrate. There are generally two kinds of epitaxial growth, namely homoepitaxy and heteroepitaxy. Homoepitaxy refers to the case when the deposited thin film and substrate are same kinds of material. On the other hand, heteroepitaxy refers to the case when the deposited thin film and substrate are different kinds of materials. In this project, heteroepitaxy is utilized to grow GeMnTe thin films on the BaF_2 substrate. Figure 3-1 shows the three possible growth modes in heteroepitaxy [7]. As shown in Fig. 3-1 (a), Frank-van der Merwe mode refers to the successive addition of 2-D layers to the substrate crystal. The second mode, Volmer-Weber as shown in Fig. 3-1 (b), will occur when the added material can minimize its free energy by trading increased surface area for decreased interfacial area, forming an island structure like water droplets on glass. A third mode called Stranski-Krastanow as shown in Fig. 3-1 (c) will happen when the added material's lattice spacing has a mismatch with that of the crystalline substrate. In this process, growth starts with a strained 2-D wetting layer, but islands form after the first few monolayers. The driving force for island formation is the incorporation of dislocations within the

islands to relieve stress.

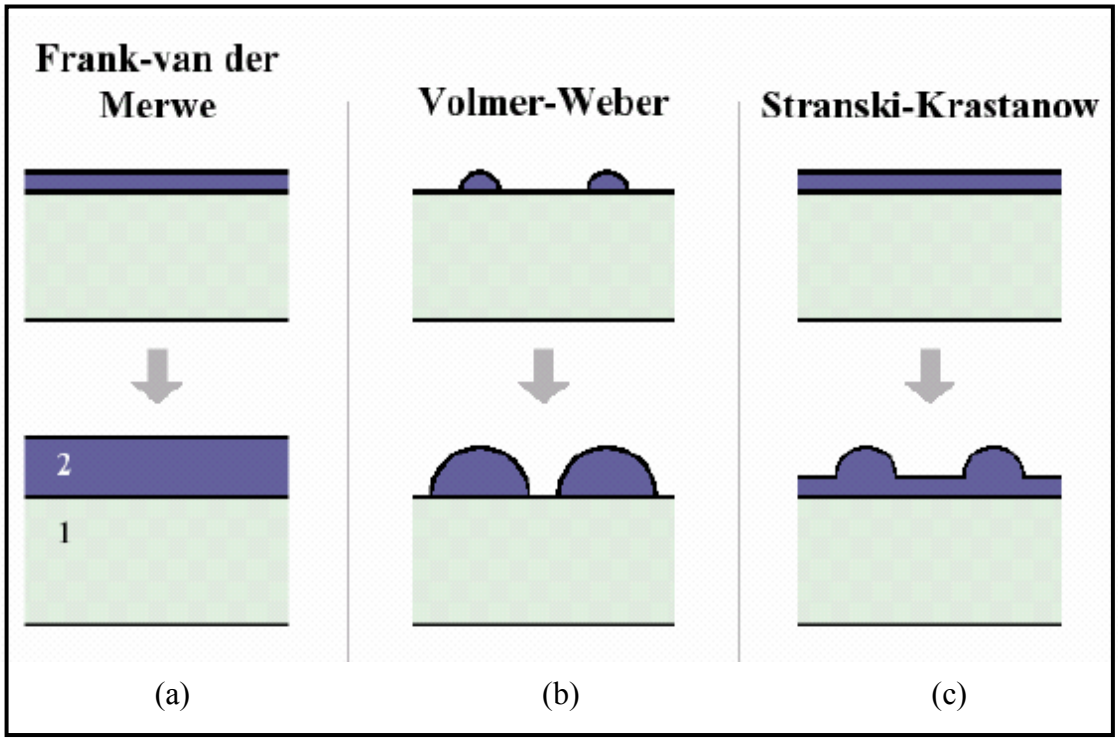

Figure 3-1 Diagram of three heteroepitaxy growth modes: (a) Frank-van der Merwe mode, (b) Volmer-Weber mode and (c) Stranski-Krastanow mode.

The crystal lattice mismatch [8] is a very important parameter in the epitaxial film growth since the epitaxial growth will be affected by the mismatch ratio which can be expressed in the following form:

$$\text{Mismatch ratio } f = \frac{a_s - a_f}{a_s}, \tag{3-1}$$

where a_s and a_f are the lattice constant of the substrate and the film, respectively. The limit of lattice mismatch for epitaxial growth is about 7%. If the lattice constant of substrate and thin film are matched, the growth will be perfect without strain. If the mismatch is small, the film will be coherently strained. On the contrary, there will be mismatch dislocation if the mismatch is large. In this situation, a buffer layer is

normally required. The buffer layer should have better lattice match with both the targeting material and the substrate. If the buffer layer is thick enough, it will perform like a virtual substrate.

3.2 MBE system

3.2.1 Main system description

In this work, ULVAC (model: MBC-1000-2C) solid-source molecular-beam epitaxy system is used in the growth process. Figure 3-2 shows the schematic diagram of this MBE system [9]. It consists of a preparation chamber and a UHV growth chamber, each of which is connected to a turbo-molecular pump and an oil rotary pump. Besides, the growth chamber is also connected to a titanium getter pump (TGP) and a sputter ion pump (IP) to achieve UHV. Normally, the pressure in pre-chamber can reach 10^{-5} Pa while the pressure in growth chamber can reach 10^{-9} Torr with liquid nitrogen cooling during the growth process. The system has seven Knudsen effusion cells (K-cells) and one valved-cracker effusion cell to hold the sources. Each of them has its own mechanical shutter to control the on/off state of the beam flux. The operation of the MBE system can be carried out through the touch-panel control board as well as computer automation.

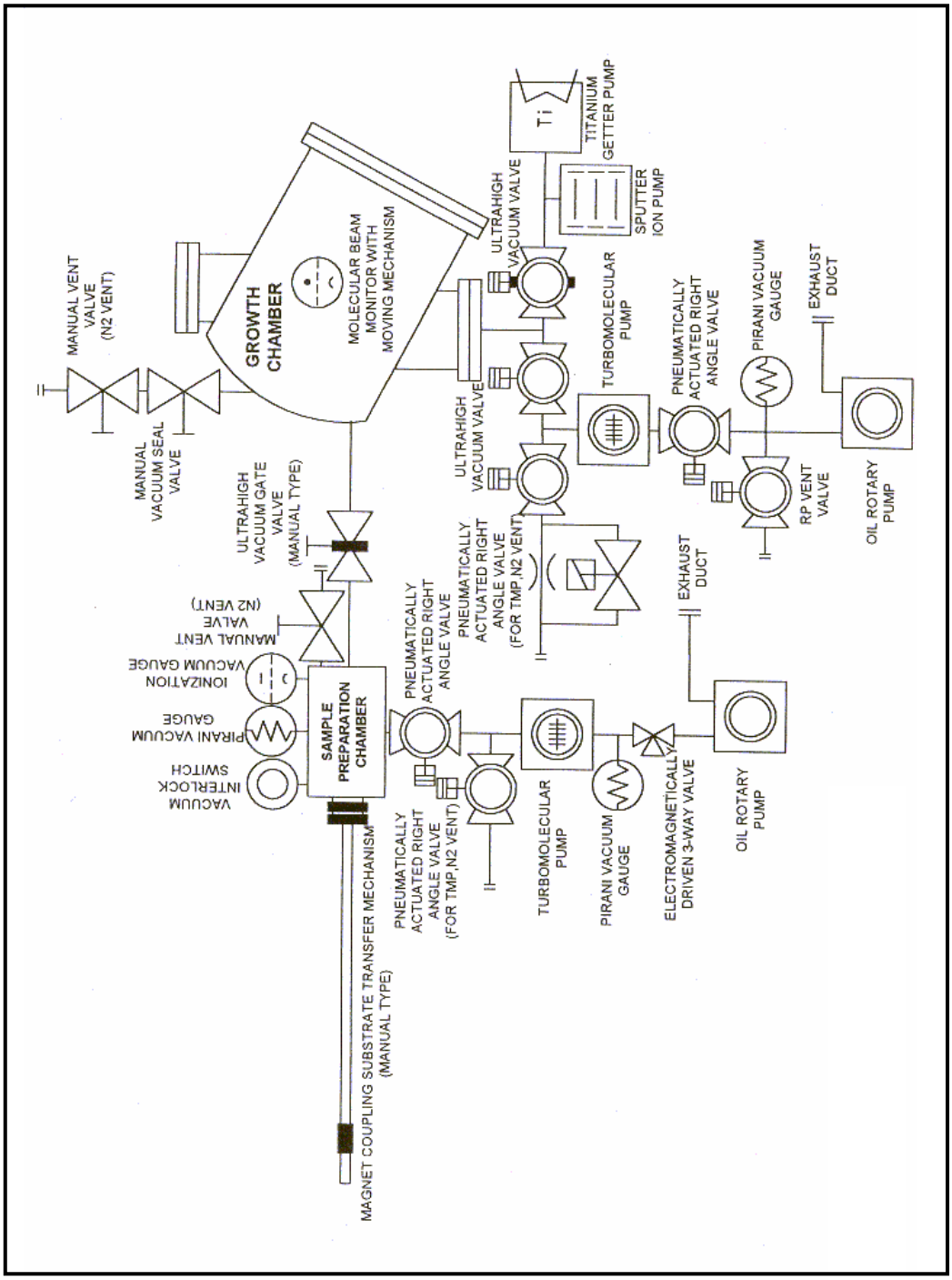

Figure 3-2 Schematic diagram of the ULVAC MBE system [9].

Figure 3-3 shows the schematic diagram of a MBE growth chamber. In the growth chamber, the substrate is placed in a special holder, which faces the molecular effusion K-cells. There is a heater behind the holder, so that the substrate's temperature (T_S) can be fixed at an optimum value for the epitaxy growth. The T_S is measured by a thermocouple located at the center of the substrate heater. In addition, the growth chamber also incorporates a Reflection High-Energy Diffraction (RHEED) system for *in-situ* film quality monitoring. The electron gun reaches the surface of the film at a grazing angle, and the diffraction pattern can be observed from the RHEED screen.

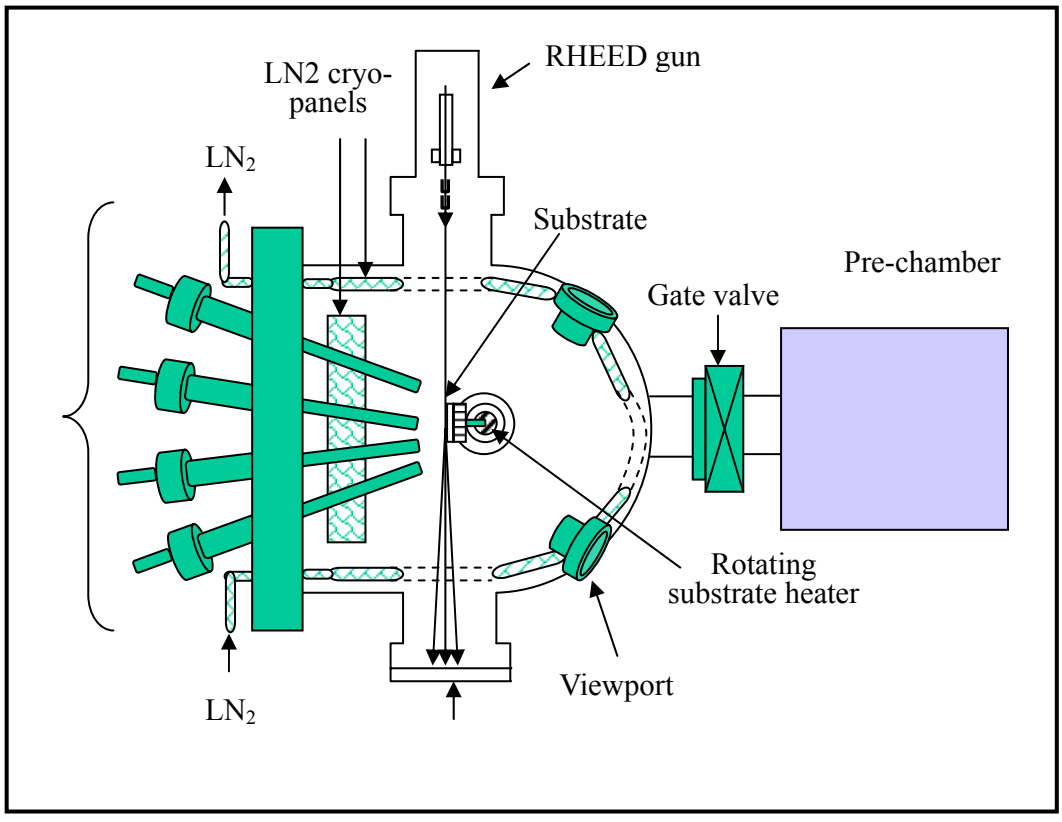

Figure 3-3 Schematic diagram of the MBE growth chamber

3.2.2 Knudsen Effusion Source Cells

The molecular beams are generated from thermally evaporated elemental sources, but other kinds sources are also widely used, including metal-organic group III precursors (MOMBE), gaseous group V hydride or organic precursors (gas-source MBE), or some combination (chemical beam epitaxy or CBE). To obtain high-purity layers, it is critical that the material sources are extremely pure and the entire process is carried our in an ultra-high vacuum environment. The solid source materials such as Cr, Mn, Co, Cd, Zn, and Ge, are held in an inert crucible heated by a resistance heater source and a thermocouple is used to provide the temperature feedback.

3.2.3 Valved-Cracker Effusion Cell

Unlike other sources such as Mn and Ge which use K-cells, the valved-cracker effusion cell is used for Te source. The valved-cracker used in our system is EPI-500V-Te as shown in Fig. 3-4. The reason for using valved cracker is that cracked tellurium molecules are likely to have higher sticking coefficients than the uncracked counterparts. More importantly, cracker cell provides better controllability and reproducibility of the flux in controlling the composition of compound tellurium [10]. The Te source in the EPI valved-cracker can be controlled manually via a micrometer valve actuator or automatically by a servo-motor controller (SMC). In normal situation, the idling temperature of the craker zone is maintained at 300°C, while the temperature of the bulk crucible is maintained at 150°C. During the growth, the temperature of the bulk zone and cracker zone are raised to the desired values. The

tellurium particles are split into tellurium molecules when they pass through the cracker zone to the growth chamber. The valved-cracker uses its own DC power supply and water-cooling system, which help the crucible to maintain a stable temperature. Because of the complicated structure of cracker zone, the valved-cracker has much larger surface area than conventional effusion cells. Therefore, the pumping down and outgassing process requires longer time.

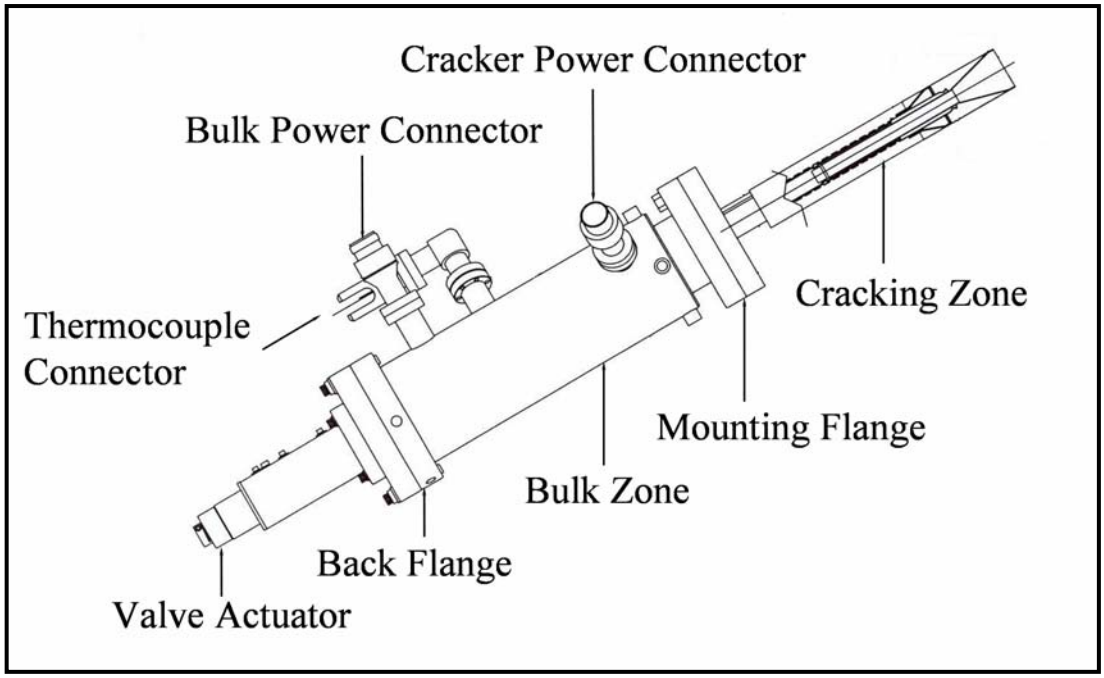

Figure 3-4 Overview of EPI-500V valved-cracker cell

3.2.4 Reflection-high Energy Electron Deffraction (RHEED)

The most important advantage of MBE is that it allows the growth of crystalline layer combinations with accurate dimension control. This precise control would be impossible without those accurate characterization techniques like reflection high-energy electron diffraction (RHEED) [11]. RHEED is a powerful technique that can provide high resolution down to atomic scale while at the same time also fully compatible with the crystal growth process. It is used for the study of surface structures as well as surface phase transitions. RHEED is sensitive to surface changes, either due to structure changes or due to adsorption. Therefore, it is widely used as a real-time *in-situ* characterization tool to monitor the crystal growth. A typical RHEED measurement system consists of an electron gun, a phosphor screen with image-processing hardware and software. Figure 3-5 illustrates a simplified schematic diagram of a RHEED system. A high-energy beam (3-100keV) from the electron gun is incident on the sample surface at a grazing angle of 0.5^{o}-2.5^{o}. The electrons are diffracted by the crystal structure of the sample and then impinged on a phosphor screen mounted opposite to the electron gun. Compared with the low-energy electron diffraction (LEED), the higher-energy electrons used by RHEED will sharpen the picture. Furthermore, the lower angle makes the electrons just pass a few atomic layers into the crystal, which makes RHEED pictures only represent the structure of the surface, not the whole crystal.

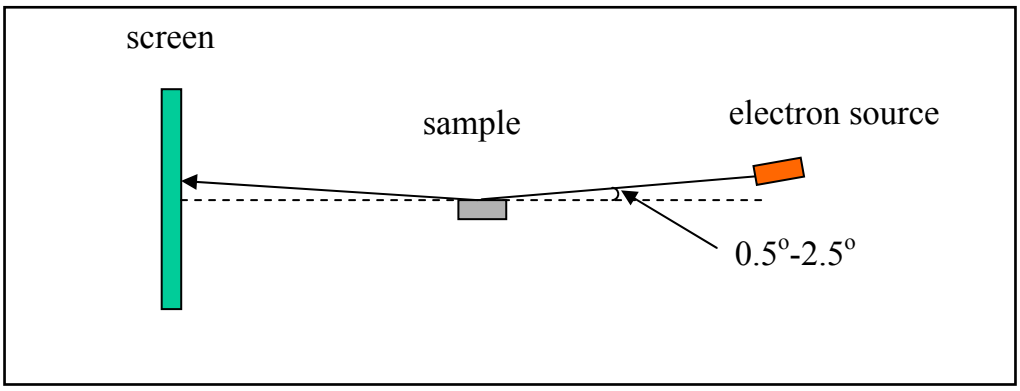

Figure 3-5 Schematic diagram of a RHEED system.

3.3 Growth Preparation and Procedures

3.3.1 Growth preparation

A clean surface is an important prerequisite for epitaxial growth, since contaminants from the air or other sources can easily contaminate a clean wafer and cause crystal defects or degrade the optical and electrical characteristics of the epitaxial layer. Hence, substrates must be cleaned before any deposition is carried out. The substrates used in this project are commercially available polished single crystal of BaF_2 (111) with one-inch in diameter. The substrates are cleaned in Acetone for 10 minutes followed by Methanal for another 10 minutes and then blown dry in N_2 gas before being placed on the Ta holder. The substrate is outgased in the preparation chamber at 300°C for 30 min to eliminate the water-molecules stuck onto the substrate's surface during the cleaning and transferring process. Thereafter, the substrate is transferred into the growth chamber and annealed at a proper temperature until a sharp (1×1) RHEED pattern appeared. The thin film deposition on the substrate

begins after the substrate temperature (T_S) is lowered to the desired growth temperature. Figure 3-6 showed the BaF_2 (111) RHEED pattern along the [100] and [110] azimuths after annealed at 300^{o}C in the growth chamber.

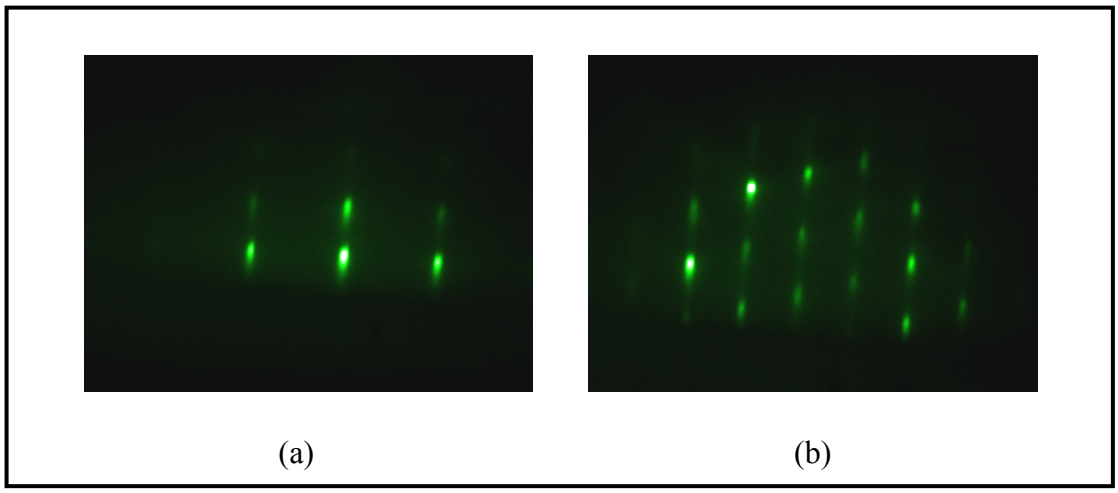

(a) (b)

Figure 3-6 RHEED patterns along the [100] and [110] azimuths of the BaF_2 (111) substrate.

3.3.2 Beam Equivalent Pressure control

Usually, sources such as Ge, Mn, Cr and Co inside the K-cell crucibles are kept at their individual idling temperature at around 200°C. At the idling temperature, the beam Equivalent pressure (BEP) should be in the order of 10^{-10} torr, therefore the source will not lose much. Before the operation, the temperatures of the sources are increased to their operating temperatures. The flux of the K-cells can be controlled by varying their temperatures. Figure 3-7 (a)-(b) shows the relationship of the BEP of Ge and Mn sources versus their effusion cells' temperatures, respectively.

However, for valved-cracker Te source, the idling temperature of cracker zone is maintained at 300°C, and the temperature of the bulk crucible is maintained at 150°C.

Before growth, the temperature of the crucible is increased to 380°C, and the cracker's temperature is increased to 650°C. The servo-motor of the cracker controls the cracker's needle valve so that Te's BEP can be changed. Figure 3-7 (c) shows the relationship of the Te's BEP versus the needle opening-size of the cracker's valve. Although the BEP of all sources have been calibrated after sources loading and system baking, the source's BEP should be calibrated again each time before the growth.

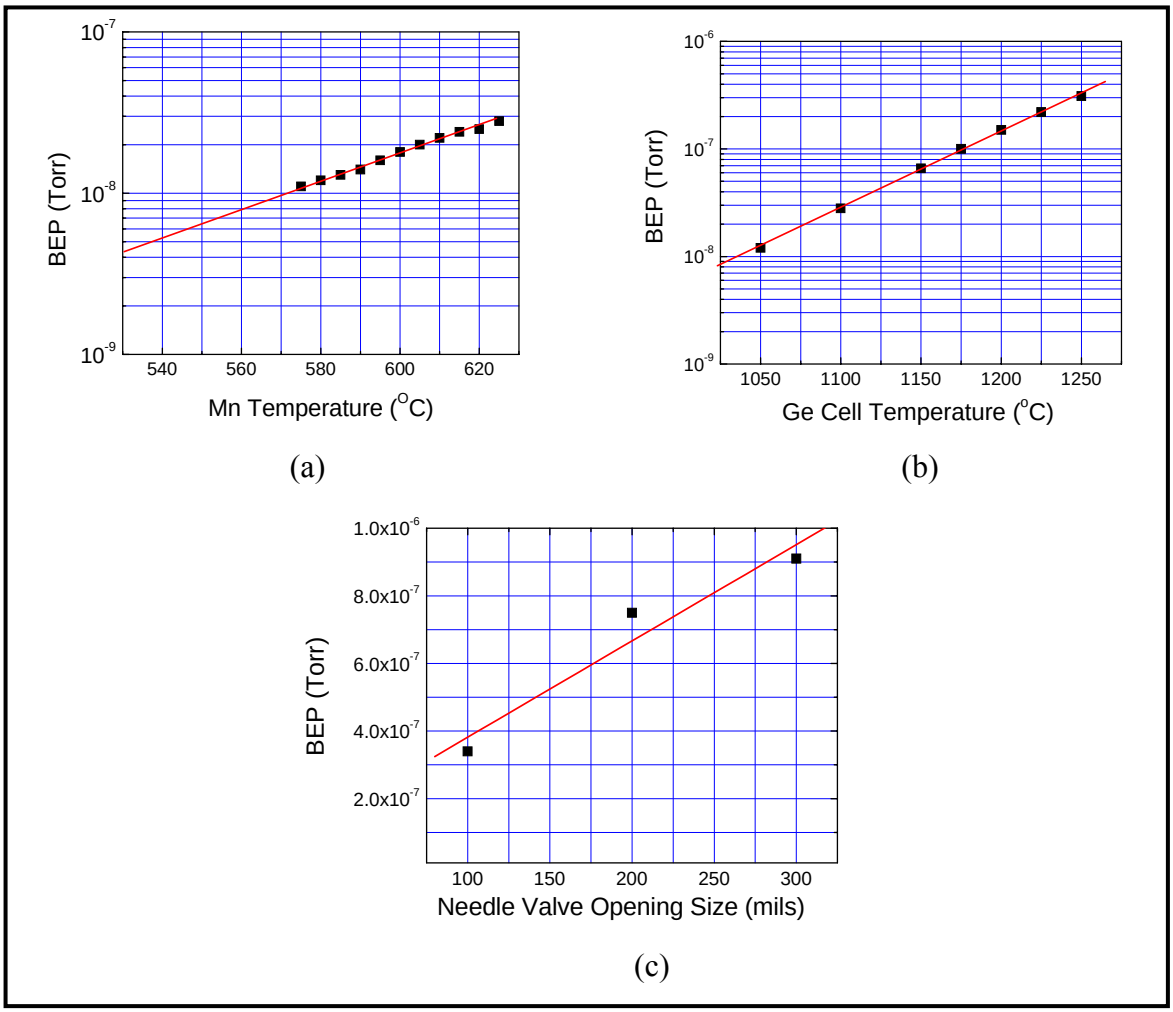

Figure 3-7 (a) BEP versus Mn cell temperature (b) BEP versus Ge cell temperature (c) BEP versus opening-size of needle valve of Te valved-cracker.

Since the ion gauge used in MBE is in essence a density monitor, the relative average velocities of each species must be taken into account when comparing with BEP, i.e. the relative fluxes may be calculated from the relative BEP according to

$$\frac{J_x}{J_y} = \frac{P_x}{P_y} \cdot \frac{\eta_y}{\eta_x} \left(\frac{T_x M_y}{T_y M_x} \right)^{\frac{1}{2}}, \tag{3-2}$$

where J_x is the flux of species X, P_x is its beam equivalent pressure, T_x and M_x are the absolute temperature and molecular weight, respectively. For Ge, Mn and Te, M is 72.59g, 54.94g and 127.6g, respectively. The ionization efficiency relative to nitrogen (η) is given by

$$\frac{\eta}{\eta_{N_2}} = \frac{0.4Z}{14} + 0.6 \tag{3-3}$$

where Z is the atomic number [12]. Given Z of Ge, Mn and Te are 32, 25 and 52, respectively, η of Ge, Mn and Te can be calculated using Eq.(3-3). By substituting the BEP of Ge, Mn and Te at the desired temperatures into Eq.(3-2), the Te/Ge flux ratio and the Te/Mn flux ratio can be calculated. In this way, the flux can be controlled effectively by varying the temperature of the K-cells. The flux ratio is one of the most important parameters to adjust the growth rate and control the film quality in MBE growth.

3.4 Summary

In summary, MBE provides a powerful tool for the epitaxial growth of the thin film due to its UHV environment and precise sources control. The working mechanisms of its main components have been illustrated in this chapter. It

incorporates an *in-situ* RHEED system which is used to monitor the surface reconstructions during the growth. In addition, the valved-cracker used for Te source makes the cracked Te molecules have a higher sticking coefficient and also provides good controllability of the flux.

Before the film growth, BaF_2 (111) substrate has been cleaned by the chemicals and outgasesd in the pre-chamber to eliminate the water-molecules. After transferred into the growth chamber, the substrate is annealed at a proper temperature until a sharp BaF_2 (1×1) RHEED pattern appeared and then the T_S is lowered to the desired temperature for the film deposition. The BEP of the Ge and Mn are controlled by the K-cell temperature. The Te source is controlled by the needle-valve opening size of the cracker cell. The relative flux ratio can be obtained from the relative BEP.

References:

[1] A. Y. Cho, "Morphology of Epitaxial Growth of GaAs by a Molecular Beam Method: The Observation of Surface Structures" J. Appl. Phys. **41**, 2780 (1970);

[2] A. Y. Cho, "GaAs Epitaxy by a Molecular Beam Method: Observations of Surface Structure on the (001) Face" J. Appl. Phys., **42**, 2074 (1971);

[3] A. Y. Cho, "Growth of Periodic Structures by the Molecular-Beam Method" Appl. Phys. Lett. **19**, 467 (1971).

[4] Alfred Cho., Molecular beam epitaxy N.Y. American Institute of Physics, (1994).

[5] http://www.phys.ksu.edu/personal/mnakarmi/MOCVD/mocvd.html

[6] Toivo T. Kodas and Mark J. Hampden-Smith, Aerosol processing of materials,

New York : Wiley-VCH, (1999).

[7] R. J. Nicholas, E. Bunge, H. Meyer and H. Baumgartl, “Classification of Growth Behaviour for Copper on Various Sbstrates with In-situ Scanning Probe Microscopy”, Surface Science, **335**, 110 (1995).

[8] M. Ohring, The materials science of thin films, Boston: Academic Press, (1992).

[9] ULVAC MBC-1000-2C Molecular Beam Epitaxial Growth System manual.

[10] F. J. Bartoli, Jr., H. F. Schaake and J. F. Schetzina, Properties of II-VI semiconductors: bulk crystals, epitaxial films, quantum well structures, and dilute magnetic systems, (1990).

[11] Wolfgang Braun, Applied RHEED- Reflection High-Energy Electron Diffraction During Crystal Growth, New York : Springer, (1999).

[12] M. A. Herman and H. Sitter, Molecular Beam Epitaxy: Fundamentals and Current Status, New York: Springer, (1996).

CHAPTER 4 CHARACTERIZATION TECHNIQUES

4.1 Introduction

A good understanding of the magnetic and semiconductor behaviors of the ferromagnetic semiconductor (FMS) is very important. As a semiconductor, FMS should maintain the semiconductor crystal structure and has the proper band-gap behavior as well. In addition, as a magnetic material, FMS should also present the magnetic properties. Various characterization methods have been used in this project to determine the magnetic and semiconductor properties of the GeMnTe thin films. As shown in Fig. 4-1, Reflection high-energy electron diffraction (RHEED), X-ray diffraction (XRD) and high-resolution transmission electron microscopy (HRTEM) are employed to investigate the crystal structures. The X-ray photoelectron spectroscopy (XPS) is used to determine the chemical state of the thin film and the optical absorption spectra is used to analyze the optical band-gap of the materials. Superconducting quantum interference device (SQUID) is mainly used to characterize the magnetic properties such as the temperature-dependent magnetization and the field-dependent magnetization. Hall effect, temperature-dependent resistivity (R-T), Anomalous Hall effect (AHE), magnetoresistance (MR) measurements are conducted to determine the transport properties. In addition, the atomic force microscope (AFM) is used to investigate the surface morphology and the surface profiler is used to measure the film thickness. Details for some of the important characterization

methods will be presented in this chapter.

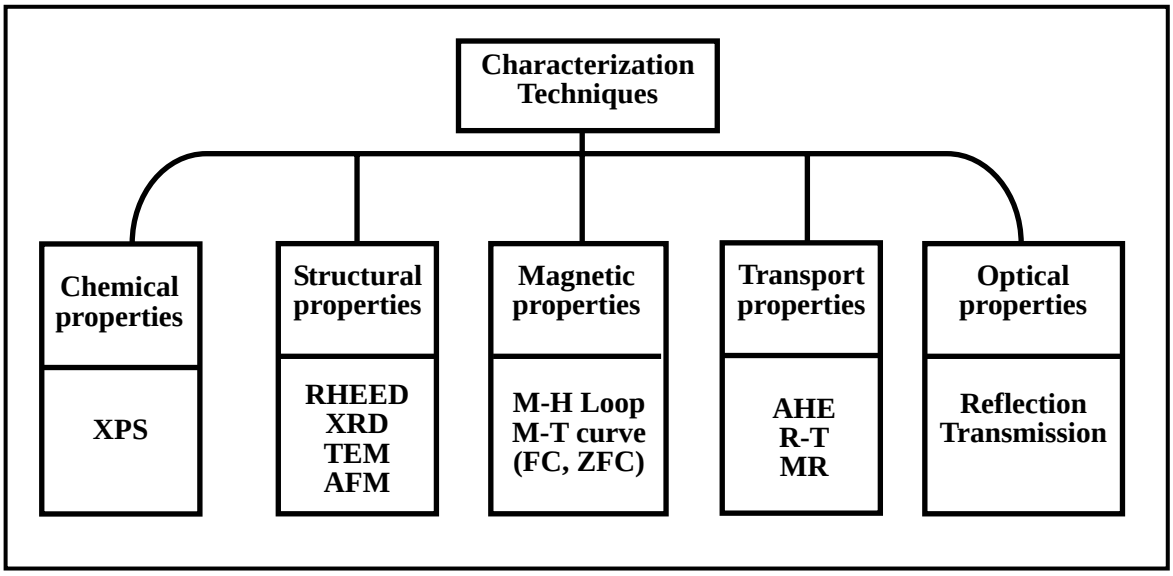

Figure 4-1 Characterization techniques.

4.2 Structural Characterization

4.2.1 Reflection-high Energy Electron Diffraction (RHEED)

The equipment setup and working principles of the RHEED system have been illustrated in Chapter 3. Moreover, a number of simplified kinematical approaches have been introduced to understand the basic idea of RHEED. The simplest theory to describe RHEED is the "geometric theory", which is widely used for experimental calculations. A more elaborated "dynamical theory," is used for more complicated problems [1]. The important information provided by RHEED patterns is regarding the flatness of a surface. If electrons interact only with the first atomic layer of a perfectly flat and ordered surface, the three-dimensional reciprocal lattice points degenerate into parallel infinite rods as shown in Fig. 4-2 (a), visualized as extending infinitely in the directions perpendicular to the surface. However, in reality, the

thermal vibrations, and lattice imperfections will affect the diffraction from a perfectly smooth crystal surface. A diffraction pattern consisting of a series of streaks with modulated intensity is observed as shown in Fig. 4-2 (b). If the growth undergoes the 3D mode, the electrons diffracted from different terraces interact with surface features and terraces. As a result of these interactions, the reciprocal lattice rods can be effectively broadened as shown in Fig. 4-2 (c). When the surface has more than one domain (i.e. randomly oriented crystals), the RHEED image will be the sum of diffraction from all the different regions. This gives rise to a system of concentric rings as shown in Fig. 4-2 (d). It is evident that diffraction from an amorphous surface (such as an oxide on top of a semiconductor) gives no diffraction pattern at all, and only a diffuse background exists. This is important, for example, for evaluating oxide desorption when a new substrate is initially heated up prior to growth in the MBE chamber.

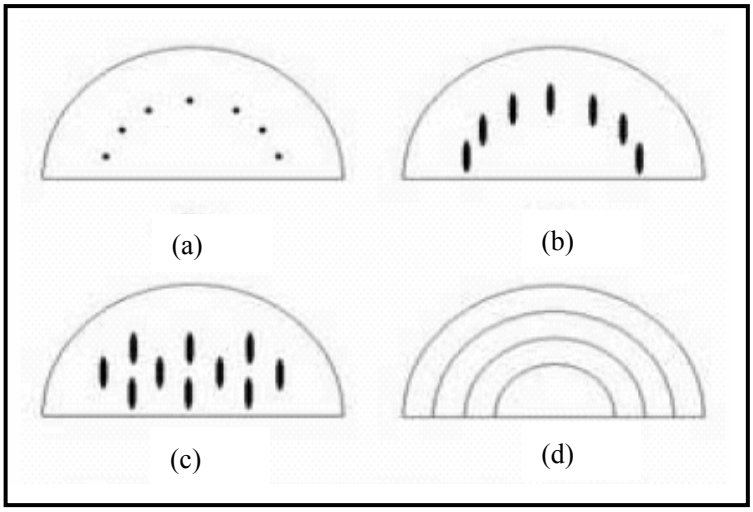

Figure 4-2 Different types of RHEED patterns (a) Ideal smooth surface, (b) Real smooth surface, (c) Diffraction from 3D cluster, (d) Diffraction from polycrystalline and textured surface [Ref 2].

4.2.2 X-Ray Diffraction (XRD)

X-ray is a kind of electromagnetic radiation that can interact with the electrons in atoms. The diffracted waves from different atoms will interfere with each other and generate an intensity distribution. If the atoms are arranged in a periodic fashion, as in crystals, the diffracted waves will consist of sharp interference maxima (peaks) which have the same distribution as atoms. Therefore, X-Ray Diffraction (Philips, X'PERTMRD) is used in this project to identify different crystal planes, possible phases and crystallographic orientation in the films. For a given set of lattice plane with an inter-plane distance of d, the condition for a diffraction (peak) to occur can be simply written as $2d\sin\theta = n\lambda$, (4-1)

which is called the Bragg's law after W.L. Bragg.

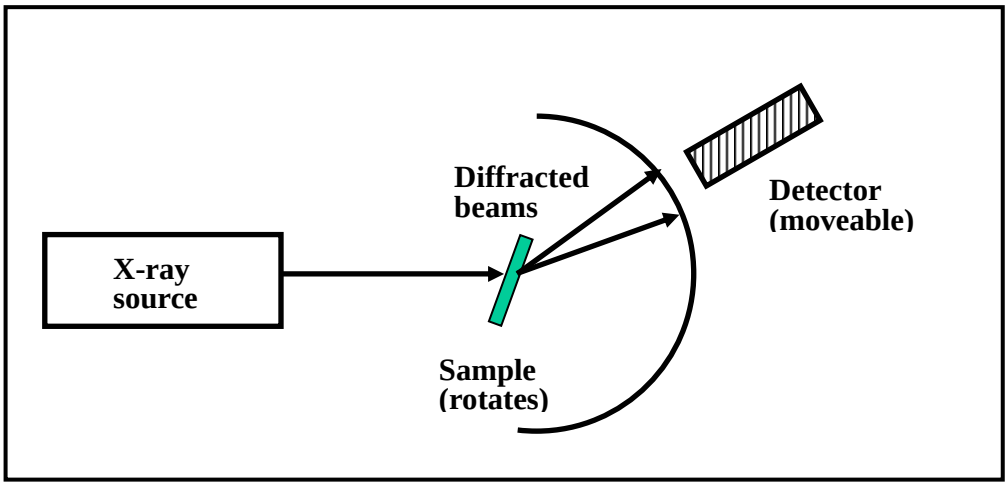

Figure 4-3 Schematic diagram of an X-ray Diffraction system

Figure 4-3 shows the schematic diagram of an XRD system [3]. Normally, a Cu target is used to generate the X-ray beams. The characteristic lines of Cu in our

system contain K_α (0.1541nm) and K_β (0.1477nm) two wavelengths. In this work, the lattice constants could be deduced through θ-2θ scans and it could provide information about lattice mismatch between the thin film and substrate.

4.2.3 Atomic Force Microscopy (AFM)

The Atomic Force Microscopy (AFM) is a high-resolution technique for atomic level surface characterization [4, 5]. The AFM system (Digital Instruments, Digital Instruments Nanoscope III (DI-3100) multimode scanning force microscope) is utilized in this study to generate images and information regarding surface roughness (RMS) and surface topography for the samples. AFM utilizes a probe, controlled by piezoelectric elements, to scan across the sample surface. This probe is a tip on the end of a cantilever that bends in response to the force between the sample and the tip. This force is an inter-atomic force called the van der Waals force. The deflection of the cantilever is then detected by the optical detection method where a fine laser spot is reflected from the back of the reflective cantilever and onto a position-sensitive photodiode. As the cantilever bends and thus the height of the tip changes, the position of the reflected spot will change as well. A schematic diagram of the AFM system is shown in Fig. 4-4. Generally, there are 3 different operational modes for the AFM, namely contact mode, non-contact mode and tapping mode. In this work, the tapping mode is utilized [6].

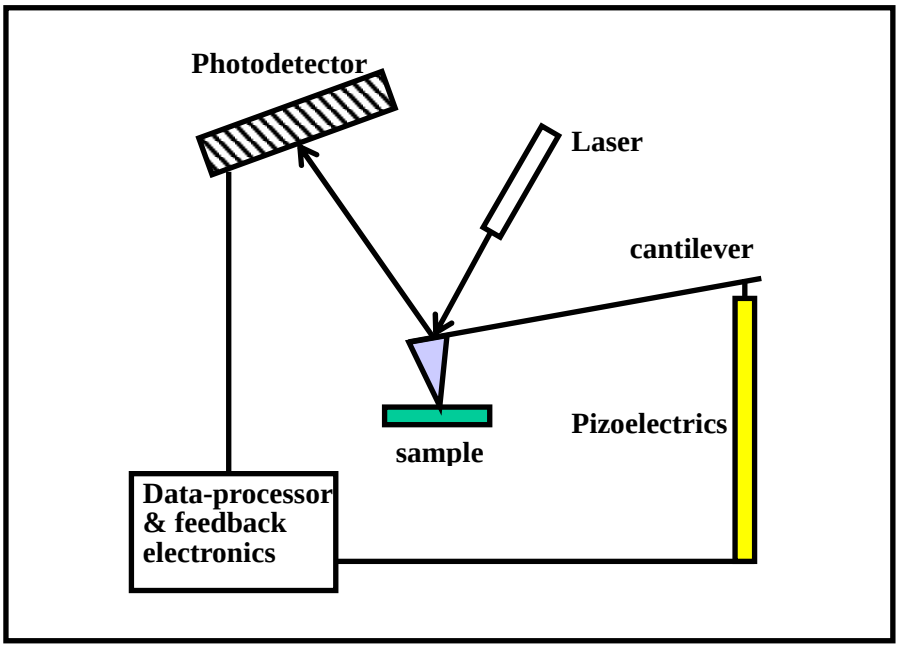

Figure 4-4 Schematic diagram of AFM operation.

4.2.4 X-ray Photoelectron Spectroscopy (XPS)

X-ray Photoelectron Spectroscopy (Physical Electronics Quantum 2000 Scanning Microprobe) is used to characterize the compositions and the electronic state of the thin films. The schematic diagram of the XPS system is shown in Fig. 4-5 [7]. The sample is placed in an UHV chamber and bombarded with monochromatic Al Kα (0.83386 nm, 1486.6 eV) source. XPS is a surface sensitive analytic tool that the X-rays penetrate only the top ~5nm of the sample surface. Electrons are excited by the X-Ray to higher energy levels and the photoelectrons are emitted as a result, and when detected, their kinetic energies can be measured by an electrostatic electron energy analyzer. The kinetic energy (E_k) of the photoelectrons is given by:

$$E_k = h\nu - E_b - E_w, \quad (4\text{-}2)$$

where hν is the energy of the X-ray radiation, E_b is the electron binding energy and E_w

refers to workfunction of the spectrometer [8]. For each element, there is a characteristic binding energy associated with each core atomic orbital. Hence, each element will give rise to a set of characteristic peaks in the photoelectron spectrum. The presence of the energy peaks provides an indication of the existence of a specific element in the sample. In addition, the intensity of the peaks also provides information of the concentration level of each element within the sample.

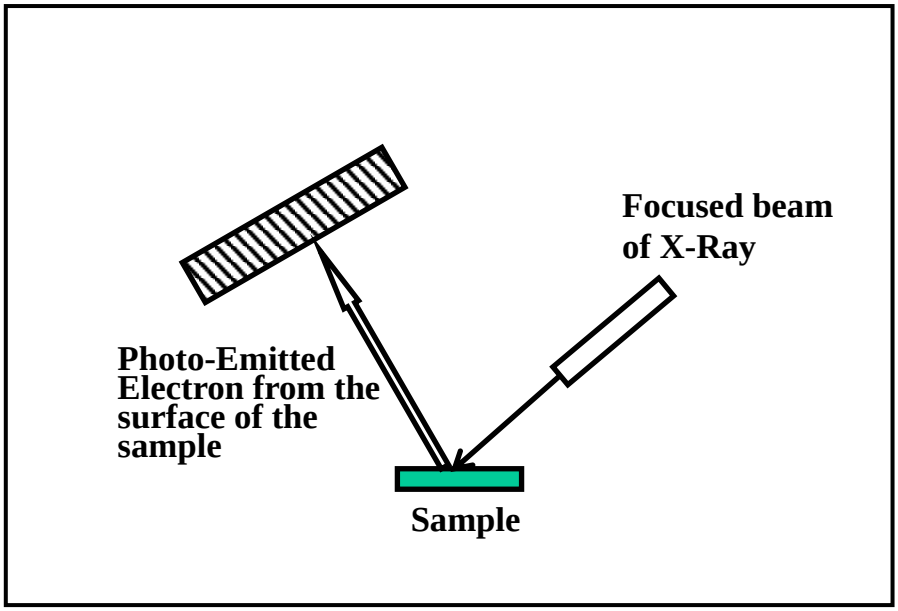

Figure 4-5 Schematic diagram for XPS system.

4.2.5 High-Resolution Transmission Electron Microscopy (HRTEM)

High-Resolution Transmission Electron Microscopy (HRTEM) is the ultimate imaging tool that displays the imaging of the crystallographic structure of the thin film at an atomic scale. It directly shows a two-dimensional projection of all the crystals including the defects. Figure 4-6 shows the schematic diagram of the HRTEM system [9]. HRTEM operates in the same principles as the light microscope but electron is utilized instead of light to get a resolution a thousand times higher than that of the

light microscope. A beam of electrons generated by the eletron gun is transmitted through a specimen to form an image. This image is then magnified to display either on a fluorescent screen or to be detected by a sensor such as a CCD camera.

The HRTEM system (JEOL 2300) is equipped with energy dispersive X-ray spectroscopy (EDS) analysis. EDS is the measurement of X-rays emitted during electron bombardment to determine the chemical composition of materials on the micro- and nano- scale. By determining the energies of the X-rays emitted from the area excited by the electron beam, the elements in the sample can be determined. The detection rate of these characteristic X-rays is used to measure the amounts of elements. After the electron beam is rastered over the target area in the sample, EDS systems can acquire the X-ray maps showing elements spatial variation in the sample. It can detect the full range of elements from Boron (atomic no. 5) to Uranium (atomic no. 92).

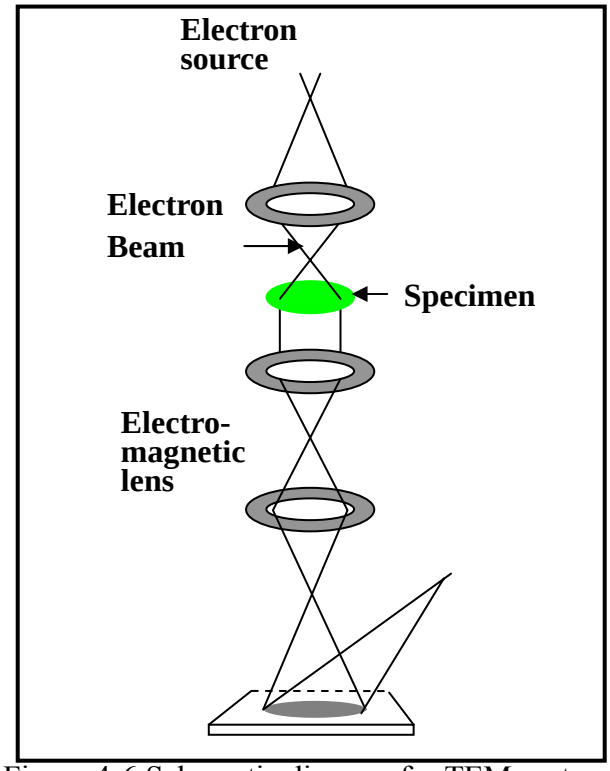

Figure 4-6 Schematic diagram for TEM system

4.3 Magnetic and Transport Characterization

4.3.1 Superconducting Quantum Interference Device (SQUID)

The SQUID magnetometer (Quantum Design MPMS XL-SQUID) is utilized to measure the magnetic properties of the thin films. This technique is highly sensitive to the magnetic field change and the temperature change. The probe contains a high precision temperature control system, allowing measurements from 4.2 K up to 400K. Beyond that temperature, an oven system has to be used with the magnetometer. The probe also contains a superconducting electromagnet to provide a magnetic field (up to 7 Tesla) which is maintained in superconducting state by liquid helium [10]. In addition, a superconducting detection coil is utilized as an extremely sensitive current-to-voltage converter. A schematic diagram is shown in Fig. 4-7 to illustrate the SQUID magnetometer system.

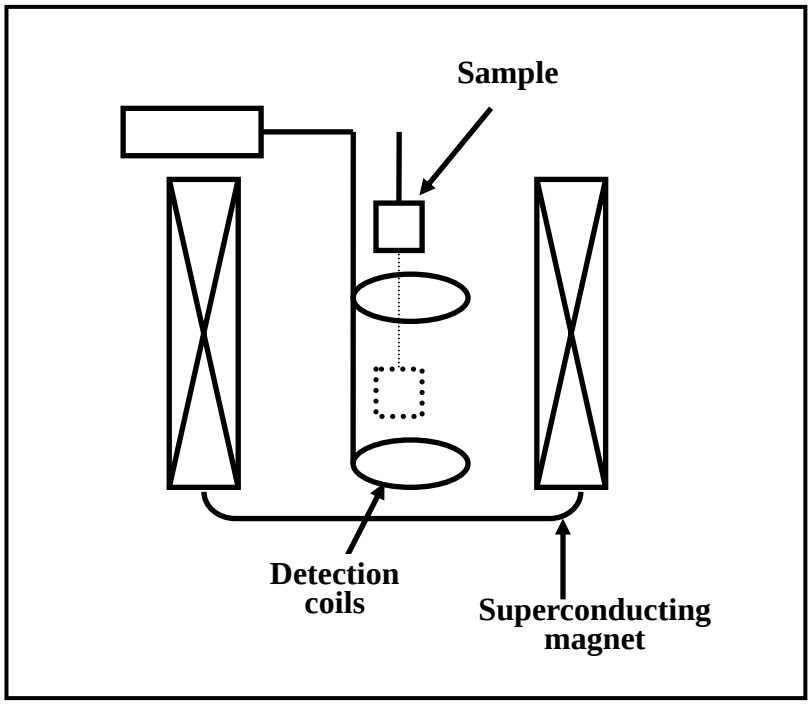

Figure 4-7 Schematic diagram for SQUID magnetometer

The basic principle of SQUID magnetometer is the measurement of the magnetic flux change through the detection coil system [11]. The output signal is proportional to the magnetic moment of the thin film, which is magnetized by the magnetic field from the superconducting magnet. Magnetic fields can be applied parallel or perpendicular to the sample so as to investigate both magnetization-applied field dependence and magnetization-temperature dependence.

4.3.2 Transport Measurement

Hall effect system (Lakeshore 7500) with a maximum magnetic field up to 0.7 Tesla is used to determine the carrier-concentrations of the film at the room temperature. The measurement of thin film's temperature dependent transport property, including AHE, MR and resistivity are conducted in a vacuum cryostat system with magnetic field up to 1 Tesla. A temperature variation between 10K and 300K is controlled by a Lakeshore 340 temperature controller system via the helium compressor and the water chiller. The sample is connected to a Keithly 6221 DC/ AC current source and a Keithley 2182A Nanovoltmeter outside the chamber.

The cryostat system allows the measurement of resistance of a sample across a range of temperature. The van der Pauw configuration is used in the R-T measurement as shown in Fig. 4-8. Gold contacts are deposited using an evaporator on the 4 corners of the sample. Indium wires are subsequently soldered onto the contacts to allow current to flow through the sample. The resistivity of the sample at a given temperature can be calculated via the van der Pauw geometry given by

$$\rho = \pi t / \ln 2 * (V_{43}/I_{12} + V_{14}/I_{23}) \quad (4\text{-}3)$$

where t is the thickness of sample, I_{12} and I_{23} refers to the current across points 1 and 2 and the current across points 2 and 3, respectively; while V_{43} and V_{14} refers to the corresponding voltage across points 3 and 4 and voltage across points 1 and 4, respectively [12].

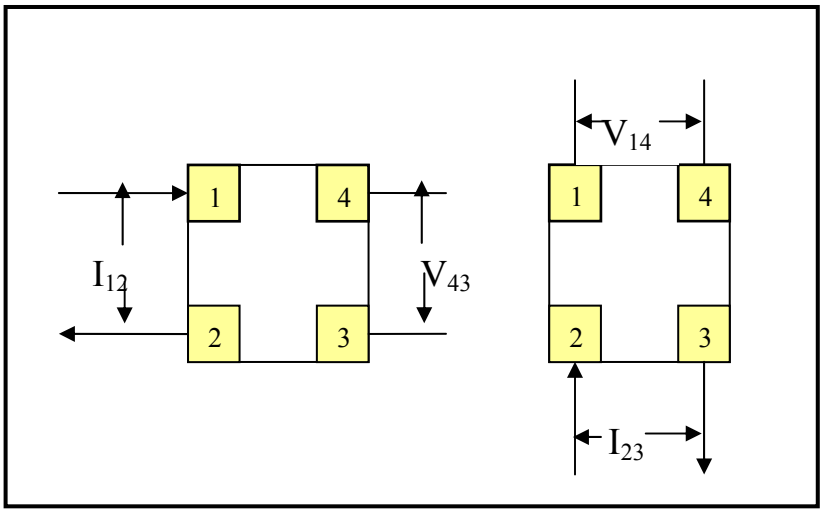

Figure 4-8 Schematic diagram for resistivity measurement

The Anomalous Hall Effect (AHE) measurement also uses the van der Pauw configuration. As illustrated in Fig. 4-9, the external current/voltage sources are applied in perpendicular directions with a magnetic applied field applied in normal direction to the sample surface plane. For example, the current passes through contact 1 and 3 and the voltage measured between contact 2 and 4, as shown in the Fig. 4-9. Therefore, the anomalous Hall resistance R_{xy} can be expressed as: $R_{xy}=V_{24}/I_{13}$.

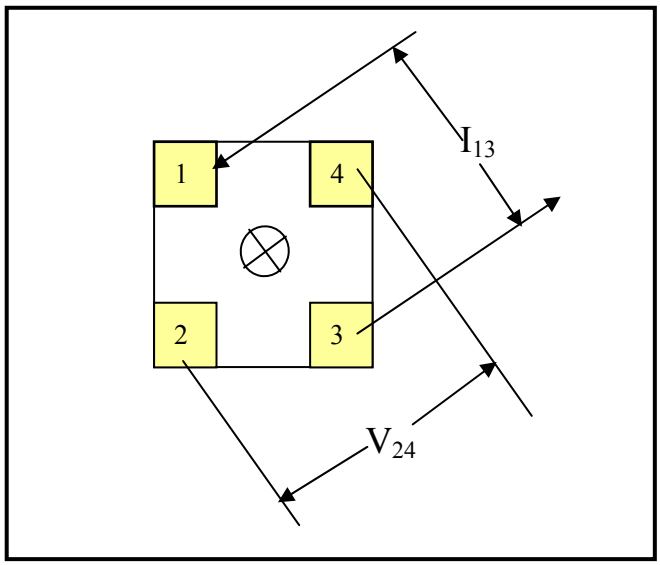

Figure 4-9 Schematic diagram for Anomalous Hall Effect (AHE) measurement

In order to measure the magnetoresistance (MR), linear four probe contacts are deposited in a new configuration as shown in Fig. 4-10, instead of the van der Pauw configuration. The current passes through contact 1 and 4 and the voltage is detected between contact 2 and 3. The magnetic field can be applied either perpendicular or parallel to the sample plane.

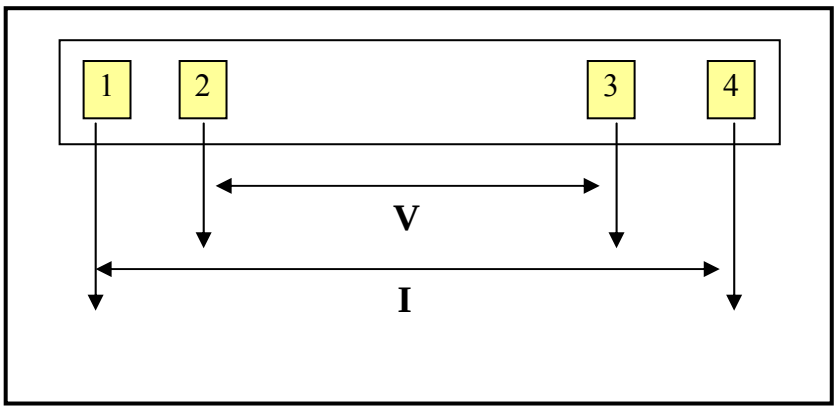

Figure 4-10 Schematic diagram for Magnetoresistance (MR) measurement

4.4 Optical Characterization

The Spectrophotometer (UV-3101PC Spectrophotometer) with wavelength λ from 300nm to 3200nm is used to measure the absorption spectra so as to obtain the absorption coefficient and the optical band-gap of the semiconductors. In a spectrophotometer, a light from the lamp is guided through a monochromator and this light reflected by or passes through the sample is measured with a photodiode or other light sensor. Figure 4-11 shows the schematic diagram of the absorption experiment.

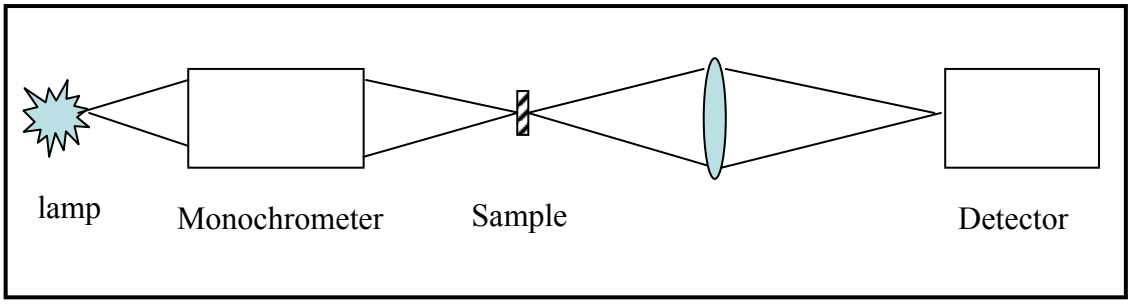

Figure 4-11 Schematic diagram of the absorption experiment.

4.5 Summary

In this chapter, various characterization methods used in determining the magnetic properties and the semiconductor properties of $Ge_{1-x}Mn_xTe$ thin films have been illustrated. The working principles of RHEED, XRD, AFM, HRTEM, XPS, SQUID, Hall Effect, the temperature dependent resistivity, AHE, MR and optical absorption measurement have been briefly described.

References:

[1] Wolfgang Braun , Applied RHEED- Reflection High-Energy Electron Diffraction During Crystal Growth, New York : Springer, (1999).

[2]http://www-drecam.cea.fr/en/Phocea/Vie_des_labos/Ast/ast_sstechnique.php?id_ast=506

[3] http://www.mrl.ucsb.edu/mrl/centralfacilities/xray/xray-basics/

[4] http://invsee.asu.edu/nmodules/spmmod/afm.html

[5]http://www.weizmann.ac.il/Chemical_Research_Support/surflab/peter/afmworks/index.html

[6] Manuals for Digital Instruments Nanoscope III (DI-3100) multimode scanning force microscope.

[7] http://www.answers.com/topic/x-ray-photoelectron-spectroscopy?cat=technology

[8] http://www.chemistry.adelaide.edu.au/external/soc-rel/content/xps.htm

[9] http://nobelprize.org/educational_games/physics/microscopes/tem/index.html

[10] http://www.cmp.liv.ac.uk/frink/thesis/thesis/node59.html

[11] http://hyperphysics.phy-astr.gsu.edu/hbase/solids/squid.html

[12] Lake Shore 7500/9500 Series Hall System User's Manual, Appendix A: Hall Effect Measurements

CHAPTER 5 RESULTS AND DISCUSSION: STRUCTURAL AND OPTICAL PROPERTIES OF $Ge_{1-x}Mn_xTe$ FILMS

5.1 Growth conditions of $Ge_{1-x}Mn_xTe$ Thin Films

5.1.1 Phase diagram of $(GeTe)_{1-x}(MnTe)_x$ system

Germanium monotelluride GeTe is an $A^{IV}B^{VI}$ compound, crystallized in a rhombohedrally distorted rocksalt structure with a lattice constant of $a = 5.979$ Å and a deviation angle of 88^o [1]. In the rock-salt structure, two types of atoms occupy alternate positions on a face-centered-cubic (fcc) lattice. The crystal structure can be described as fcc lattice with a basis of two atoms of two types, i.e., Ge at (000), Te at $\left(\frac{1}{2},\frac{1}{2},\frac{1}{2}\right)$ as presented in Fig. 5-1.

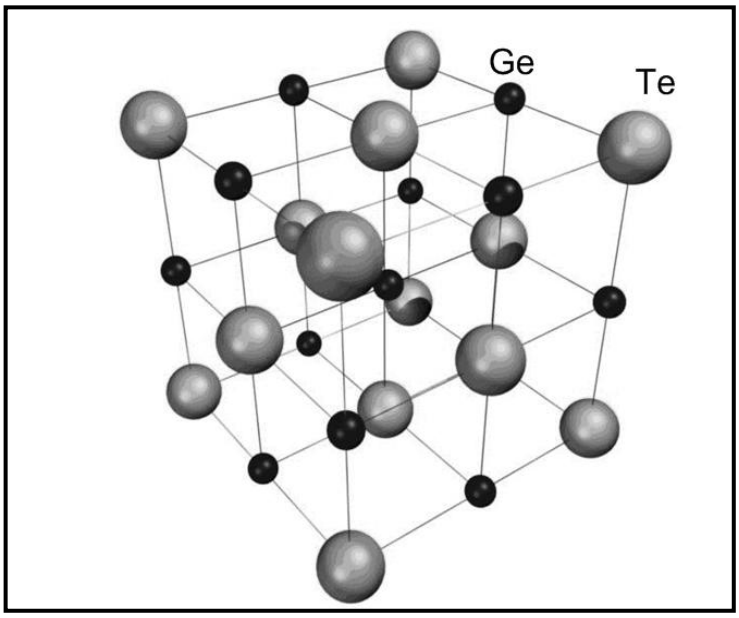

Figure 5-1 GeTe unit cell structure.

Manganese telluride (MnTe), which belongs to the family of manganese chalcogenidses, crystallizes in a hexagonal NiAs structure (with the lattice parameter average values $a = 4.15$ Å and $c = 6.71$ Å) [2]. The stacking configuration of NiAs structure is ABACABAC, with Mn atoms on the A sites and Te on B and C, respectively. The environment of the Mn atoms is fcc-like and the environment of Te atoms is hcp-like as illustrated in Fig. 5-2 (a). However, MnTe can also be obtained in the metastable zinc blende (ZB) phase with lattice constant of a = 6.33Å, when grown in non-equilibrium conditions [3]. The ZB structure can be considered as a close-packed cubic structure with a basis of two atoms: Te at (000), Mn at $\left(\frac{1}{4},\frac{1}{4},\frac{1}{4}\right)$ as illustrated in Fig. 5-2 (b).

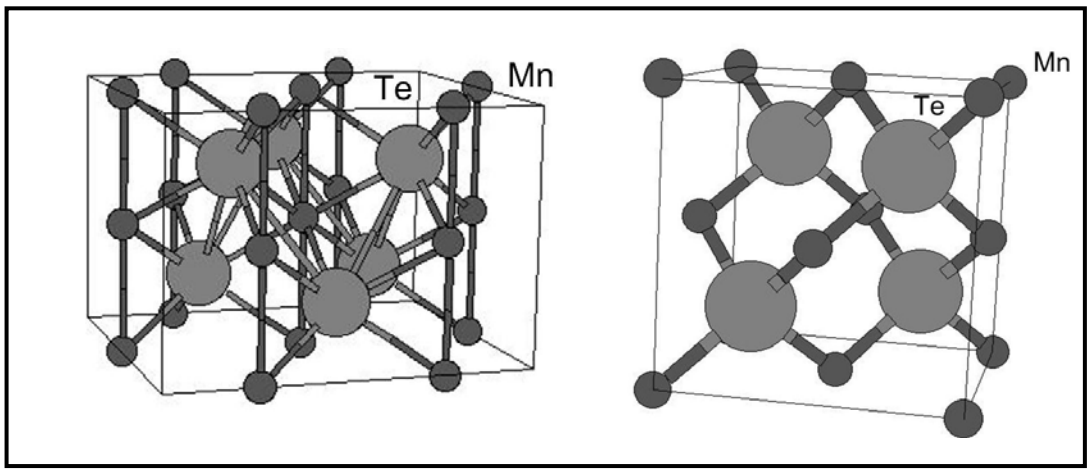

Figure 5-2 MnTe unit cell structure (a) NiAs structure (b) Zinc blende structure.

The phase diagram of the $(GeTe)_{1-x}(MnTe)_x$ system exhibits three stable solid phases at room temperature which become one phase at high temperature, as shown in Fig. 5-3 [4]. The high temperature phase is a simple cubic NaCl structure similar to a large number of chalcogenide compounds. Below 450°C, however, the stable phase

for GeTe is a distorted cubic structure or known as rhombohedral structure with a corner angle of 88°. The rhombohedral distortion decreases rapidly with Mn and vanishes at x = 18%. From 18 to 60%, the phase is the high-temperature cubic NaCl. Beyond 90%, the alloys crystallize into the hexagonal NiAs structure of MnTe, while the region between 60 and 90% consists of two phases, i.e. NaCl+NiAs.

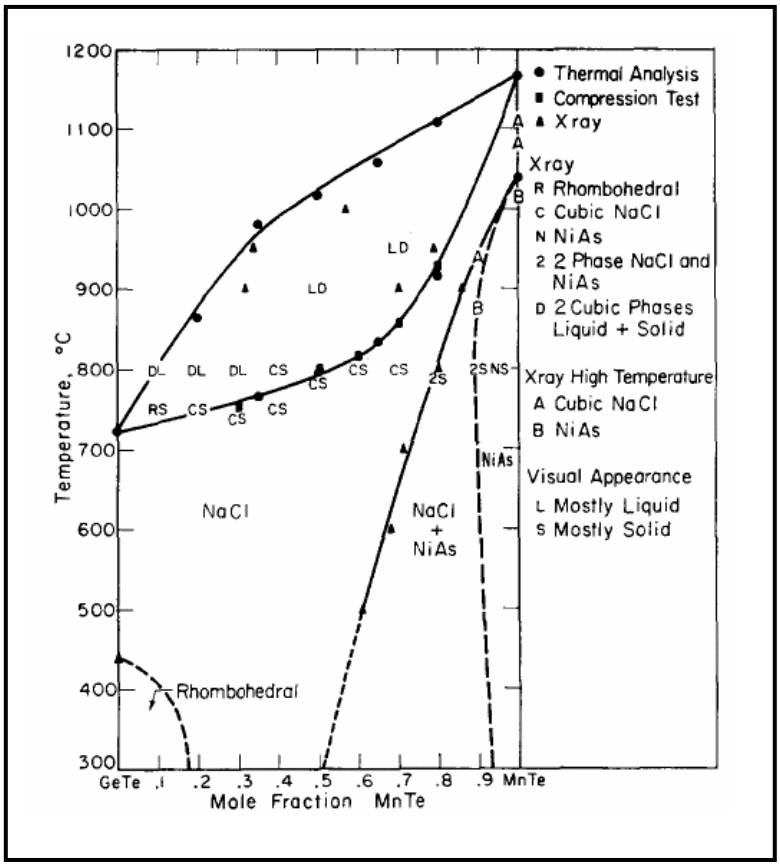

Figure 5-3 Phase diagram for MnTe-GeTe system [Ref. 4]

5.1.2 Growth conditions of $Ge_{1-x}Mn_xTe$ Film

The $Ge_{1-x}Mn_xTe$ thin film growth is performed on the BaF_2(111) substrate, which belongs to the fluorite-type structure with a lattice constant $a = 6.196$ Å [5]. The lattice mismatch between BaF_2 and GeTe atom is around 3%. From our experimental

results, the growth of stoichriometric GeTe film itself is very difficult to achieve using elemental Ge and Te sources. Moreover, GeTe oxidizes spontaneously in the presence of atmospheric air [6]. In most of the IV-VI material MBE growth, IV-VI compound sources are used. For example, SnMnTe was grown using the effusion cells of SnTe, Mn and Te [7], PbMnTe was grown using PbTe and Mn sources [8] and GeCrTe was grown using GeTe and Cr sources [9]. Compared with GeTe material in which Ge and Te atoms are bonded by the chemical reaction, the ionic bonding between Mn and Te atoms is much stronger in MnTe compound. Therefore, MnTe compound should be more stable than GeTe compound. By taking the advantage of the non-equilibrium conditions in the MBE system, a few monolayers of cubic MnTe are grown as a buffer to compensate the substrate surface defects. In addition, since Zinc-blende (ZB) MnTe is an antiferromagnet material [10], the growth of GeMnTe film on the MnTe buffer layer has the potential for future exchange bias study which can be used in the spin-valve applications.

Figure 5-4 shows a time sequence series of RHEED patterns observed during the deposition of MnTe on $BaF_2(111)$ substrate at a substrate temperature T_S=200^oC. The (1×1) RHEED pattern of $BaF_2(111)$ substrate appeared after annealing for 10 min at 300^oC as shown in Fig.5-4 (a). Large spots can be observed in the RHEED pattern which indicates the surface is not perfectly smooth. Along with coverage of two minutes of MnTe (a few MLs) at T_S~200^oC, the RHEED pattern tends to become more streaky. Figure 5-4 (b) shows the RHEED pattern of MnTe follows the pattern of BaF_2, indicating the same crystalline property of MnTe is achieved. However, as

shown in Fig. 5-4 (c), an increase in the number of the diffraction spots tends to appear in the RHEED pattern with the increase of the MnTe thickness. This means that the surface get rougher. Therefore, we limit the growth time of MnTe to 2 mins.

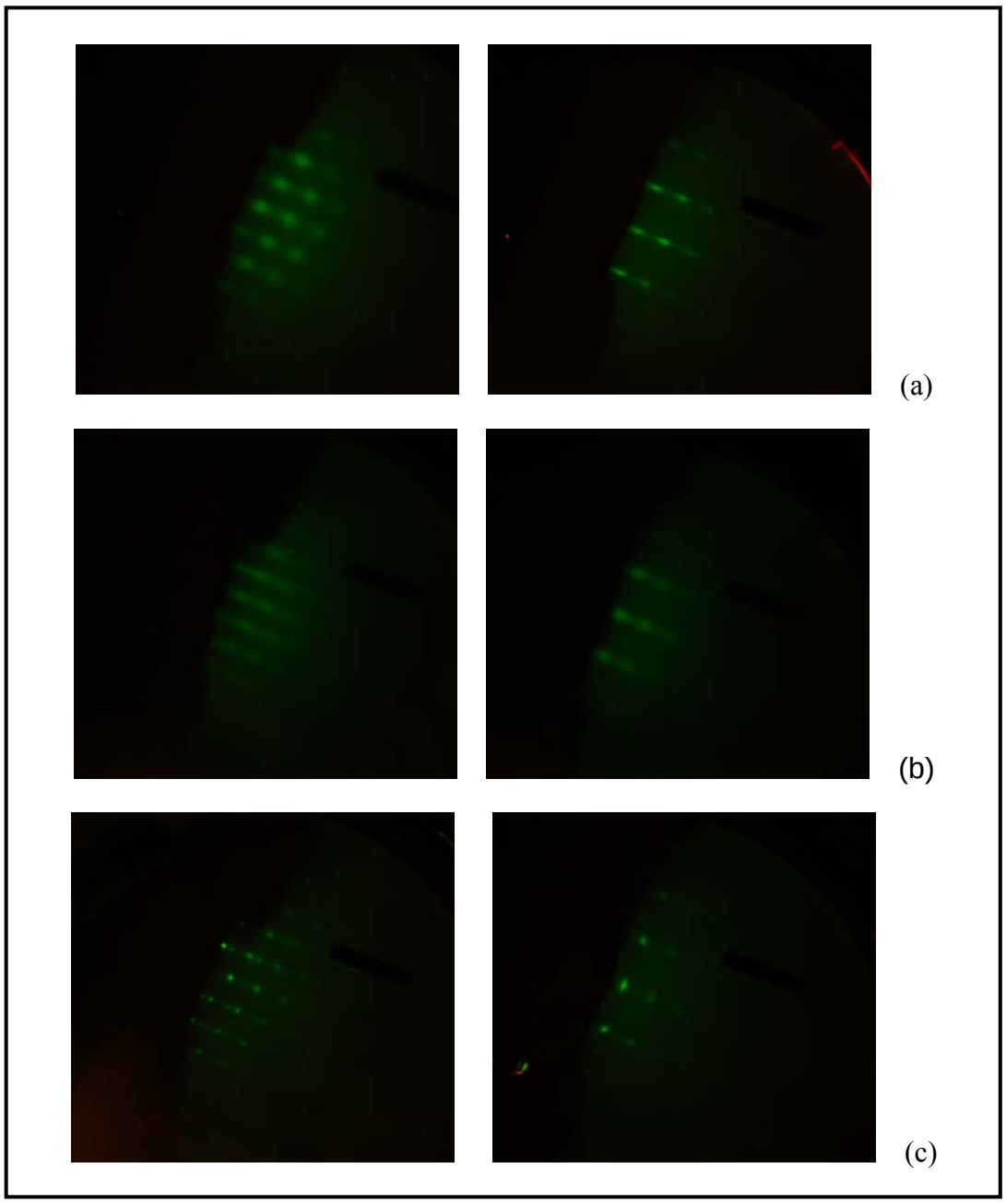

Figure 5-4 RHEED patterns along the [100] and [110] azimuths recorded: (a) BaF_2 (111) substrate. (b) 2 minutes deposition of MnTe at Ts=200°C. (c) 5 minutes deposition of MnTe. The black bar was used as a reference for picture taking.

Two critical parameters; namely, the flux ratio and the growth temperature are optimized during the growth. Since GeTe compound has a relatively low melting temperature of 725°C at the atmospheric pressure so growth at a very high temperature is not appropriate. If the growth temperature is too high, $T_s > 300\ ^oC$, the film contains very few Ge atoms. On the other hand, the substrate should be maintained at a certain temperature to provide the enough kinetic energy for the atoms. If $T_s < 150^oC$, no matter how much the flux ratio changes, we can only obtain polycrystalline growth. Therefore, the most appropriate growth temperature is set to $T_s \sim 200^oC$.

It is known that the bond between Ge and Te atoms is much weaker compared with that between Mn and Te atoms, so usually the Te/Mn ratio is more than 10 times of Te/Ge ratio to achieve 50% of Mn composition in the compound. Furthermore, with large Te/Ge flux ratio, the Te/Mn flux ratio must be increased accordingly. This is equivalent to decreasing the Mn's BEP. On the other hand, the Mn's BEP should be higher than the background pressure (around 10^{-9}) to enhance the calibration accuracy and thin film growth controllability. Thus, there is an optimum range for the Mn's BEP. From our experiment result, we found that the most appropriate flux ratio of Te/Ge~1.5 to 2. By varying the K-cell temperature of Mn from 625°C to 540°C (BEP $5\times10^{-9} \sim 2.7\times10^{-8}$Torr or equivalently the flux ratio of Te/Mn from 13 to 70) at the constant Te/Ge flux ratio, the portion of Mn in the ternary material can be changed.

Figure 5-5 shows a typical time sequence series of RHEED patterns observed during the deposition of $Ge_{1-x}Mn_xTe$ films (x=0.98) on a BaF_2 (111) substrate at 200°C. A well defined RHEED pattern (1×1) of the BaF2 (111) substrate in [100] and [110] directions appeared after annealing for 10 min at 300°C as shown in Fig. 5-5 (a). The RHEED patterns become diffused when the temperature lowers to 200°C, as shown in Fig. 5-5 (b). However, with coverage of few ML of the MnTe, the RHEED pattern becomes streaky [Fig. 5-5 (c)]. With the deposition of $Ge_{1-x}Mn_xTe$, very weak line and spots start to appear. The growth is subsequently resulted in an island growth-mode as shown in Fig. 5-5 (d). Diffraction spots become more intense with increasing thickness. The spot-like diffraction pattern is preserved throughout the entire growth process, indicating no apparent change in the surface structure of the film.

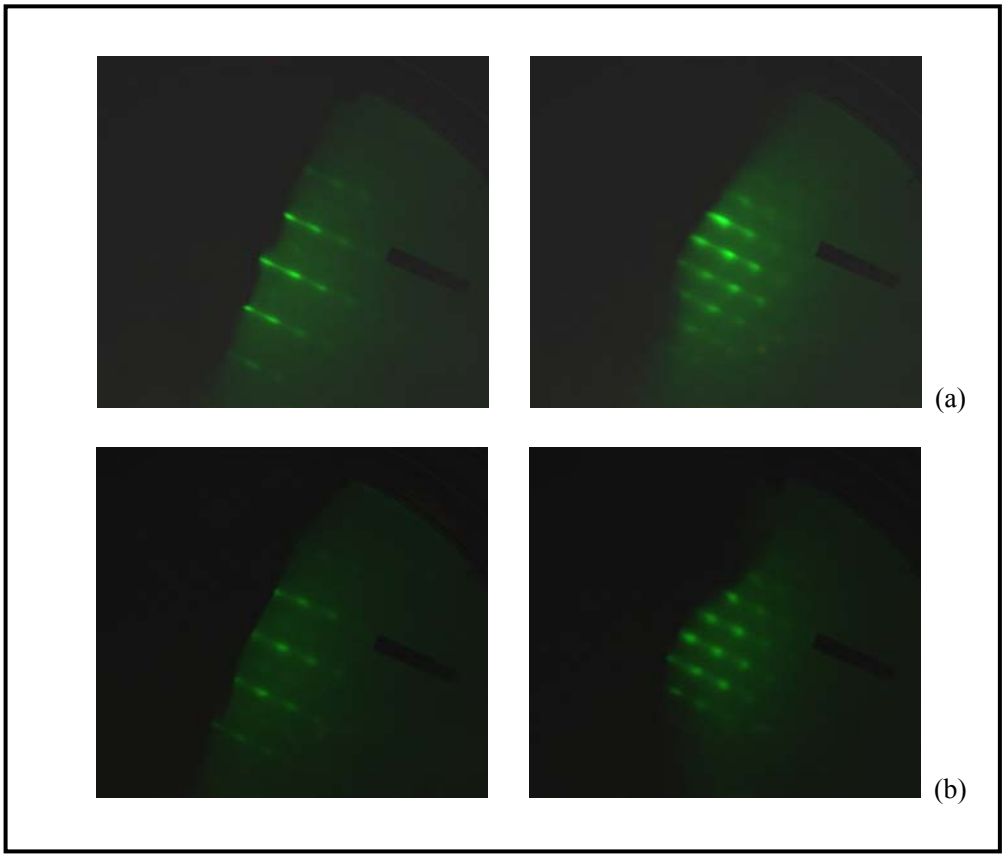

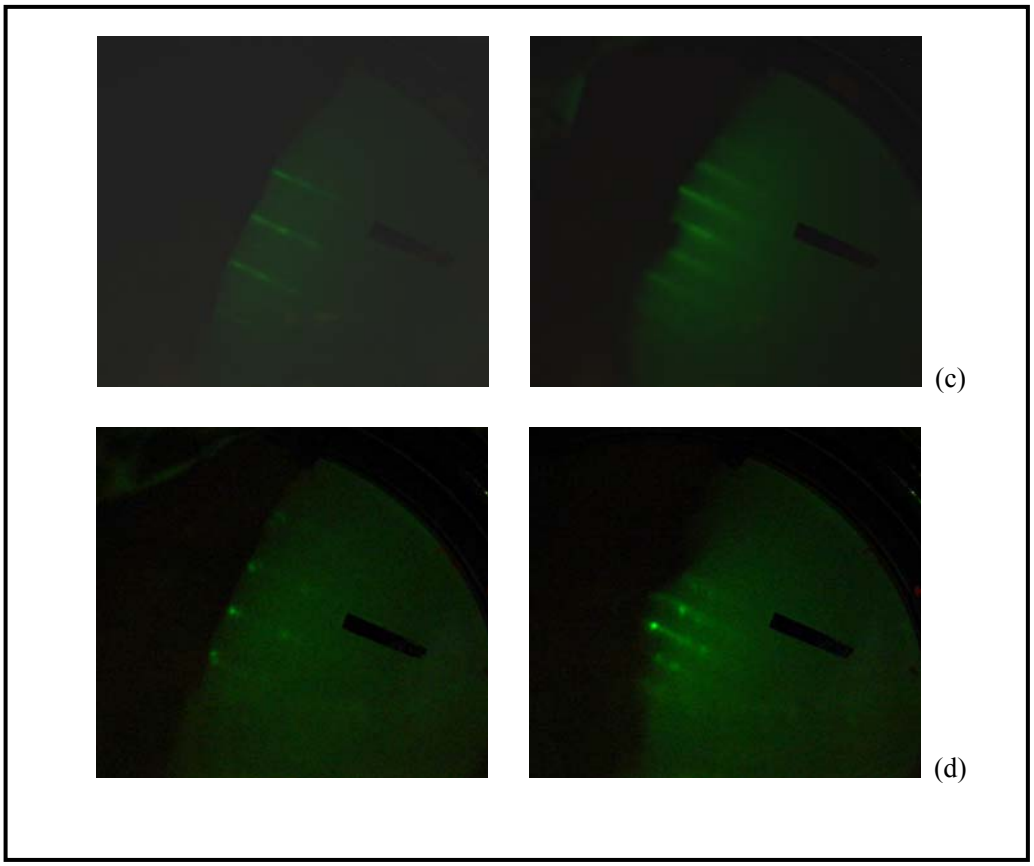

Figure 5-5 RHEED patterns along the [100] and [110] azimuths recorded: (a) BaF_2 (111) substrate annealing at 300°C. (b) BaF_2 (111) substrate at 200°C. (c) after 2 minutes deposition of MnTe at Ts=200°C. (d) after 2h deposition of $Ge_{1-x}Mn_xTe$ (x=0.98). The black bar is used as a reference for picture taking.

Compostional characteristics of the deposited $Ge_{1-x}Mn_xTe$ films are determined by the XPS measurement. Figure 4-6 shows the XPS result of $Ge_{1-x}Mn_xTe$ film grown with the Mn cell temperature T_{Mn}=625°C. The measurement is obtained after pre-sputtering 10nm to 15 nm to eliminate the surface oxidation and contamination. The atomic percentage of Mn2p3, Ge2p3 and Te3d5 is 41.5%, 1% and 50.4%, respectively. Therefore, Mn composition deduced from Mn%=Mn/(Mn+Ge) is x=0.98.

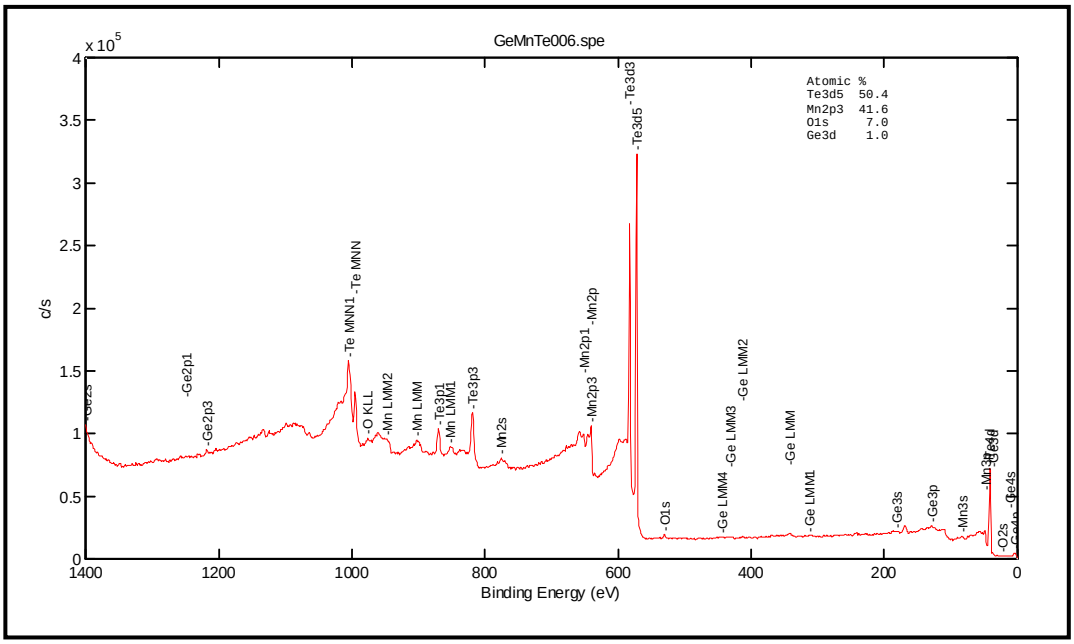

Figure 5-6 XPS result of $Ge_{1-x}Mn_xTe$ film with T_{Mn}=625°C after pre-sputtering for 10nm~15nm.

Figure 5-7 shows the XPS depth profile measurement of $Ge_{1-x}Mn_xTe$ thin film with a Mn cell temperature T_{Mn}=625°C. The contents of film and the substrate are clearly observed. The surface of the film contains lots of carbon and oxygen but they get much less after further sputtering of 10nm. The film thickness is around 100nm and the substrate elements Ba and F are diffused into the film. No obvious buffer layer starting and ending point can be observed because only few monolayers MnTe buffer have been deposited. The inset in Fig. 4-7 shows the relative Mn depth composition deduced from Mn%=Mn/(Mn+Ge). The dash line at around 97% is consistent along the whole film.

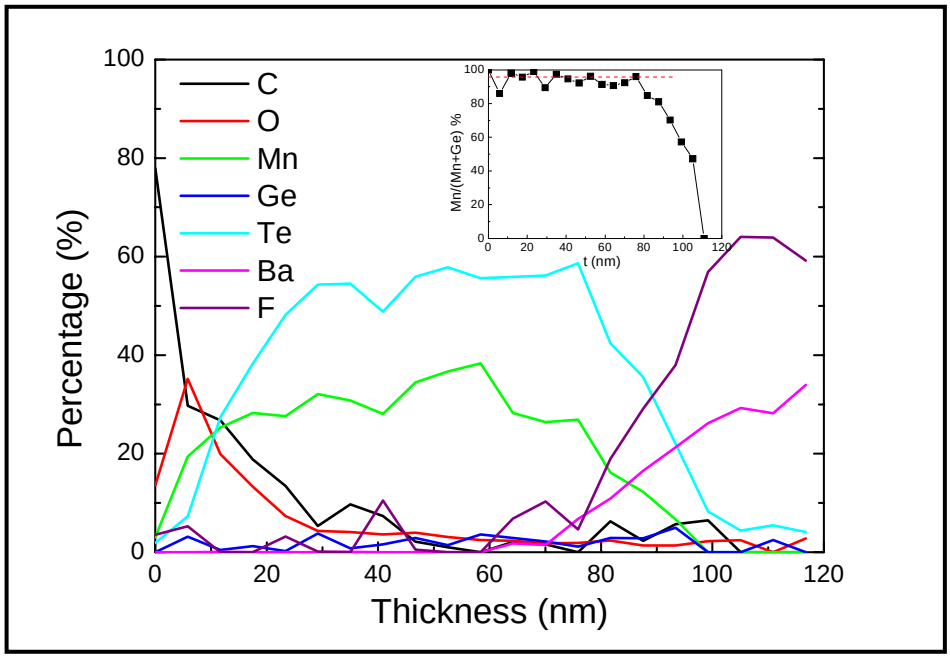

Figure 5-7 XPS depth profile of $Ge_{1-x}Mn_xTe$ film with T_{Mn}=625°C. The inset shows the relative Mn depth composition.

The Mn composition is varied by the change of Mn cell temperature so as to change Mn's BEP. Figure 5-8 shows the plot of the Mn composition versus Mn cell temperature. It can be observed that the Mn composition is linearly dependent on the temperature of the Mn cell.

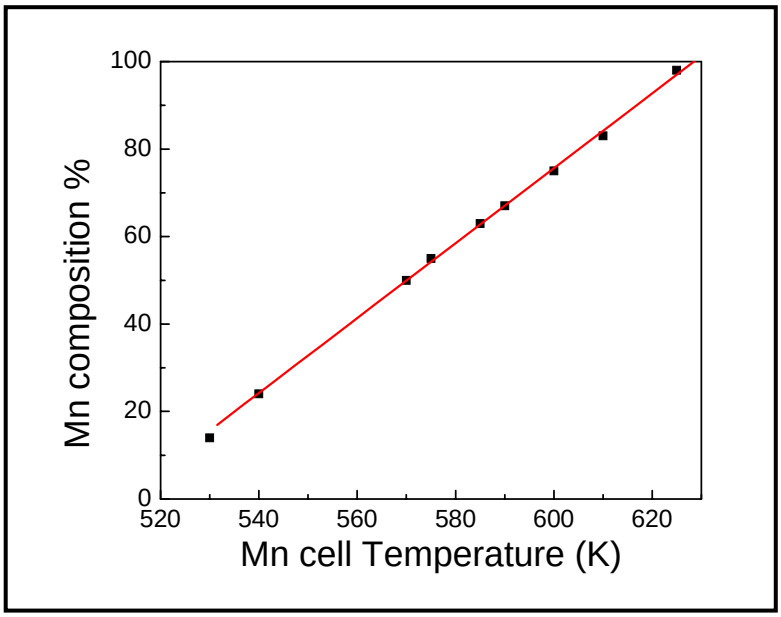

Figure 5-8 Mn composition vs. Mn cell temperature

5. 2 Structural Properties

5.2.1 XRD Crystalline Properties analysis

Figure 5-9 shows the XRD θ-2θ scan taken from a 100nm thick $Ge_{0.02}Mn_{0.98}Te$ film on a (111) BaF_2 substrates via a MnTe buffer grown at $T_S = 200°C$. The BaF_2 (111) and (222) peaks are located at 25.06° and 51.43°, respectively [11]. The peaks of $Ge_{0.02}Mn_{0.98}Te$ centered at 26.5° and 54° are indexed as (111) and (222) plane, respectively. Double peaks appeared around $Ge_{0.02}Mn_{0.98}Te$ (222) is caused by the wavelength difference from Cu K_α (0.1541nm) and K_β (0.1477nm) sources. No other phases are observed in the XRD measurement which indicates that film only crystallizes in cubic structure with (111) orientation preferred.

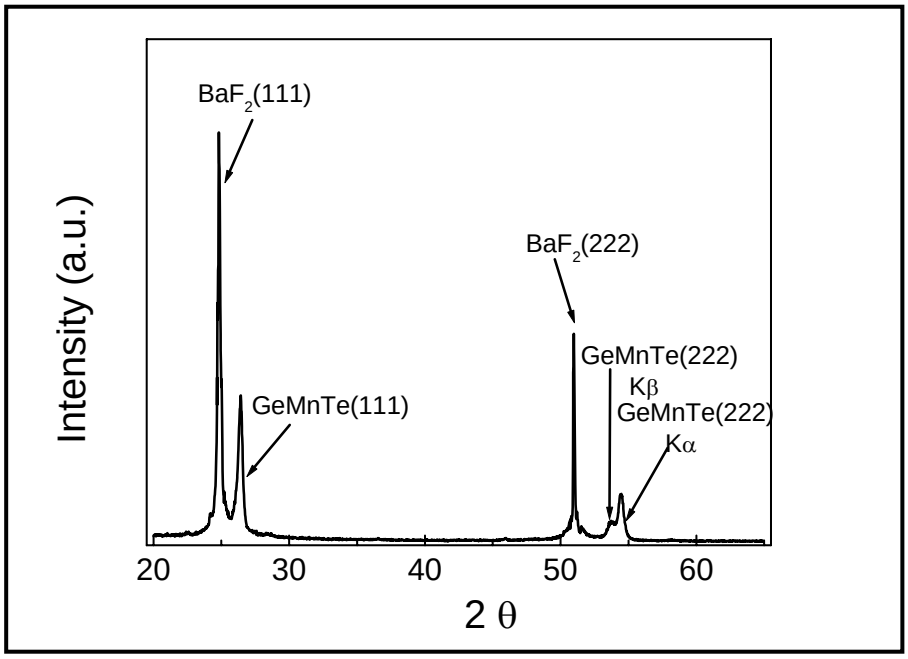

Figure 5-9 XRD θ-2θ scan of $Ge_{0.02}Mn_{0.98}Te$/MnTe film grown on BaF_2(111) at 200°C.

Figure 5-10 shows the XRD pattern of $Ge_{1-x}Mn_xTe$ (x = 0.55) sample. We observe that the signal of the $Ge_{1-x}Mn_xTe$ (111) peak tends to be overwhelmed by the

BaF_2 (111) peak occurring at 25.28°. For x < 0.55, the $Ge_{1-x}Mn_xTe$ (111) peak will shift towards a smaller angle and overlapping with the BaF_2 (111) peak. As such, it will be easier to determine the lattice constant by selecting the $Ge_{1-x}Mn_xTe$ (222) instead of $Ge_{1-x}Mn_xTe$ (111) peak.

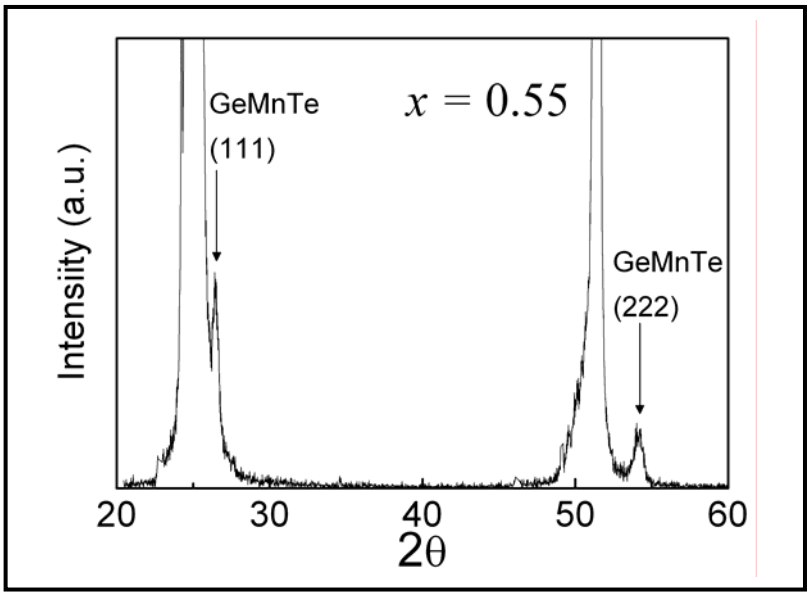

Figure 5-10 XRD patterns of $Ge_{1-x}Mn_xTe$ with x = 0.55.

Figure 5-11 shows the XRD patterns of the $Ge_{1-x}Mn_xTe$ (222) peak position with different Mn compositions. The spectra for different x are displayed vertically for clarity. The peak of GeMnTe (222) shifts towards the larger angle with the increase of the Mn composition. Assuming GeMnTe crystallizes in NaCl structure, the lattice constant can be derived from the XRD peak using equation:

$$2d\sin\theta = n\lambda. \quad (5\text{-}1)$$

For cubic structure, the spacing between the planes in the atomic lattice is given as

$$d = \frac{a}{\sqrt{h^2 + k^2 + l^2}}, \quad (5\text{-}2)$$

where a is the lattice constant, λ is the wavelength of the incident X-ray-beam ($\lambda_{K\alpha}$~

1.541Å in our XRD system), 2θ is the angle where peaks are detected and *h*, *k* and *l* are the Miller indices.

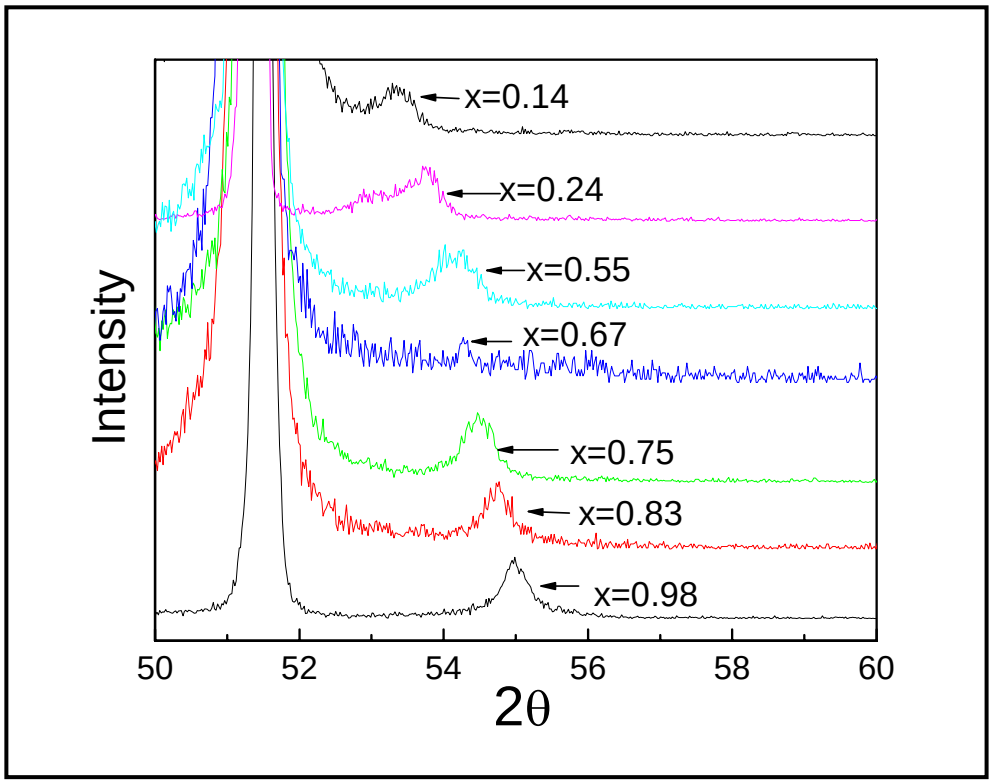

Figure 5-11 XRD patterns of $Ge_{1-x}Mn_xTe$/MnTe films on BaF_2(111) substrate with various Mn compositions.

Figure 5-12 shows the dependence of the lattice constant *a* on the Mn composition of the $Ge_{1-x}Mn_xTe$ films. A least-squared fit is obtained and is in good agreement with those reported in the literature. Extrapolation of the line to x=0 gives the lattice parameter value $a = 5.98$ Å for the rocksalt of GeTe, which is in good agreement with the lattice constant $a = 5.979$ Å from the literature [1].

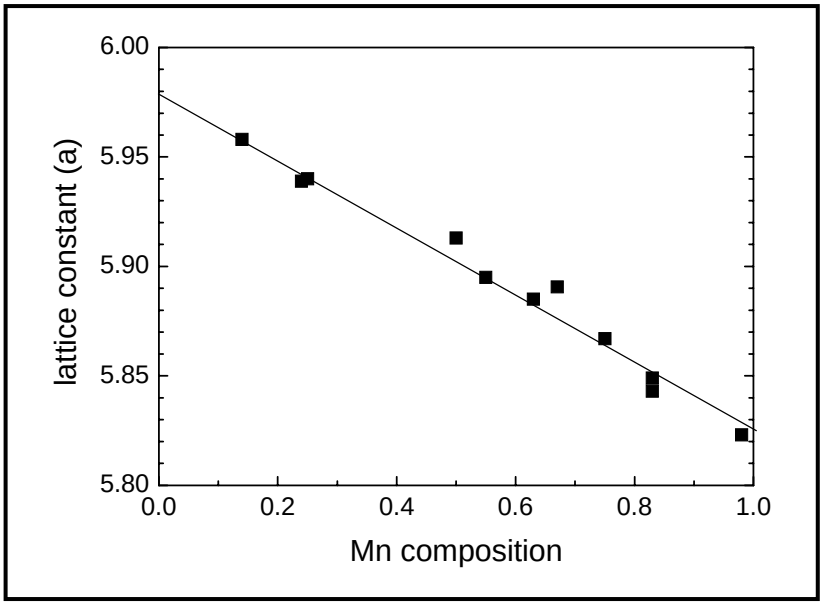

Figure 5-12 Mn composition dependence of lattice constant of $Ge_{1-x}Mn_xTe$ films. The solid line is the least-squared fit to the experiment data.

5.2.2 HRTEM analysis of the crystalline properties

The high-resolution TEM is utilized to investigate the crystal structure of the grown film. Figure 5-13 (a) and (b) show the high-resolution TEM images for $Ge_{1-x}Mn_xTe$ x=0.24 and x=0.55 samples, respectively. We observe a non-uniform spatial distribution of Mn contents exists in the x=0.24 sample as shown in Fig. 5-13 (a) which indicates that the film is non-homogeneous. Although the defects and dislocations deteriorate the crystalline quality, only rock-salt (NaCl) structure can be observed. In contrast, for x=0.55 sample, clusters or grains of different sizes (5 to 20 nm) are observed as shown in Fig. 5-13 (b). Among the clusters, two different kinds of structures; namely ZB (marked I) and NaCl (marked II) can be distinguished. Clear boundary was formed by the neighbouring grains with different crystal orientations. We note that similar distinct crystal structures have been observed in the TEM

imaging on the formation of PbTe quantum dots in a crystalline CdTe host matrix [11]. Due to high Mn composition, the films may subject to the phase segregation. As such, the ZB structure observed in Fig. 5-13 (b) is most likely arising from the formation of ZB MnTe. We note that XRD results shown in Fig. 5-9 do not reveal the ZB phase. This may be due to the XRD resolution limitation since clear diffraction peaks can only be observed when the sample possesses sufficient long-range crystallographic ordering.

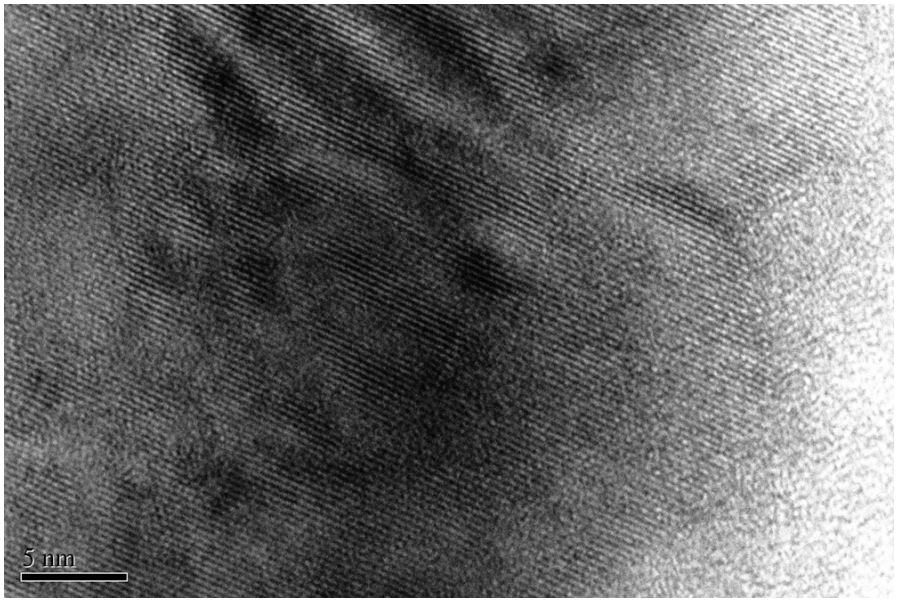

(a)

Figure 5-13 (a) High-resolution TEM images of $Ge_{1-x}Mn_xTe$ films for x=0.24.

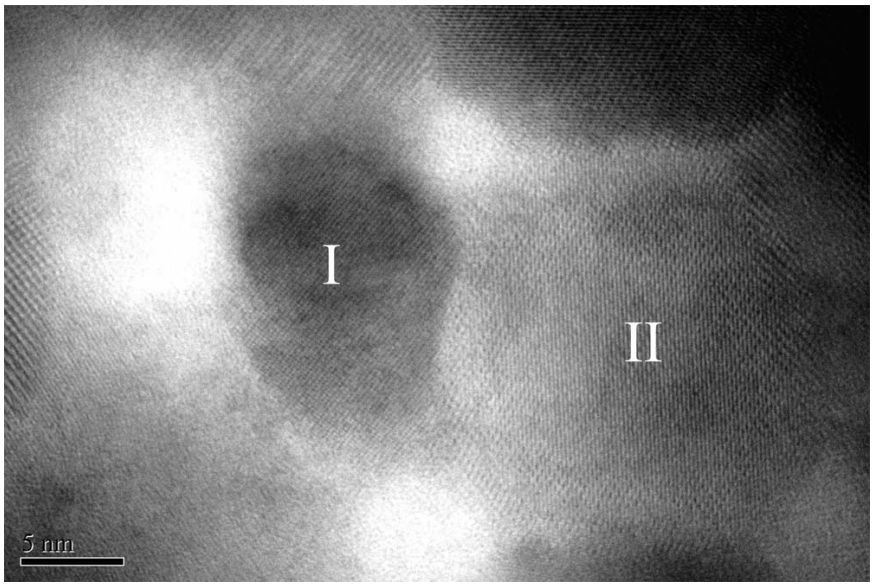

(b)

Figure 5-13 (b) High-resolution TEM images of $Ge_{1-x}Mn_xTe$ films for x=0.55.

Figure 5-14 shows the spot-selection of the energy dispersive X-ray spectroscopy (EDS) analysis for x=0.55 sample. We would like to emphasize that EDS offers only localized composition information and thus it does not accurately determine the elemental composition of the whole sample. Instead, we used the XPS measurement to determine the compound composition due to the good agreement between the XPS measurement and the result deduced from XRD peaks as shown in the previous section. However, EDS spot-analysis mode can be utilized to compare the bright and the dark area of Mn contents. It is found that the non-uniform Mn content is estimated to be 10.5% and 25.6% for spot 001 (brighter spot) and spot 002 (darker spot), respectively. The results indicate that the dark area has a higher Mn content as compared to the bright area. This strongly suggests the bright region consists mainly of GeTe matrix and thus it does not contribute significantly to the magnetic properties.

It is noted that the growth mode of the film is an island mode from the RHEED and AFM observation. The island configuration observed in TEM is randomly chosen.

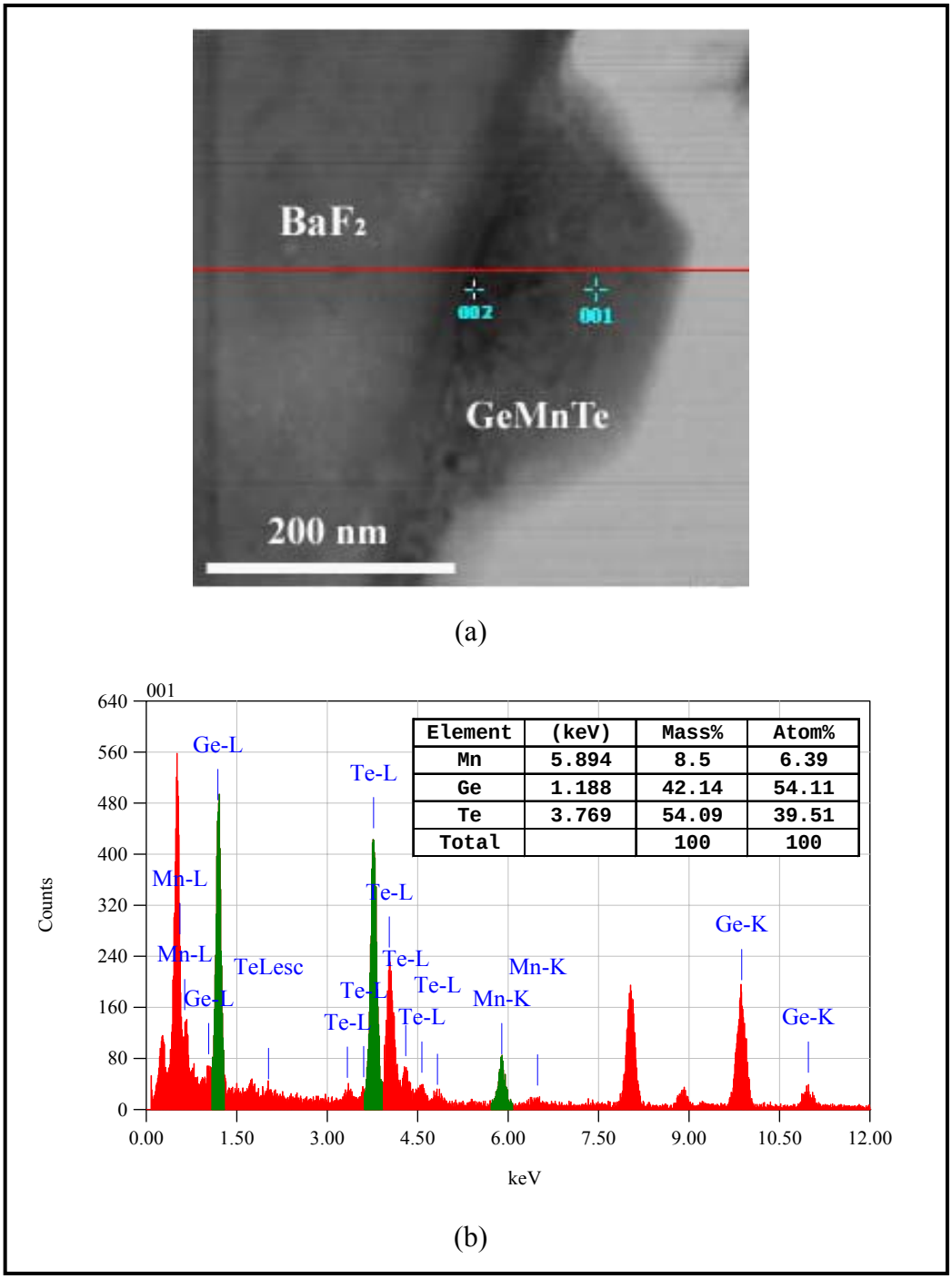

Figure 5-14 EDS spot-analysis mode of $Ge_{1-x}Mn_xTe$ x=0.55 film. (a) Cross-section image of the sample. (b) EDS analysis of spot 001, Mn content is estimated to be 10.5 %.

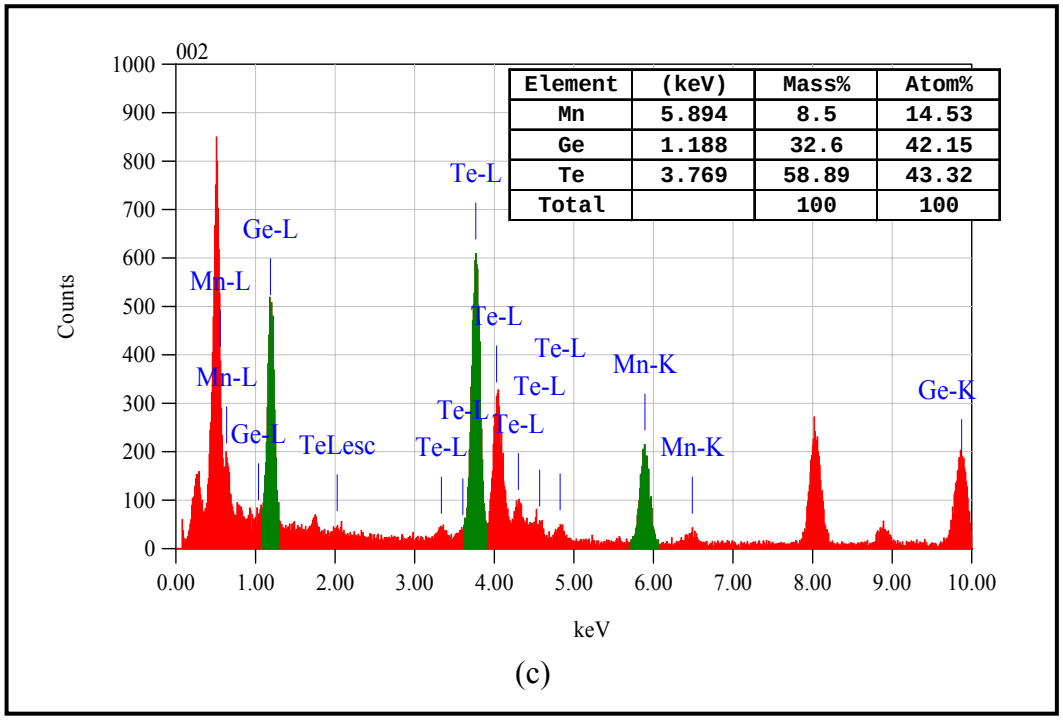

Figure 5-14 (c) EDS analysis of spot 002, Mn content is estimated to be 25.6%.

Figure 5-15 shows the line-analysis curves of the elemental intensities detected from the BaF_2 substrate to $Ge_{1-x}Mn_xTe$ film along the line for x=0.24 (a) and x=0.55 (b) samples. The contents of each layer are clearly observed and the cross-point of the elements symbolizes the starting or ending of their corresponding layers. The film thickness deduced by the EDS line-analysis is around 50nm and 120nm for x=0.24 and x=0.55 sample, respectively, which is in agreement with the result measured by XPS and prolifometry.

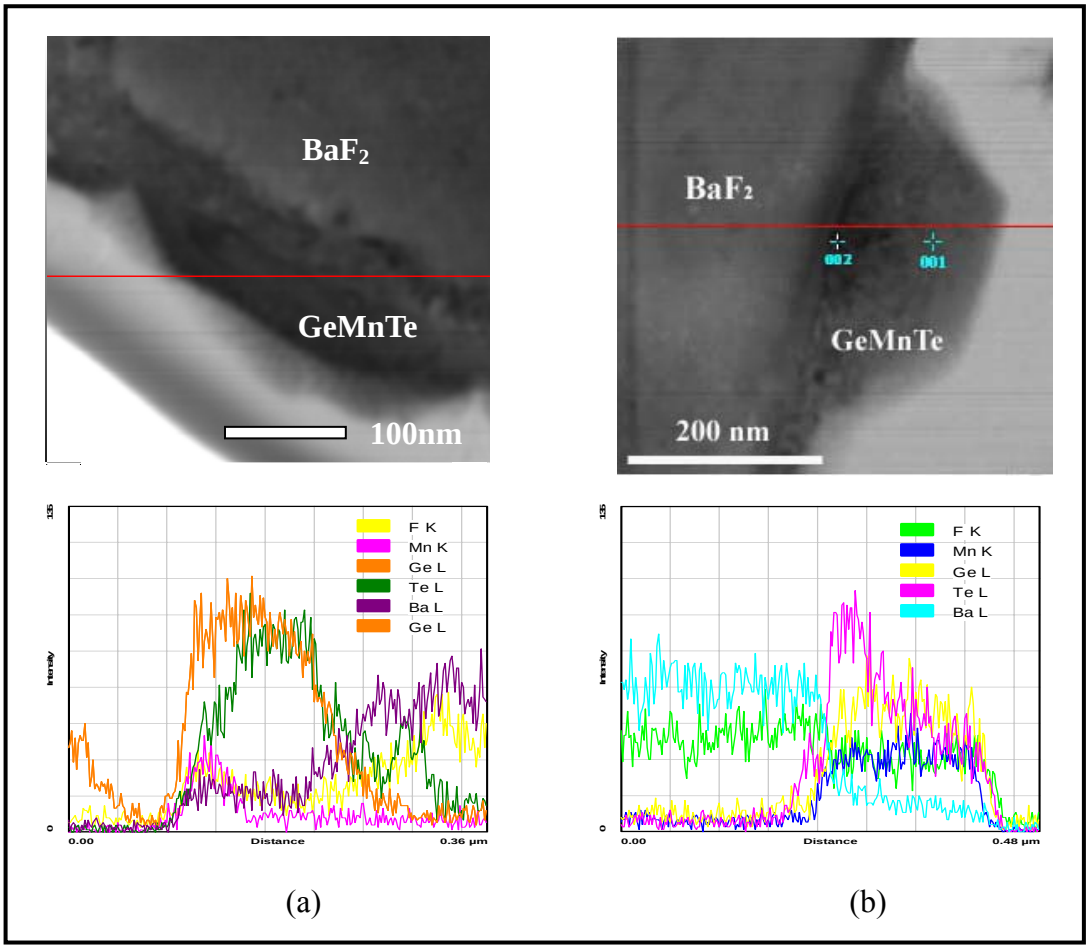

Figure 5-15 EDS line-analysis mode of $Ge_{1-x}Mn_xTe$ x=0.24 (a) and x=0.55 (b) films.

Figure 5-16 shows the scan of the mapping result of the element distribution in the $Ge_{1-x}Mn_xTe$ (x = 0.55) sample. We observe that the Ge, Mn and Te elements are mainly concentrated within the GeMnTe layer in which a small percentage of atoms are diffused outside the layer. For substrate elements, Ba is mainly concentrated in the BaF_2 layer, but large amount of F atoms are diffused into the $Ge_{1-x}Mn_xTe$ layer. This result is in good agreement with the EDS line-analysis as shown in Fig. 5-15 (b).

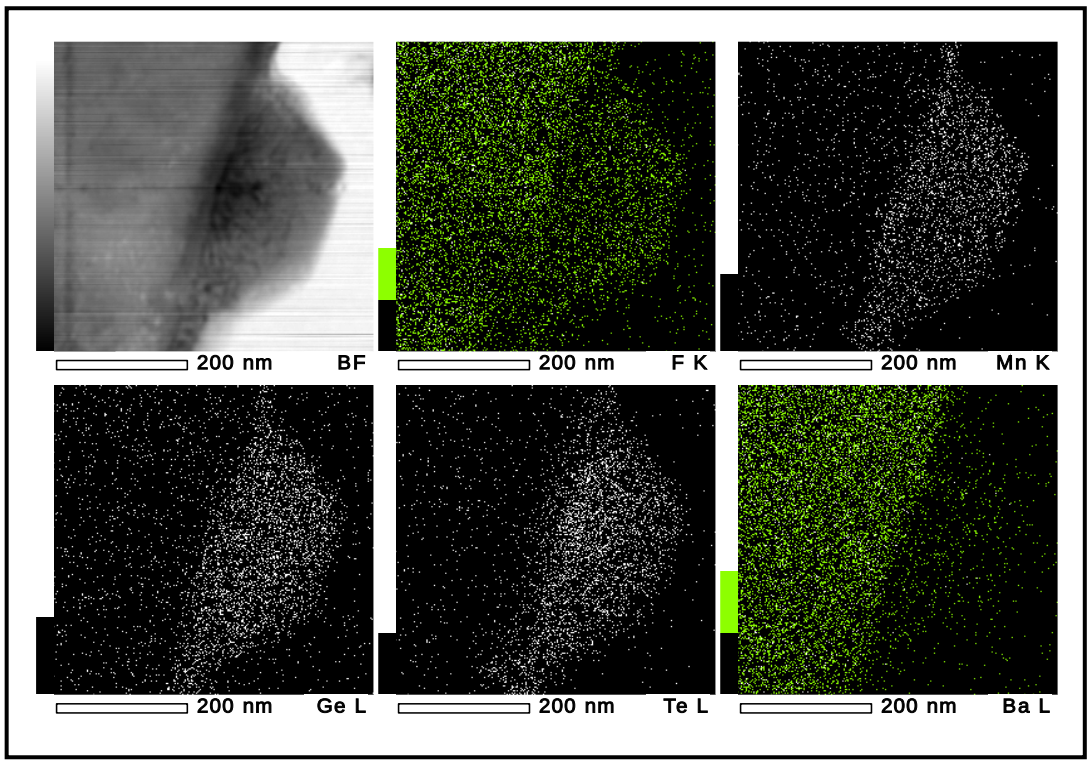

Figure 5-16 Elements mapping of $Ge_{1-x}Mn_xTe$ x = 0.55 sample.

The scan of the mapping result of the elements distribution in the $Ge_{1-x}Mn_xTe$ x=0.24 sample is shown in Fig. 5-17. Compared with the mapping result of x=0.55 sample, Mn element is much less within the $Ge_{1-x}Mn_xTe$ layer. The extra Ge at the surface was also observed which corresponds to the line-analysis as shown in the Fig. 5-15 (a). This may be due to the TEM sample preparation process since it occurs above the coating layer.

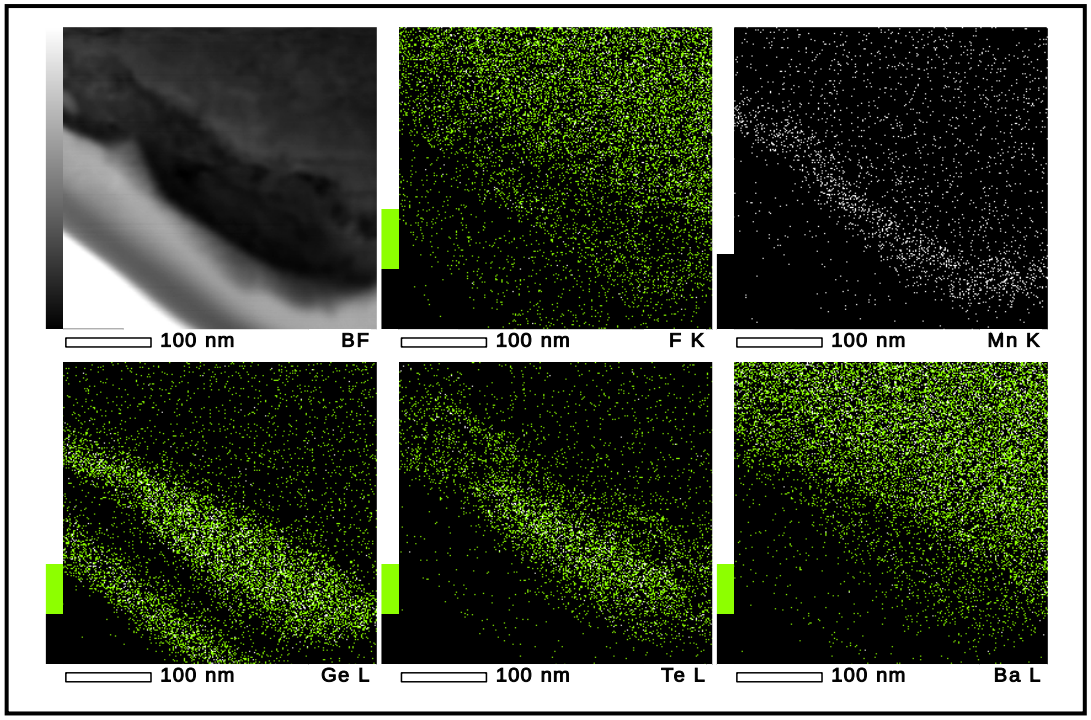

Figure 5-17 Elements mapping of $Ge_{1-x}Mn_xTe$ x = 0.24 sample.

5. 3 Optical Properties

The Spectrophotometer (UV-3101PC Spectrophotometer) is employed for the measurement of sample's reflection and transmission optical properties to obtain the absorption spectra and optical band-gap of a $Ge_{1-x}Mn_xTe$ sample.

The absorption coefficient is defined as the attenuation caused by energy absorption when the light passes through a medium. The mechanism of this absorption is a process in which the energy of a photon is taken when the electron is excited from the valence band to the conduction band. The absorption coefficient of direct bandgap semiconductor can be written as:

$$\alpha(h\nu) = A \times (h\nu - E_g)^{1/2}, \quad (5\text{-}3)$$

where A is a constant, $h\nu$ is the photon energy of the light and E_g is the band-gap of the semiconductor. However, for the indirect bandgap material, the above-mentioned

transition requires changes in both energy and momentum. A double or two-step process is required because the photon from the light cannot provide a change in momentum. Instead, a phonon is absorbed or emitted to conserve the momentum. The absorption coefficient of indirect bandgap semiconductor with phonon absorption and emission is:

$$\alpha_a(h\nu) = \frac{A(h\nu - E_g + E_p)^2}{e^{Ep/kT} - 1} \text{ and } \alpha_e(h\nu) = \frac{A(h\nu - E_g - E_p)^2}{1 - e^{-Ep/kT}} \quad (5\text{-}4)$$

respectively, where E_p is the phonon energy.

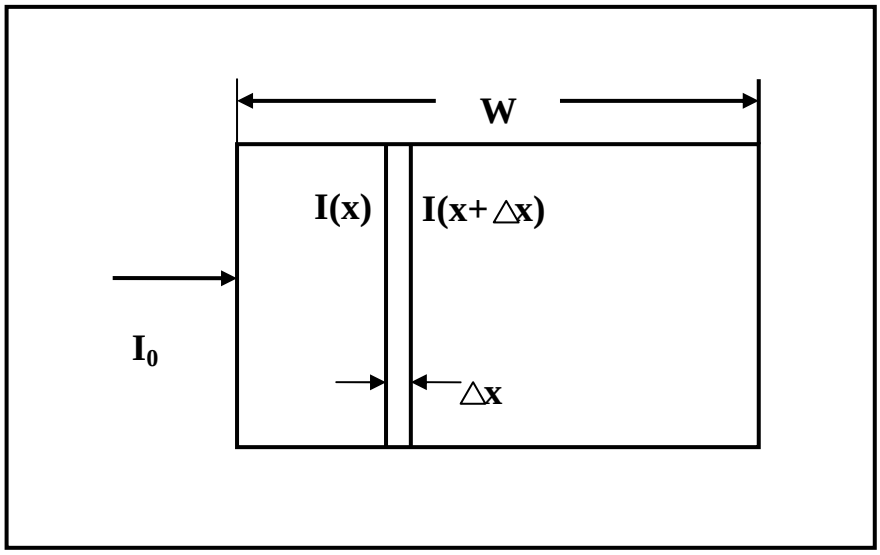

Figure 5-18 Illustration of an incident light on a slab of the semiconductor.

To obtain the absorption coefficient, let us consider an incident light on a slab of semiconductor shown in Fig 4-18. The absorption of light in a thin layer of thickness Δx at a distance x from the surface can be written as

$$\Delta I \propto -I_0 \Delta x, \quad (5\text{-}5)$$

$$\Delta I = -\alpha I_0 \Delta x, \quad (5\text{-}6)$$

therefore, $I(x) = I_0 e^{-\alpha x}$ (5-7)

where α is the absorption coefficient, I_0 is the incident light intensity. To obtain α value, the ratio of the transmitted to incident power I_T/I_o is required.

If we consider a more complex situation when the sample is a system with multiple internal reflections (We assume that the reflectance R is constant throughout the whole film) as shown in Fig. 5-19, the transmission coefficient T (the ratio of transmitted to incident power I_T/Io) is given as

$$I = I_0(1-R)^2 e^{-\alpha x}(1 + R^2 e^{-2\alpha x} + R^4 e^{-4\alpha x} + \cdots\cdots)$$
$$= \frac{I_0(1-R)^2 e^{-\alpha x}}{1 - R^2 e^{-2\alpha x}} \qquad (5\text{-}8)$$

The transmission coefficient of the film is then expressed as

$$T = \frac{I_T}{I_0} = \frac{(1-R)^2 e^{-\alpha} x}{1 - R^2 e^{-2\alpha x}}, \qquad (5\text{-}9)$$

For $\alpha x >> 1$, T can be simplified as

$$T \approx (1-R)^2 e^{-\alpha x} \qquad (5\text{-}10)$$

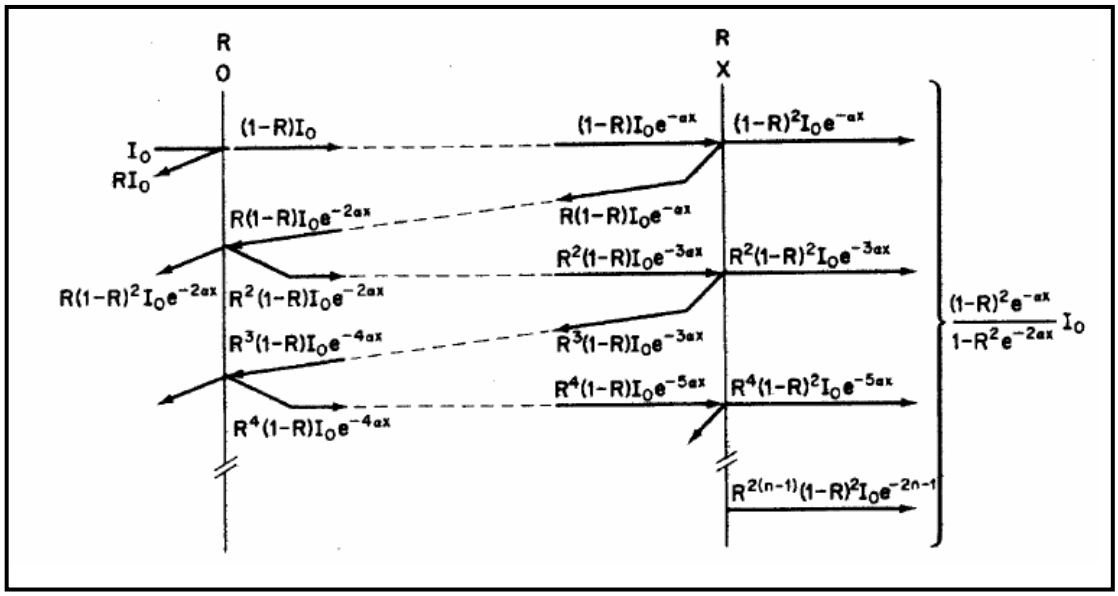

Figure 5-19 Accounting energy flow in a system allowing multiple internal reflections.

Since BaF_2 is a wide bandgap material with $E_g = 9.1\,\text{eV}$ [5], there will be no electron transition process from the valence band to the conduction band when the light with photon energy in the range of 0.58eV to 6.2eV ($300nm < \lambda < 3200nm$) is incident on it. Therefore, we can separate the total transmission coefficient T as

$$T = T_f \times T_s \tag{5-11}$$

where T_f is the transmission coefficient of the film and Ts is the transmission coefficient of the BaF_2 substrate. The formula used to calculate the absorption coefficient of the film is given in (4-10) as

$$T_f = (1-R)^2 e^{-\alpha x} \tag{5-10a}$$

By substituting (4-10a) into eq.(4-11), $\frac{T}{T_s} = T_f = (1-R)^2 e^{-\alpha x}$ (5-12)

Therefore, $\alpha = -\frac{1}{x}\ln\frac{T}{T_S \times (1-R)^2} = \frac{1}{x}\ln\frac{T_S \times (1-R)^2}{T}$ (5-13)

Figure 5-20 (a), (b) and (c) shows the spectra of the total transmission coefficient (T), the substrate transmission coefficient (Ts) and reflection coerfficient (R), respectively for the $Ge_{1-x}Mn_xTe$ (x=0.98) sample. The total transmission coefficient T drops from around 30% to near zero when the photon energy increases to greater than 1.5 eV. Instead, the substrate transmission coefficient Ts does not show abrupt droping to zero, which proves the substrate is a wide bandgap semiconductor. Moreover, two peaks in the reflection coerfficient (R) of the film are observed which may be caused by the $Ge_{1-x}Mn_xTe$ film and the buffer layer.

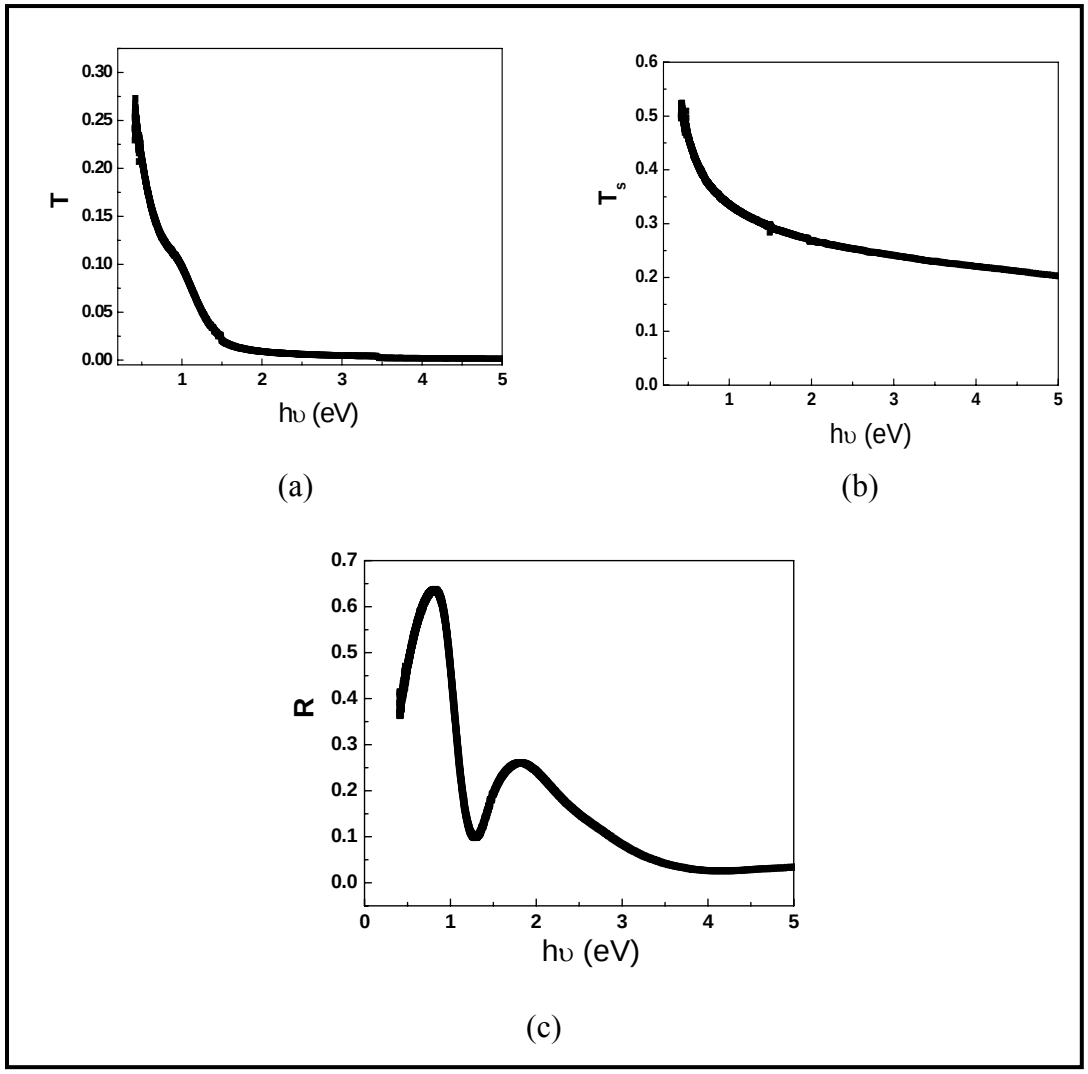

Figure 5-20 The spectra of the total transmission coefficient T of $Ge_{0.02}Mn_{0.98}Te$ (a), the substrate transmission coefficient Ts (b) and reflection coerfficient R (c).

The deduced absorption coefficient spectrum using formula (5-13) is shown in Fig. 5-21 (a) assuming the film is homogeneous. A minimum value of $3\times10^3\,cm^{-1}$ is obtained at 0.785 eV. It is well known that the GeTe is a p-type degenerate semiconductor with E_g ~ 0.1 to 0.2 eV but usually a direct optical absorption edge is observed at 0.7-1.0 eV, which is due to Burstein-Moss shift [12]. Besides, MnTe is also a p-type direct bandgap semiconductor with E_g ~1.3eV and 3.1eV for NiAs [13] and ZB structure [14], respectively. Since both GeTe and MnTe are direct bandgap semiconductors, the compound $Ge_{1-x}Mn_xTe$ is a direct bandgap material and E_g is

proportional to the square of the absorption coefficient α^2 when the incident photon energy $h\nu$ is higher than the E_g. The absorption curve of $Ge_{0.02}Mn_{0.98}Te$ is plotted in the form of $(\alpha h\upsilon)^2$ versus $(h\upsilon)$ according to Tauc relation [15] as shown in Fig. 5-21 (b). The E_g value obtained for $Ge_{1-x}Mn_xTe$ (x=0.98) sample is E_g ~1.02 eV.

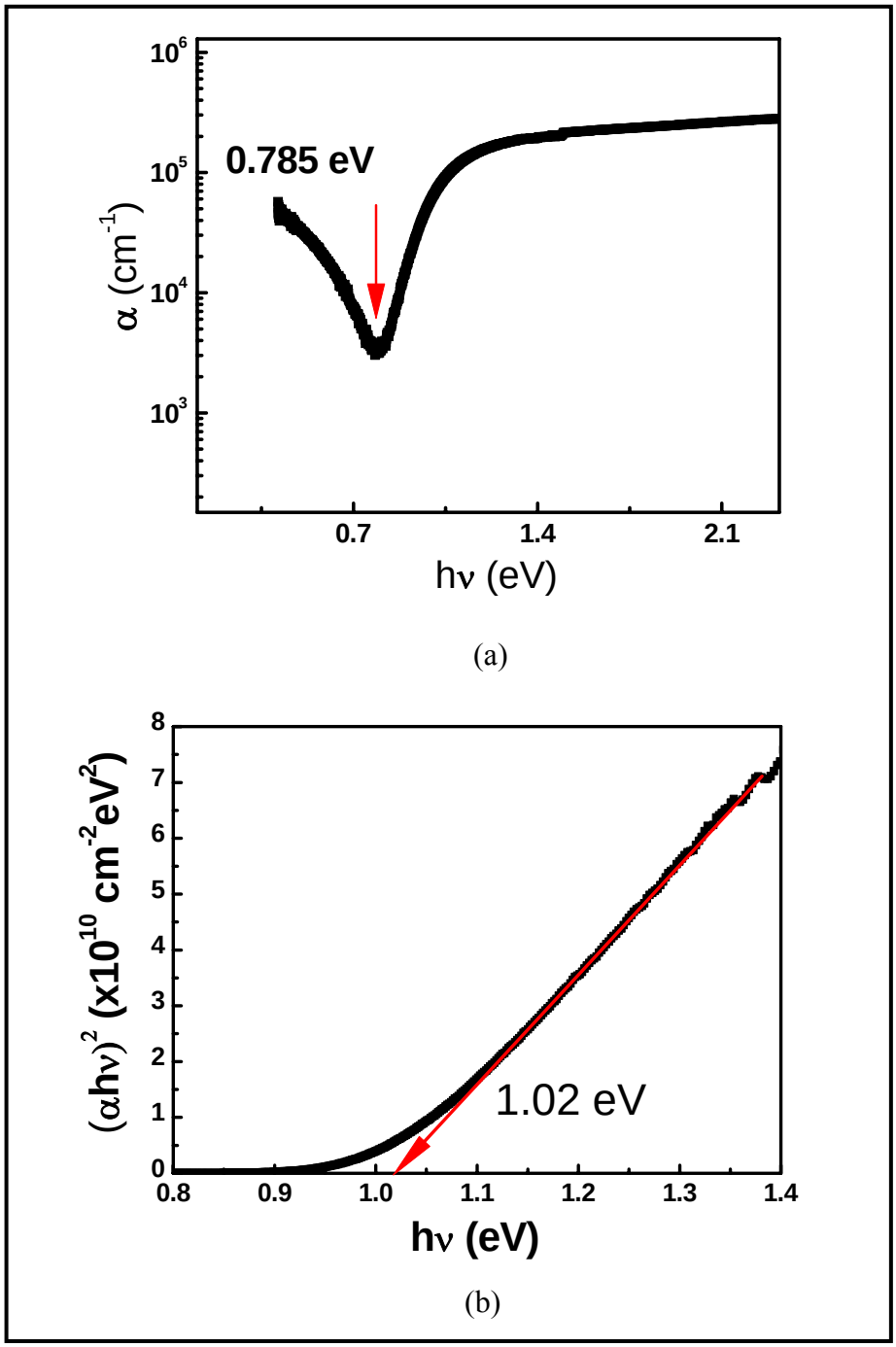

Figure 5-21 The absorption coefficient spectrum (a) and the deduced bandgap spectrum (b) of $Ge_{1-x}Mn_xTe$ (x=0.98) film.

The same method is used for bandgap E_g deduction of $Ge_{1-x}Mn_xTe$ samples with $0.14<x<0.98$ Mn composition. Figure 5-22 (a) specifically shows the $(\alpha h\upsilon)^2$ versus $(h\upsilon)$ plotting of x=0.14, 0.24, 0.55, 0.75 and 0.98 samples with film thickness of 50nm, 120nm, 110nm, 90nm and 100nm, respectively. The deduced band-gap for these five samples are 0.87, 0.92, 0.96, 1.0 and 1.02eV, respectively. The dependence of the band-gap value on the Mn composition is shown in Figure 5-22 (b). The results show that the band-gap of magnetic semiconductor $Ge_{1-x}Mn_xTe$ with $0.14<x<0.98$ in a manner qualitatively similar to the nonmagnetic semiconductor counterpart. Our measurement values all fall in the range of 0.7 eV to 1.3 eV. The straight line is the linear fitting to the experimental data.

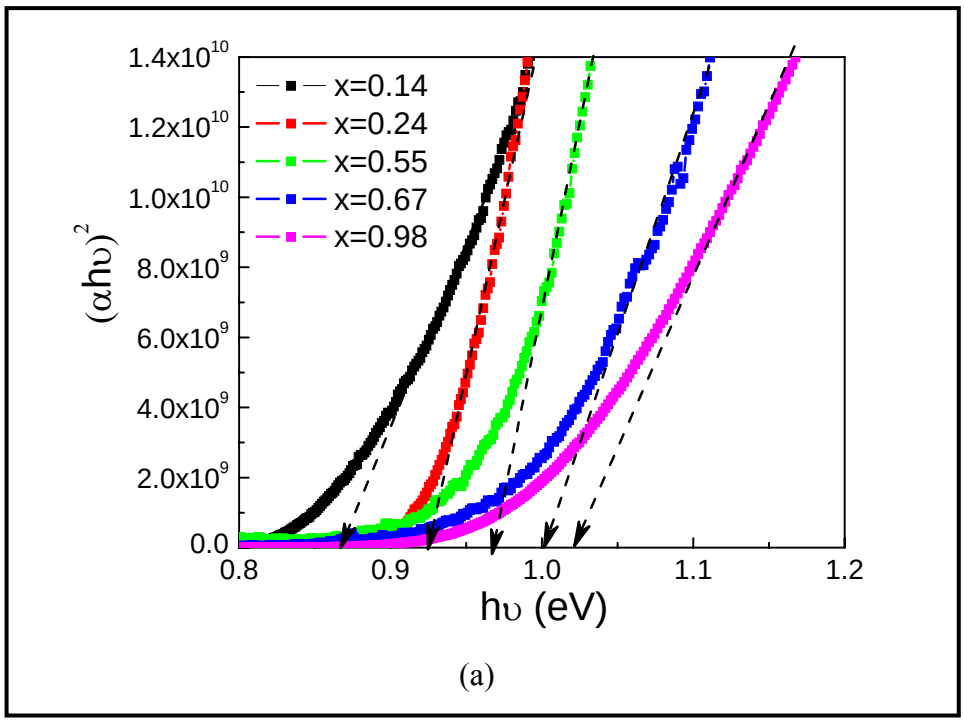

Figure 5-22 (a) the $(\alpha h\upsilon)^2$ versus the $(h\upsilon)$ plotting of $Ge_{1-x}Mn_xTe$ samples with x=0.14, 0.24, 0.55, 0.67 and 0.98.

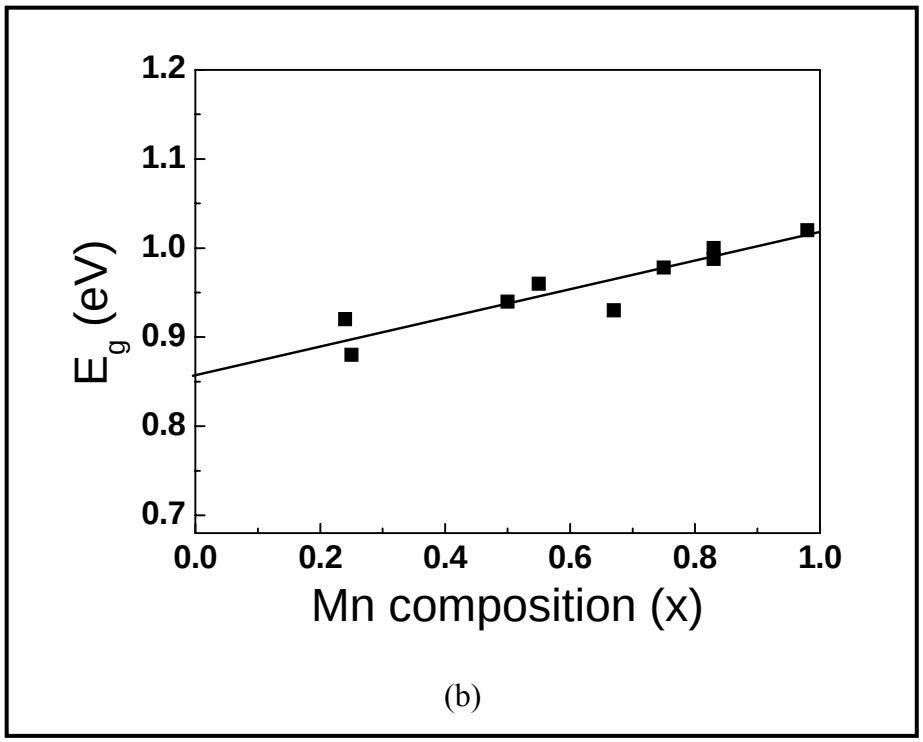

(b)

Figure 5-22 (b) Mn composition dependence of bandgap Eg of $Ge_{1-x}Mn_xTe$ films. The straight line is the linear fitting to the experiment values.

Two competing mechanisms; namely, Burstein-Moss shift and band-gap narrowing will cause the bandgap shift when the doping concentrations are high. The Burstein-Moss shift is also called band filling or phase-space filling, so that the conduction band becomes significantly filled at high doping concentrations due to the finite density of states. Hence, absorption transition edges will shift to a value higher than the undoped semiconductor bandgap. Quantitatively, the Burstein-Moss shift can be calculated from the filling of the conduction or valence band in n-type and p-type semiconductors, respectively. The shift in the band-gap is given by [16]

$$\Delta E = \frac{\hbar^2}{2m^*}(3\pi^2 n)^{2/3} \qquad (5\text{-}14)$$

where n is the free carrier concentration and m^* is the effective carrier mass. Since it is inversely proportional to the effective mass, the effect of Burstein-Moss shift is

more effective in n-type material than in p-type material. On the other hand, the main reason of band-gap narrowing is many-body effects of free carriers through long-range Coulomb potential or spins interactions, which lower the electron energies as compared to a non-interacting carrier system [17]. In our high *p*-type $Ge_{1-x}Mn_xTe$, the band-gap shift is likely to be due to the combined effect of band gap narrowing effect and the Burstein-Moss shift.

5. 4 Summary

In summary, the growth condition of $Ge_{1-x}Mn_xTe$ in the MBE system has been discussed in this chapter. A few monolayers of cubic MnTe are grown as a buffer to compensate the substrate surface defects. The optimum growth condition with flux ratio of Te/Ge~1.5 to 2, Te/Mn~13 to 70 and the growth temperature ~200^{o}C are chosen for the growth.

The composition of the $Ge_{1-x}Mn_xTe$ film, which is in the range of $0.14<x<0.98$, is determined from XPS measurement. XRD result shows that the films crystallize in rocksalt structure and the lattice constant deduced from the peak has a linear relationship with the Mn composition. The HRTEM results show that the non-uniformity exists in the film. The samples are not homogeneous and may contain clusters or grains with different sizes and compositions. Moreover, ZB and NaCl structures are distinguished in the high Mn composition sample, which may be subject to the phase segregation. The direct band-gap (E_g) values of the $Ge_{1-x}Mn_xTe$ films are deduced from the optical absorption measurement. All the E_g values all fall in the

range of 0.7 eV to 1.3 eV, which is the bandgap of rocksalt GeTe and NiAs MnTe, respectively.

References:

[1] Y. Ishihara, Y. Yoshita and I. Nakada, "Specific Heat of Germanium Monotelluride" J. Phys. Soc. Jap., **55**, 1948 (1986).

[2] W. Szuzkiewicz, B. Hennion, B. Witkowska, E. Lusakowska, and A. Mycielski, "Neutron Scattering study of structural and magnetic properties of hexagonal MnTe", Phys. Stat. Sol. (c) **2**, 1141 (2005).

[3] S. M. Durbin, J. Han, Sungki O, M. Kobayashi, D. R. Menke, R. L. Gunshor, Q. Fu, N. Pelekanos, A. V. Nurmikko, D. Li, J. Gonsalves, and N. Otsuka, "Zinc-blende MnTe: Epilayers and quatumn well structure" Appl. Phys. Lett., **55**, 2067 (1989).

[4] W. D. Johnston and D. E. Sestrich, "The MnTe-GeTe Phase Diagram"**,** J..Vnorg. Nucl. Chem., **19**, 229 (1961).

[5] http://www.almazoptics.com/BaF2.htm

[6] O. Sh. Gogishvili, A. N. Degtyarev, G. G. Kononov, I. P. Lavrienko, S. P. Ladykin, Inorg. Mater., **24,** 1108 (1988).

[7] A. J. Nadolny, J. Sadowski, B. Taliashvili, M. Arciszewska, W. Dobrowolski, V. Domukhovski, E. Łusakowska, A. Mycielski, V. Osinniy, T. Story, K. Świątek, R.R. Gałązka and R. Diduszko, "Carrier induced ferromagnetism in epitaxial $Sn_{1-x}Mn_xTe$ layers" J. Magn. Magn. Mater., **248,** 134 (2002).

[8] N. Frank, A. Voiticek, H. Clemens, A. Holzinger and G. Bauer, "High vacuum molecular beam epitaxy for the growth of IV-VI compounds" Journal of crystal growth, **126,** 293 (1993).

[9] Y. Fukumaa, T. Taya, S. Miyawaki, T. Irisa, H. Asada, and T. Koyanagi, "Growth and magnetic properties of IV-VI diluted magnetic semiconductor $Ge_{1-x}Cr_xTe$" J. Appl. Phys., **99**, 08D508 (2006).

[10] K. Ando, K. Takahashi and T. Okuda, "Zinc-blende MnTe: magnetic properties", J. Mag. Mag. Mat., **104-107** 993-994 (1992).

[11] W. Heiss, H. Groiss, E. Kaufmann, G. Hesser, M. Böberl, G. Springholz, and F. Schäffler R. Leitsmann and F. Bechstedt, K. Koike, H. Harada, and M. Yano, "Quantum dots with coherent interfaces between rocksalt-PbTe and zincblende-CdTe", J. Appl. Phys., **101**, 081723 (2007).

[12] R. Tsu, W. E. Howard and L. Esaki, "Optical and Electrical Properties and Band structure of GeTe and SnTe" Phys. Rev., **172,** 779 (1968).

[13] J. W. Allen, G. Lucovsky, and J. C. Mikkelsen, "Optical Properties and Electrical Strucature of Crossroads Material MnTe", Solid State Commun. , **24**, 367 (1977).

[14] A. Goswami, A.B. Mandale, "Electrical Properties of Manganous Telluride films" Jpn. J. Appl. Phys., **17,** 473 (1978).

[15] J. Tauc, Amorphous and Liquid Semiconductor, Plenum Press, New York (1974).

[16] Moss TS. "The Interpretation of the Properties of Indium Antimonide", Proc Phys Soc (London) B, **67**, 775, (1954).

[17] R. A. Abram, G. N. Childs, and P. A. Saunderson, "Band-gap Narrowing Due To Many-body Effects In Silicon and Gallium-Arsenide" J. Phys. C, **17**, 6105 (1984).

CHAPTER 6 RESULTS AND DISCUSSION: MAGNETIC AND TRANSPORT PROPERTIES OF $Ge_{1-x}Mn_xTe$ FILMS

In this chapter, the magnetic and transport properties of $Ge_{1-x}Mn_xTe$ thin films are extensively investigated. The magnetization measurement is carried out in a SQUID system while the transport properties characterization is performed with a Hall system and a cryostat electromagnet system. Since the $Ge_{1-x}Mn_xTe$ thin-films with $0.14<x<0.98$ have the similar magnetic and transport behaviours, the report mainly focused on 4 characteristic samples with Mn composition of x=0.14, 0.24, 0.55 and 0.98.

6.1 Magnetic Properties of $Ge_{1-x}Mn_xTe$ thin films

6.1.1 Field dependent magnetic properties of $Ge_{1-x}Mn_xTe$ thin films

Figure 6-1 shows the field-dependent magnetization (M-H) curves of $Ge_{1-x}Mn_xTe$ thin films with Mn composition x=0.14 (a), x=0.24 (b), x=0.55 (c), and x=0.98 (d) under an in-plane applied-field up to 2 Tesla at 5K. The hysteresis curves of x=0.14 (a), x=0.24 (b), x=0.55 (c), and x=0.98 (d) clearly demonstrate ferromagnetism with a coercive field H_C of 475 Oe, 530 Oe, 370 Oe and 445 Oe, respectively and the corresponding spontaneous magnetization Ms of 16.5 emu/cc, 30 emu/cc, 12 emu/cc, and 18 emu/cc, respectively.

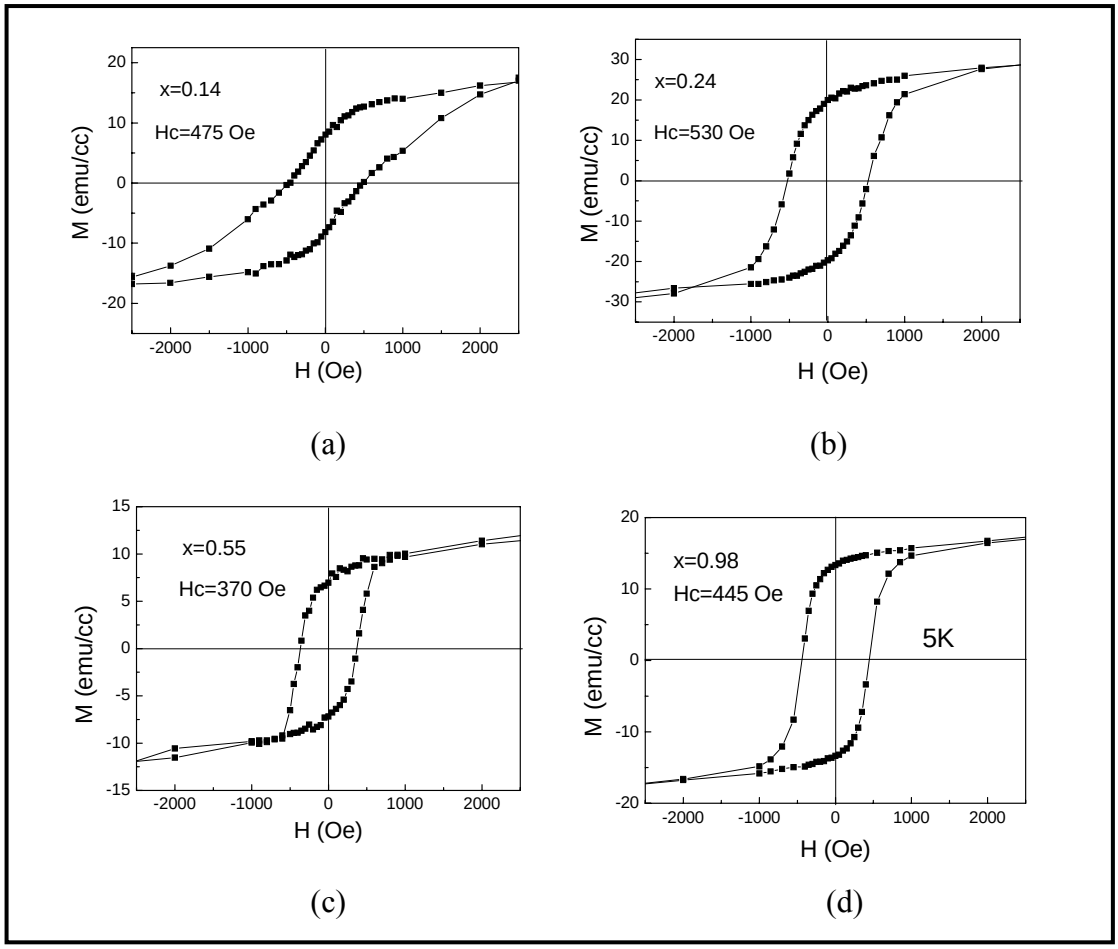

Figure 6-1 M-H curves of $Ge_xMn_{1-x}Te$ film with (a) x = 0.14, (b) x = 0.24, (c) x = 0.55 and (d) x=0.98.

The effective magnetic moment per Mn ion μ_{eff} is defined as

$$\mu_{eff} = \frac{M}{N_{Mn}}, \tag{6-1}$$

where M is the total magnetic moment (emu) and N_{Mn} is the number of Mn atoms. We rewrite eq. (6-1) as

$$\mu_{eff} = \frac{M/V}{N_{Mn}/V} = \frac{M_s}{N_{Mn}/V} \tag{6-2}$$

where V is the total volume. For the cubic lattice, $N_{Mn}/V = \frac{4x}{a^3}$, (6-3)

where x is the Mn composition and a is the lattice constant, μ_{eff} is simplified as

$$\mu_{eff} = \frac{M_s}{4x/a^3}. \qquad (6\text{-}4)$$

Since the lattice constant a for x=0.14, 0.24, 0.55 and 0.98 samples are 0.5958nm, 0.5939 nm, 0.5895 nm and 0.5823 nm respectively, the deduced effective magnetic moment per Mn ion at 5K for x=0.14, 0.24, 0.55 and 0.98 samples are 0.68 μ_B, 0.72 μ_B, 0.13 μ_B and 0.11 μ_B, respectively.

Figure 6-2 (a) shows the field-dependent magnetization (M-H) measurement for $Ge_{0.02}Mn_{0.98}Te$ sample at different temperatures. Clear hysteresis curves are obtained at various temperatures below 100K. No hysteresis loop is observed when T>100K, indicating FM ordering ceases to exist at T =100K. Figure 6-2 (b) shows coercive field H_C and remnant magnetization M_r of $Ge_{0.02}Mn_{0.98}Te$ sample at different temperatures. It is observed that both H_C and M_r decreases with the increase of the temperature and drops to near zero at approximately 80K.

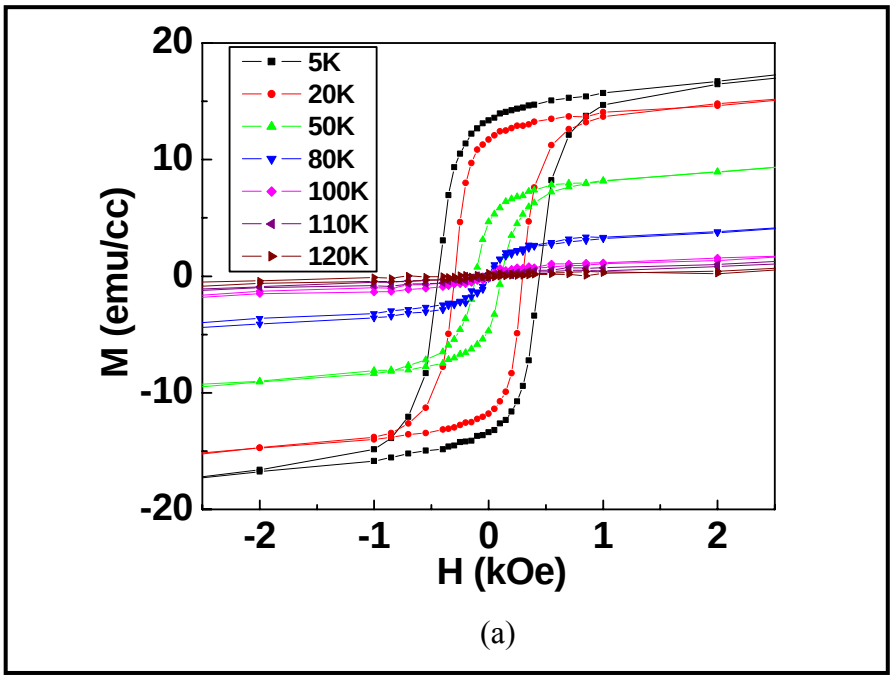

Figure 6-2 (a) Field-dependent magnetization (M-H) measurement for $Ge_{0.02}Mn_{0.98}Te$ films at different temperatures

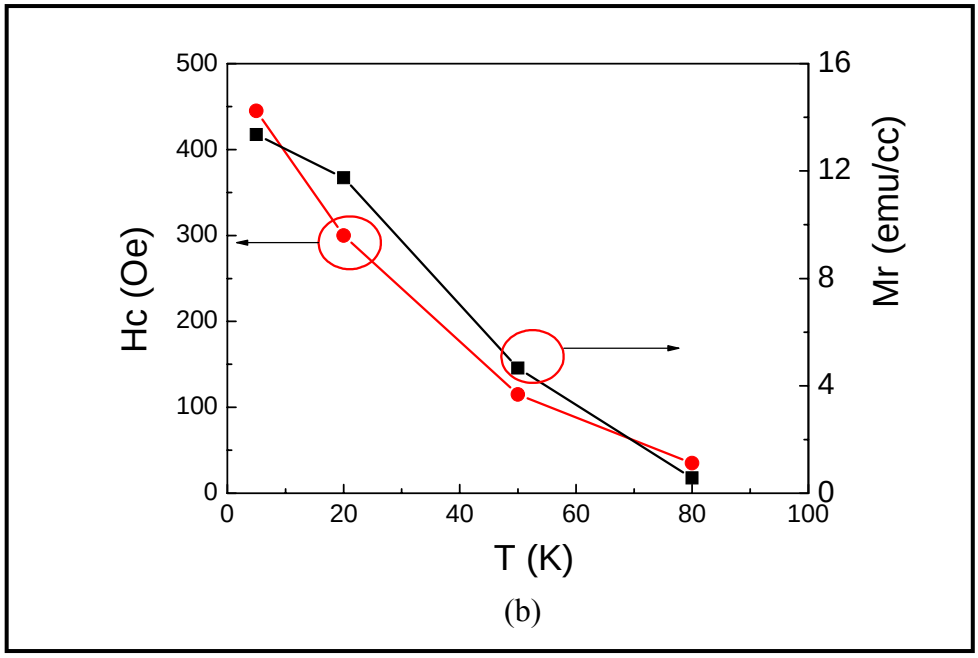

Figure 6-2 (b) Temperature-dependent H_C (round) and M_r (square) of $Ge_{0.02}Mn_{0.98}Te$ sample.

6.1.2 Temperature dependent magnetization of $Ge_{1-x}Mn_xTe$ thin films

Field-cooling (FC) curve is obtained in a manner that the sample is cooled with the presence of a magnetic field of 100 Oe from room temperature to 5 K and then the magnetic moment is measured while warming up the sample. Figure 6-3 shows the FC curves of $Ge_{1-x}Mn_xTe$ films with different Mn compositions x=0.14 (a), x=0.24 (b), x=0.55 (c), and x=0.98 (d). We note that no secondary magnetic phases such as Mn_5Ge_3 [1-3] and $Mn_{11}Ge_8$ [4] are detected, because these two phases are highly insulating with Curie temperature T_C>270K. The obtained temperature when the magnetization decreases to zero for x=0.14 (a) x=0.24 (b), x=0.55 (c), and x=0.98 (d) at 90K, 120 K, 190 K and 130K, respectively. The shape of the FC curve is more of concave type for x = 0.14 and 0.24 as compare to x = 0.55 and 0.98 sample, which

deviates from the Weiss mean-field theory. Current theories suggest that the shape of M-T curves is controlled by disorder in the sample and any shape such as concave, linear or convex is possible [5-7]. We attempt to fit $1/\chi$ –T curve to the Curie-Weiss law from the M-T curve according to the relationship $\chi = M/H$. The intercept on the temperature axis at the positive side gives a paramagnetic (PM) transition temperature θ_p of 100K, 135 K, 180 K and 120 K for x=0.14, 0.24, x=0.55 and x=0.98, respectively.

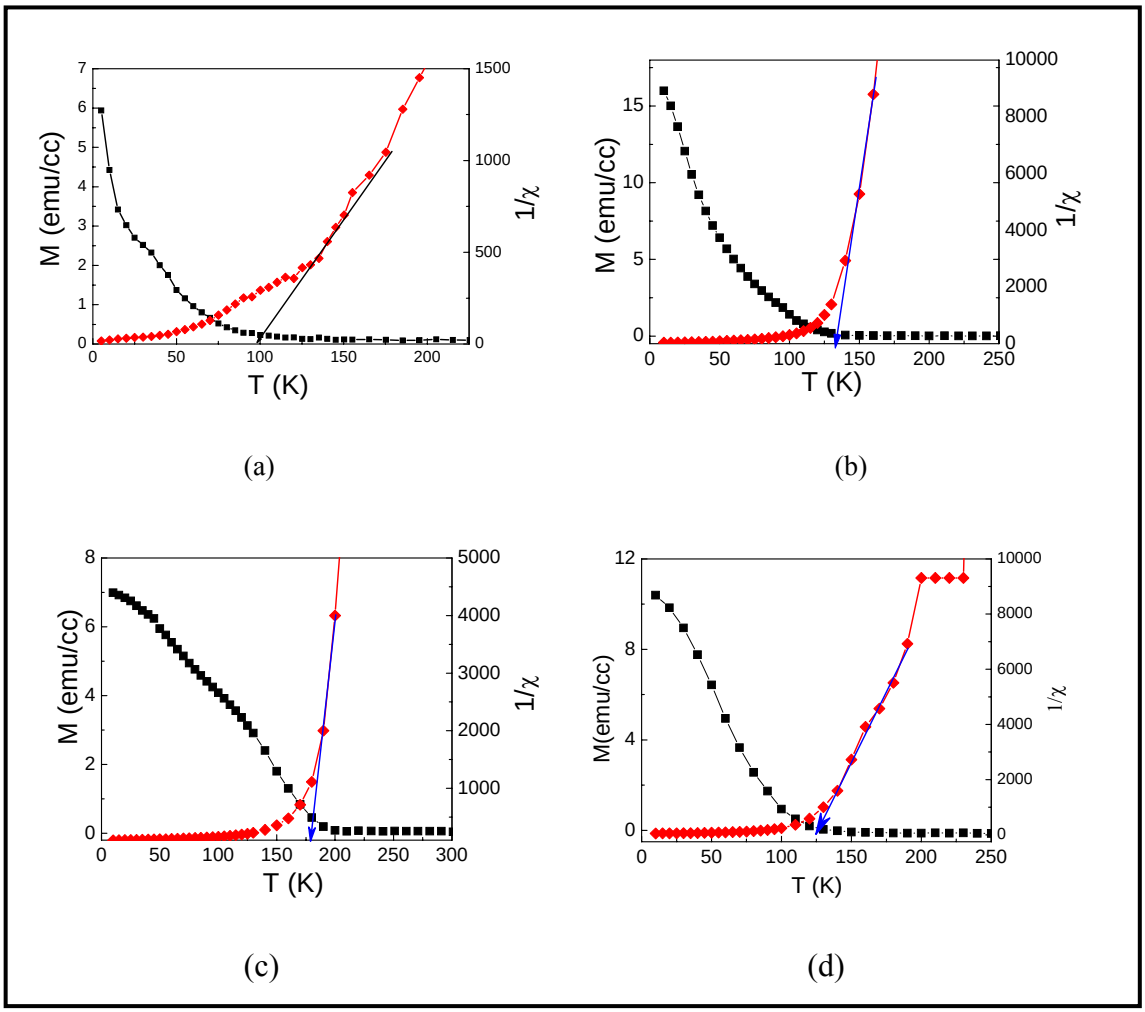

Figure 6-3 M-T curves (FC) for $Ge_xMn_{1-x}Te$ film (a) x = 0.14, (b) x=0.24, (c) x = 0.55 and (d) x=0.98 with 100 Oe field. The solid diamond shows the inverse magnetic susceptibility and the Curie-Weiss fit is depicted by the solid straight line.

Figure 6-4 presents the zero-field cooling (ZFC) and FC curves of $Ge_{1-x}Mn_xTe$ thin films with Mn composition x=0.24 (a), x=0.55 (b), and x=0.98 (c) at different applied magnetic fields. The ZFC curve is obtained in a similar procedure as FC except that the sample is cooled in a zero magnetic field, whereas measured with a field during the warm up. The deviation of the ZFC and FC curves at a lower magnetic field demonstrates superparamagnetic behavior, which may indicate the existence of ferromagnetic clusters inside the film. The blocking temperature (T_B) obtained from the peak of the ZFC curves at 100 Oe is approximately 90 K, 130 K and 70 K for x=0.24 (a), x=0.55 (b), and x=0.98 (c), respectively. The fact that T_B has a larger value for x = 0.55 sample is consistent with our TEM measurement which shows a larger cluster size as compared to x = 0.24 sample. With the increase of the applied field to 200 Oe, T_B peak shifts towards the lower temperature and finally merges with FC curve at 1000 Oe. This behavior is due to the increased magnetic field, which reduces the disorder in the crystal [8].

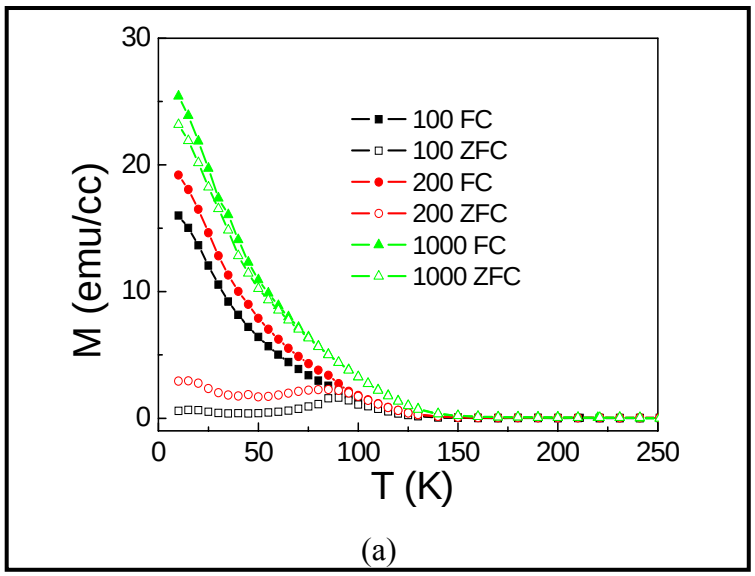

Figure 6-4 (a) FC (solid) and ZFC (open) M-T curves of the $Ge_{1-x}Mn_xTe$ film with x=0.24 at 100 Oe (square), 200 Oe (circle) and 1000 Oe (triangle).

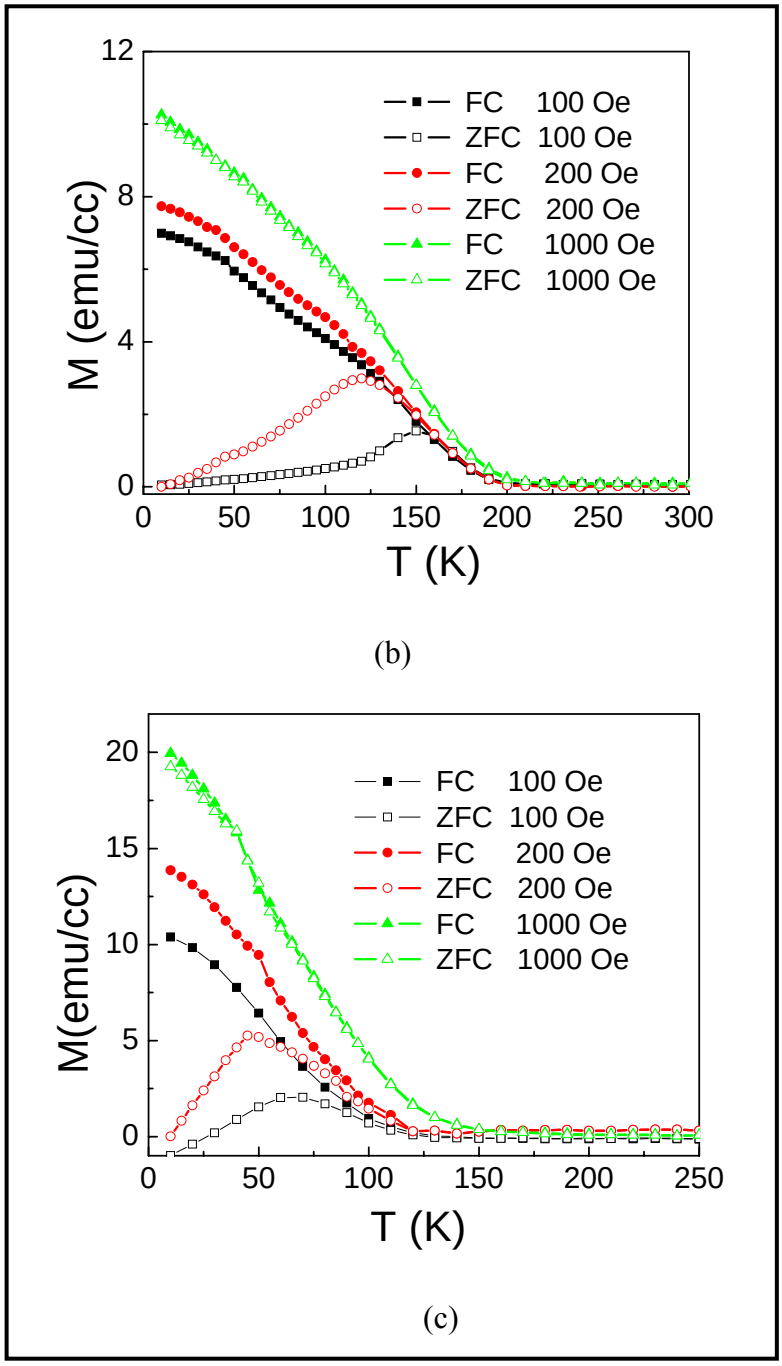

Figure 6-4 FC (solid) and ZFC (open) M-T curves of the $Ge_{1-x}Mn_xTe$ film with x=0.55 (b) and x=0.98 (c) at 100 Oe (square), 200 Oe (circle) and 1000 Oe (triangle).

6.1.3 Curie Temperature of $Ge_{1-x}Mn_xTe$ thin films

6.1.3.1 Methods to define the Curie temperature value

By definition, a material is ferromagnetic if there can exist regions within the material in which a spontaneous magnetization occurs. The temperature, below which the ferromagnetism occurs, is called the Curie temperature T_C. Curie temperature is a measure of the interaction energy associated with the ferromagnetism.

Since T_C refers to the temperature above which a ferromagnetic material loses its spontaneous magnetism, the value can be derived from FC M-T measurement when the magnetization disappears. Using this method, the critical temperature for $Ge_{1-x}Mn_xTe$ (x=0.98) sample is 130K. Another method is from the Curie-Weiss law that describes the magnetic susceptibility of a ferromagnet in the paramagnetic region above the Curie point which is [9]

$$\chi = \frac{C}{T - T_c}, \qquad (6\text{-}5)$$

where χ is the magnetic susceptibility which is given as χ = M/H, C is a material-specific Curie constant, T is absolute temperature and T_C is the Critical point where the magnetic susceptibility is theoretically infinite. The intercept of $1/\chi$ –T curve on the temperature axis gives 120K for x=0.98 sample, which is close to the value obtained from the first method.

However, as discussed in the previous section that our sample may contain clusters that may induce disordering effect, hence the shape of the M-T curve can be deviated from the standard Curie-Weiss theory. Instead, the ordering temperatures T_C

can be determined independently of the paramagnetic Curie-Weiss temperature using the data in the ordered region [10, 11]. In the molecular-field approximation, the magnetization M at $H \approx 0$ and T~T_C is expressed as

$$M^2(T) = AM_0{}^2\left(\frac{T_C - T}{T}\right), \qquad (6\text{-}6)$$

where M_0 is the spontaneous magnetization at 0 K and A is a constant related to the spin quantum number. Thus, T_C is obtained by extrapolating the steep linear part of M^2 vs. T plot to its temperature intercept as illustrated in Fig. 6-5 for $Ge_{1-x}Mn_xTe$ (x=0.98) sample. The value of the intercept to T axis gives 78 K as the Curie temperature.

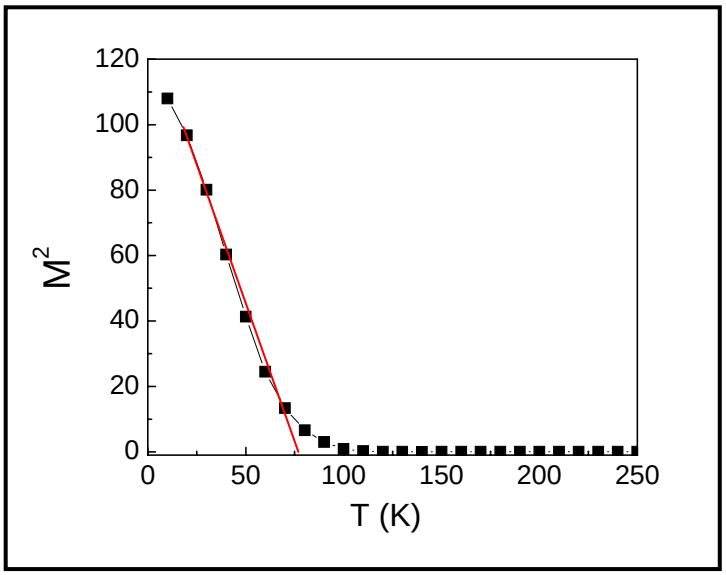

Figure 6-5 M^2 vs. T plotting for $Ge_{1-x}Mn_xTe$ (x=0.98) sample.

In addition, M can be measured as a function of H at various temperatures. The method known as Arrott plot is based on a power series expansion of the Brillouin function, whose argument is small in the vicinity of the Curie temperature [12]. The simplified equation of Arrott plot is given as

$$a(T-T_C)+bM^2=\frac{H}{M}, \qquad (6\text{-}7)$$

The equation indicates that if experimental data for M at different fields and temperature are plotted as M^2 versus H/M, at constant temperatures, they should be straight lines in the "critical region", namely when temperatures are not very far from the Curie point. The intercept of these lines with the H/M axis is positive if $T>T_C$, and negative if $T<T_C$. It is noted that the data for too low fields, that do not fit these straight lines, must be discarded. This is because that the M in the equation represents the measured magnetization of the bulk materials only if the domain alignment is complete. The M^2 versus H/M plotting for $Ge_{1-x}Mn_xTe$ (x=0.98) sample is shown in Fig. 6-6. The isotherm, which yields a slope closest to zero corresponds to $T = T_C$, which is around 95K. Although molecular-field approximation and Arrott plot gives slightly different value, the ordering temperature for x=0.98 is approximately Tc=85 ± 10K, taking into consideration of the experimental error bar in both methods.

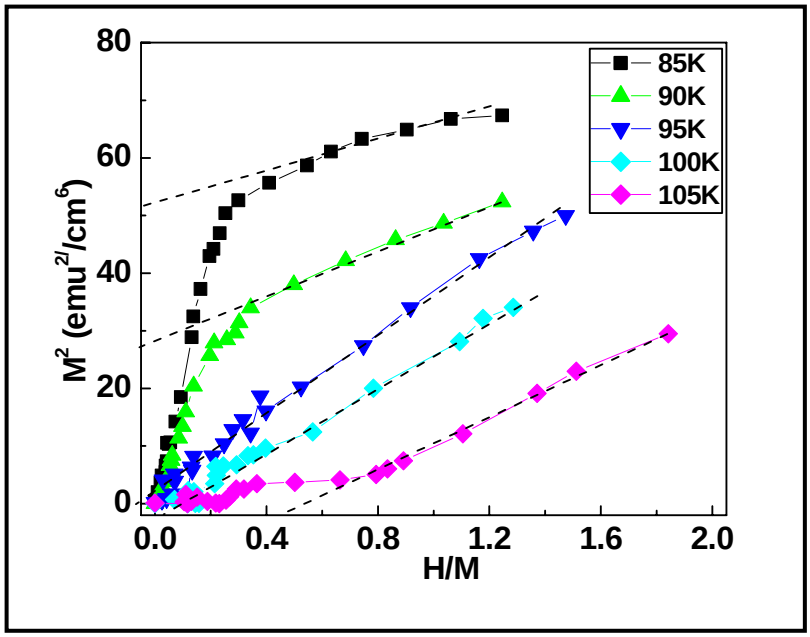

Figure 6-6 Arrot plot of $Ge_{1-x}Mn_xTe$ (x=0.98) sample.

6.1.3.2 Exchange Integral

From the spin-density functional theory for a homogenous system with randomly distributed localized spin, the T_C can be expressed as: [13]

$$k_B T_C = \frac{NS(S+1)}{3}\frac{{J_{pd}}^2 \chi_f}{(g\mu_B)^2} \quad , \tag{6-8}$$

where $N = \frac{4x}{a^3}$ is the Mn density in $Ge_{1-x}Mn_xTe$ rocksalt semiconductor with a lattice constant a, S is the spin of the Mn ions, J_{pd} is the localized-spin-itinerant-spin exchange coupling constant, and χ_f is the itinerant-hole magnetic susceptibility. The kinetic energy of the band holes gives a contribution to the susceptibility with a relation $\frac{\chi_f^{kin}}{(g\mu_B)^2} = \frac{{m_{hh}}^* k_F}{4\pi^2\hbar^2}$, (6-9)

where $m_{hh}^* = 1.2m_0$ is the hole effective mass of GeTe [14] and k_F is the Fermi wave vector. For weak interactions, the exchange energy of the spin-polarized parabolic-band model adds a contribution:

$$\frac{\chi_f^{ex}}{(g\mu_B)^2} = \frac{(m_{hh}^*)^2 e^2}{16\varepsilon\pi^4\hbar^4}, \tag{6-10}$$

where ε is the dielectric constant of the host semiconductor. In our case, $S = 5/2$ and N is Mn density in $Ge_{0.02}Mn_{0.98}Te$. The Fermi wave vector is $k_F = (3\pi^2 p/4)^{1/3}$, assuming the Fermi surface of GeTe is roughly spherical and p is the carrier concentration. Substituting the experimental data of $T_C = 85K$ and $p = 1\times10^{21}$ cm^{-3} which is obtained from transport measurement to be discussed in 6.2 into Eq. (5-8), we obtained the exchange coupling integral of $J_{pd} = 13.22\,eVA^3$ for x=0.98 sample. The same method is used to calculate the x=0.14, x=0.24 and x=0.55 sample, the J_{pd} value are 232.4 eVA^3, 207.2 eVA^3 and 162.79 eVA^3, respectively.

6.1.3.3 Mn composition dependence of Curie temperature

GeTe itself is a paramagnetic material and MnTe is an antiferromagnetic material. Figure 6-7 shows the reciprocals of the susceptibility χ versus temperature for MnTe grown at 200°C on BaF_2(111) substrate obtained from the M-T measurement at 100Oe field. The obtained antiferromagnetic Neel temperature at around 60K is due to the metastable ZB MnTe phase achieved in our non-equilibrium MBE system [15]. It is noted that the pure MnTe obtained in equilibrium-growth conditions is an antiferromagnetic semiconductor with a NiAs phase and a Neel temperature in a temperature range 305K-311K [16].

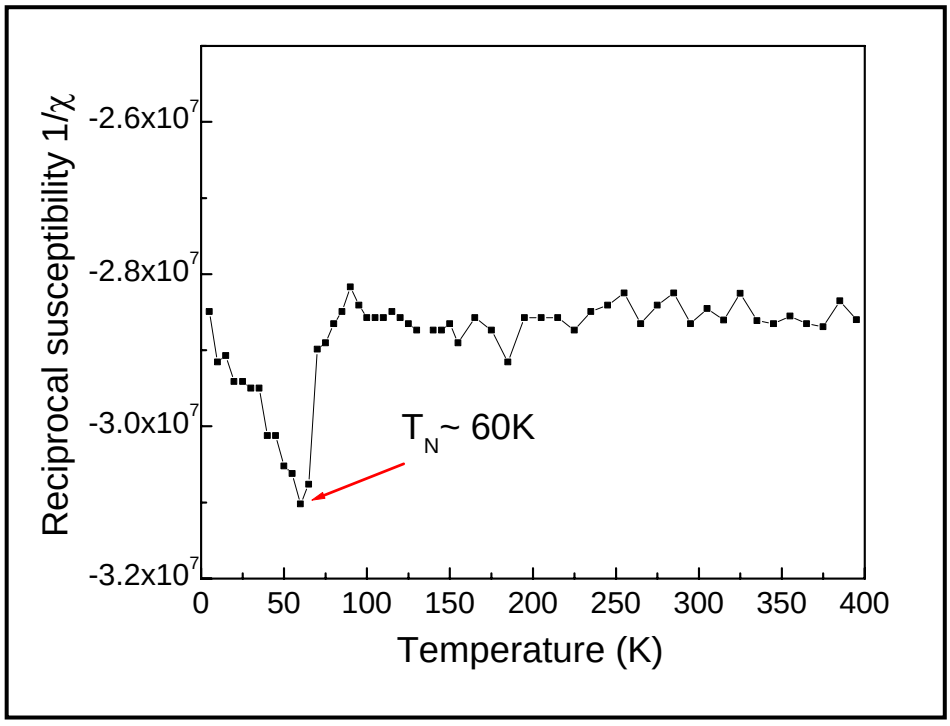

Figure 6-7 Reciprocals of the susceptibility versus temperature for MnTe

Curie Temperature T_C, determined by extrapolating the steep linear part of M^2 vs. T plot to the temperature intercept from M-T FC curve, as a function of Mn composition for $Ge_{1-x}Mn_xTe$ films is shown in Fig. 6-8. The T_C value increases with the increase of Mn composition and shows a maximum value around 150 K at x=0.55 and beyond this point it decreases. The dependence of T_C on x tends to follow a quadratic behaviour, which ascribes to the increase of the antiferromagnetic interaction between the Mn ions. It is known that the magnetic properties of Mn-doped IV-VI DMSs are caused by antiferromagnetic exchange interaction between Mn ions at low carrier concentration ~10^{17} cm^{-3} to 10^{19} cm^{-3}. On the other hand, the ferromagnetic order attributed to the Ruderman-Kittel-Kasuya-Yoshida (RKKY) interaction with the high hole concentration ~10^{21} cm^{-3} [17]. In this study, the carrier concentration of all the samples is around 3×10^{20} to 10^{21} cm^{-3} measured by a Hall system at room temperature using a 0.7 T electromagnet. The ferromagnetic order of the GeMnTe films with $0.14<x<0.98$ is probably caused by the RKKY interaction. However, the antiferromagnetic interaction mechanism also exists between the Mn ions and ZB MnTe phases as Mn composition increases, the antiferromagnetic interaction increases drastically causing the Curie temperature to decrease.

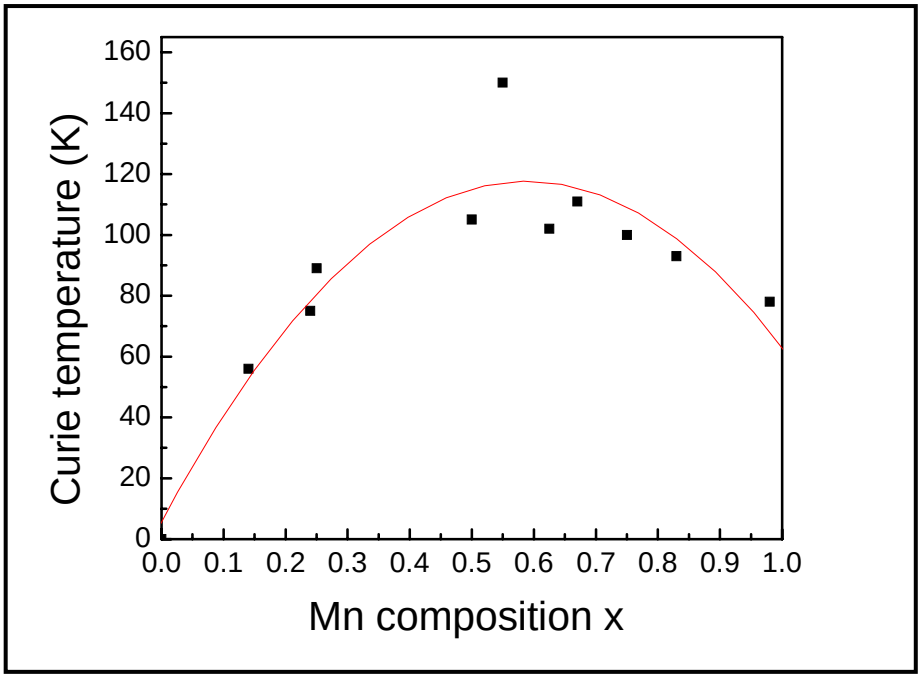

Figure 6-8 Mn composition dependence of Curie temperature

6.1.4 Magnetic Anisotropy

Figure 6-9 shows the M-H curves of $Ge_{1-x}Mn_xTe$ films (a) x=0.14, (b) x = 0.24, (c) x = 0.55 and (d) x=0.98 measured at 5K with magnetic field applied parallel (H || plane) and perpendicular (H ⊥ plane) to the sample plane. We do not observe distinct magnetic anisotropy for out of plane and in plane applied-field directions since the difference in coercivity ΔH_c is very small (around 20 Oe to 40 Oe) for these four samples. The results indicate that the magnetic moments are not all in-plane but part of them are out of plane. The existence of the out-plane magnetic moments could be due to the surface roughness which may induce spin disordering in the film surface. On the other hand, nanoscale grains or clusters with different orientations, as seen in the TEM images, have an effect on the domains formation under the crystal field. The crystal asymmetry hinders the displacement of the domain wall that might reduce the

ΔH_c. As a consequence, the magnetic anisotropy is weakened due to different orientation of the clusters.

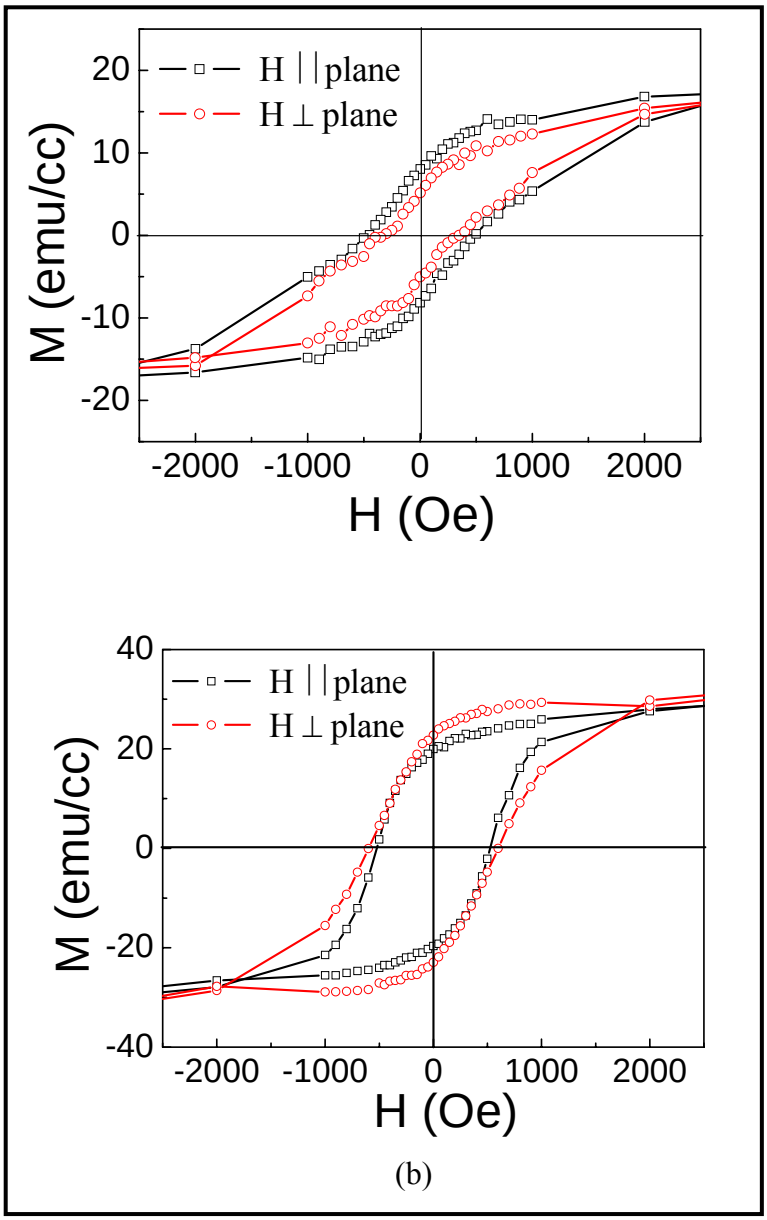

(b)

Figure 6-9 M-H curves of of $Ge_{1-x}Mn_xTe$ films (a) x=0.14 and (b) x=0.24 at 5 K with magnetic field applied in plane (H || plane) and out of plane (H ⊥ plane).

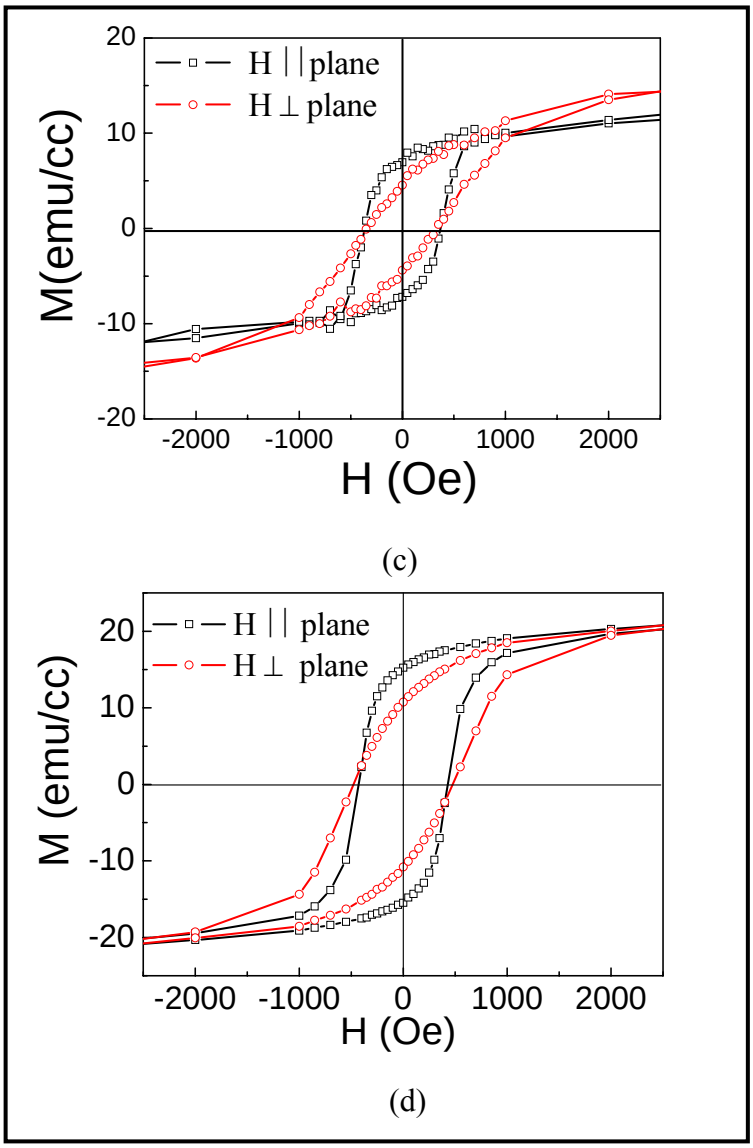

Figure 6-9 M-H curves of of $Ge_{1-x}Mn_xTe$ films (c) x = 0.55 and (d) x=0.98 at 5 K magnetic field applied in plane (H || plane) and out of plane (H ⊥ plane).

Figure 6-10 shows the temperature-dependent magnetization (M-T) of $Ge_{1-x}Mn_xTe$ films (a) x = 0.24, (b) x = 0.55 and (c) x=0.98 from 5 to 300 K with 100 Oe applied in plane (H || plane) and out of plane (H ⊥ plane). For x = 0.24 sample, there is not much difference in the strength of magnetization signals while for x = 0.55 and 0.98 samples, the magnetization is weaker in the H ⊥ plane as compared to H || plane configurations. The M-T results are consistent with the M-H loops shown in

Fig. 6-9 that the remnant magnetization M_r of out of plane is smaller than that of in-plane although the H_C remains the same for x=0.55 and 0.98 samples.

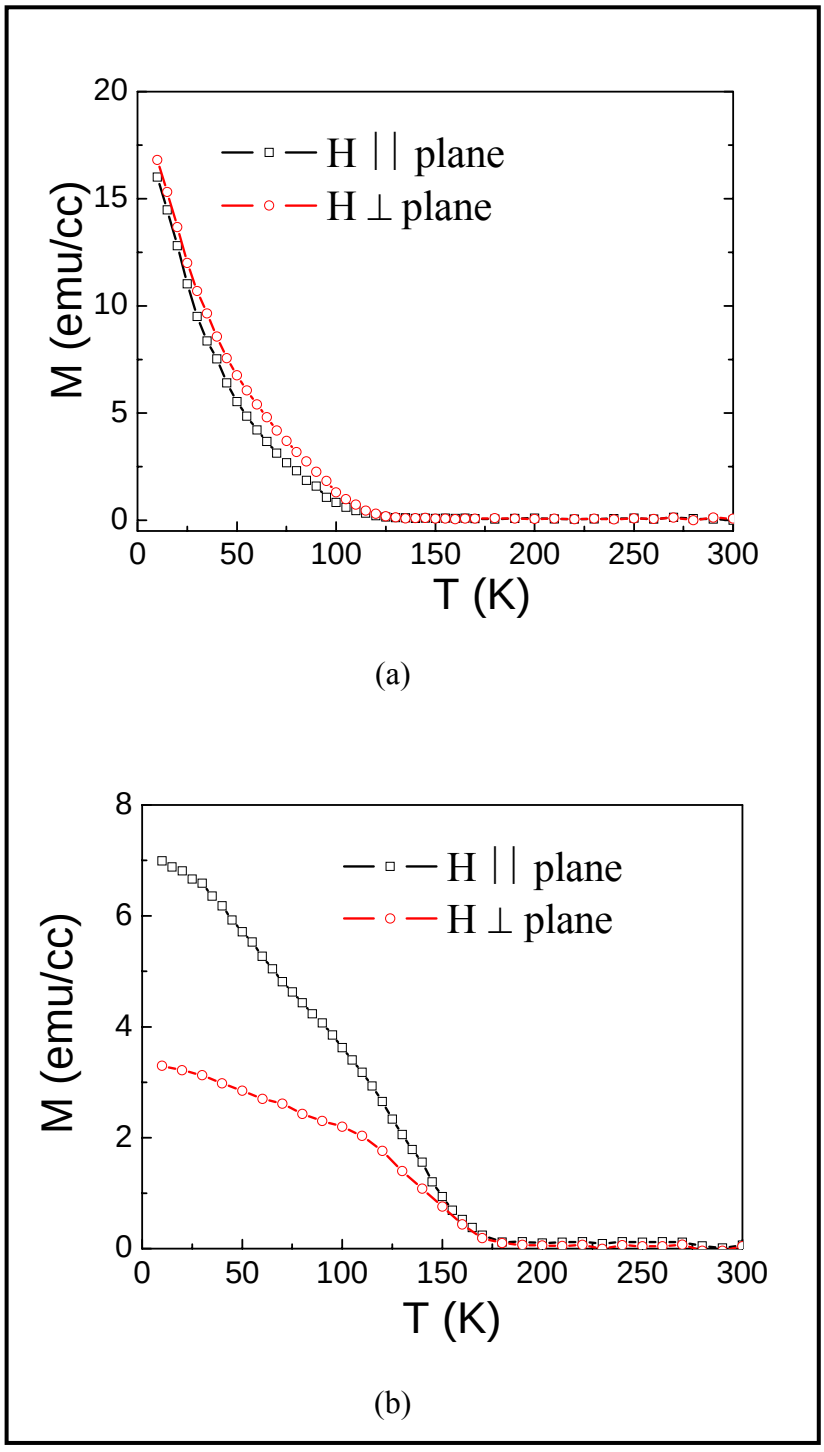

Figure 6-10 (a) M-T curves of of $Ge_{1-x}Mn_xTe$ films (a) x = 0.24 and (b) x=0.55 at 5 K with 100 Oe magnetic field applied in plane (H || plane) and out of plane (H ⊥ plane).

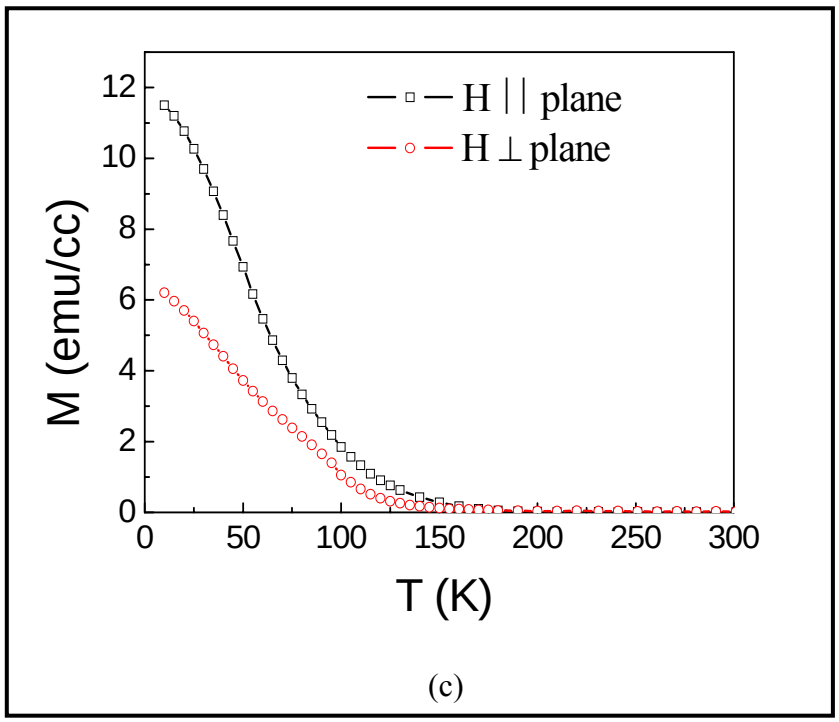

Figure 6-10 (c) M-T curves of of $Ge_{1-x}Mn_xTe$ films with x=0.98 at 5 K with 100 Oe magnetic field applied in plane (H || plane) and out of plane (H ⊥ plane).

Figure 6-11 shows the M-H loops of the $Ge_{1-x}Mn_xTe$ (x=0.98) films measured at 5K (a), 20K (b), 50K (c) and 80K (d) with H || plane and H ⊥ plane. The ratio of in-plane remnant magnetization M_r (||) to that of perpendicular remnant magnetization M_r (⊥) increases from 1.44 at 5K to 2.58 at 80K with the increase of the temperature. This result indicates that the magnetic moments are not all in the film plane but part of them are out of the film plane. The existence of the out-plane magnetic moments could be due to the surface roughness which may induce the spin disordering in the film surface. As the temperature decreases, the disordered spins are randomized, therefore the out-plane magnetic moments are enhanced at low temperature [18].

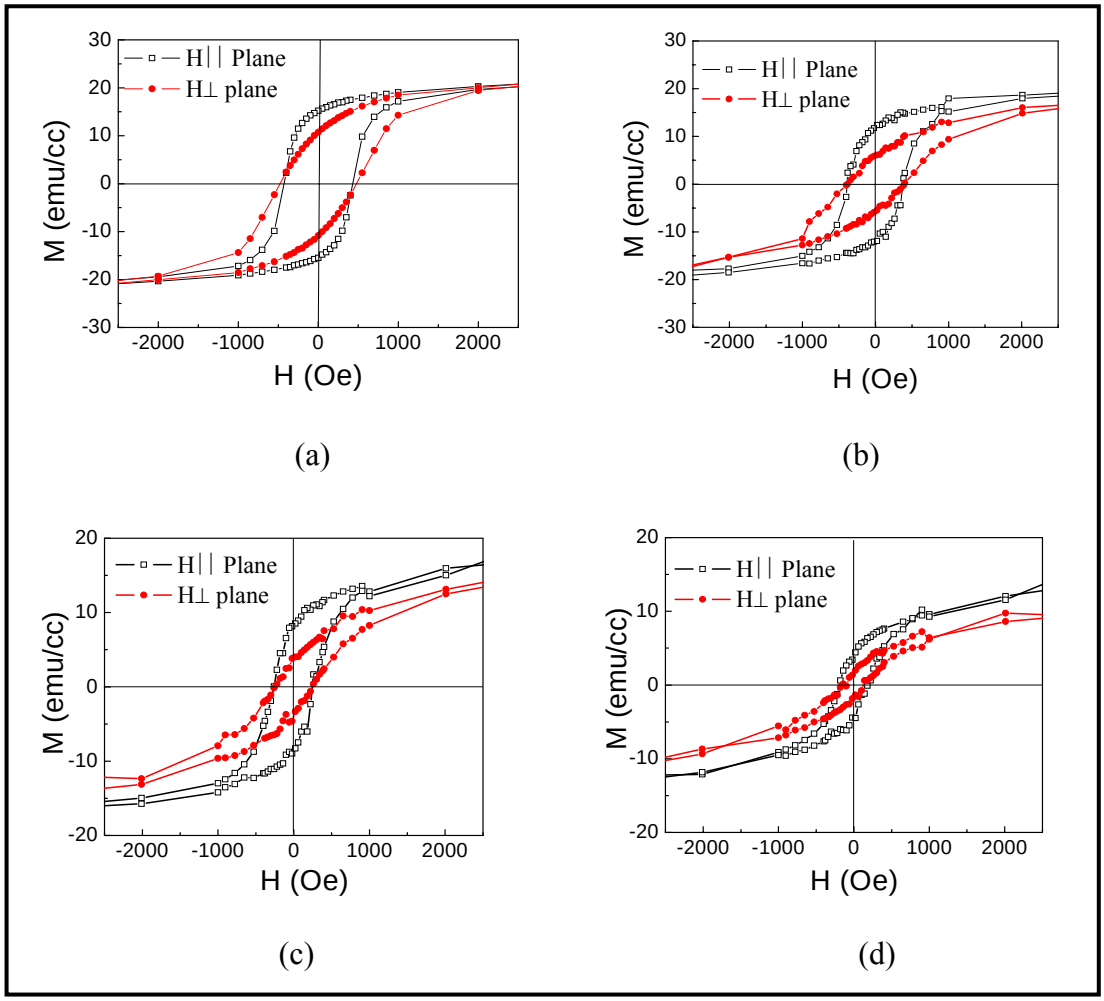

Figure 6-11 M-H loops of the $Ge_{1-x}Mn_xTe$ films x=0.98 measured at 5K (a), 20K (b), 50K (c) and 80K (d) with H || plane and H ⊥ plane.

6.2 Transport Properties of $Ge_{1-x}Mn_xTe$ thin films

6.2.1 Carrier concentration

$Ge_{1-x}Mn_xTe$ is a magnetic semiconductor, in which an amount of the nonmagnetic cation Ge^{2+} is replaced by the magnetic ion Mn^{2+}. It is well known that single crystal GeTe is a p-type material with the holes acting as the free carriers. Therefore, the free carriers in $Ge_{1-x}Mn_xTe$ films are also p-type. The hole concentration is measured by the Hall effect method using the Van der pawer configuration. In the Hall

measurement, a Hall voltage is generated perpendicular to the applied current and the magnetic flux, hence the Hall coefficient of the material R_H is obtained. The relationship between the Hall coefficient and the type density of charge carriers can be expressed as [19]

$$R_H = \frac{r}{e(p-n)}, \quad (6\text{-}11)$$

where r is the Hall scattering factor which is normally set to 1, e is the fundamental electric charge, p is the density of positive charge and n is the density of negative charge carriers in the material. For the case of $Ge_{1-x}Mn_xTe$ film with the hole as the dominant carrier, (6-11) can be simplified as

$$R_H = \frac{r}{e \times p}, \quad (6\text{-}12).$$

Therefore, the carrier density p is inversely proportional to the Hall coefficient. The carrier mobility is defined as $\mu_H = \frac{|R_H|}{\rho}$, (6-13)

Where μ_H is the Hall mobility and ρ is the electrical resistivity at zero magnetic flux density. The carrier concentration of $Ge_{1-x}Mn_xTe$ films ($0.14<x<0.98$) are in the range of 1×10^{20} cm^{-3} to 1×10^{22} cm^{-3}. Specifically, the hole concentration for x=0.14, x=0.24, x=0.55 and x=0.98 samples are $3\times10^{20}\,cm^{-3}$, $1.2\times10^{21}\,cm^{-3}$, $2.1\times10^{21}\,cm^{-3}$ and $1\times10^{21}\,cm^{-3}$, respectively. The corresponding hall mobility are 2.1 cm^2/Vs, 3.02 cm^2/Vs, 5.38 cm^2/Vs and 1.67 cm^2/Vs, respectively.

6.2.2 Temperature dependent resistivity

According to the Mott's criterion [20], the critical concentration n_c at the transition from non-conducting to metallic state satisfies the following criterion:

$$n_c^{1/3} a_H \approx 0.27, \tag{6-13}$$

where a_H is the first Bohr radius which is defined as:

$$a_H = \frac{\hbar^2 \varepsilon}{m^* e^2}. \tag{6-14}$$

and ε is the dielectric constant of the host material, m^* is the effective mass of a free carrier in the host conduction band. Using the dielectric constant $\varepsilon = 36$ [21] and hole effective mass $m^* = 1.2 m_0$ [14] for GeTe, we estimate the Bohr radius to be ~ 15.8 Å and the corresponding critical concentration is $\sim 5\times10^{18}\,\mathrm{cm}^{-3}$. Since our measured carrier concentration of $Ge_{1-x}Mn_xTe$ is in the range of 1×10^{20} to $1\times10^{22}\,\mathrm{cm}^{-3}$, which is much greater than $5\times10^{18}\,\mathrm{cm}^{-3}$, we expect the $Ge_{1-x}Mn_xTe$ films to be on the metallic side of the metal-insulator transition.

The resistivity (ρ) as a function of temperature (T) for $Ge_{1-x}Mn_xTe$ films (a) x=0.14, (b) x=0.24, (c) x=0.55 and (d) x=0.98 have been measured as shown in Fig. 6-12. All the samples exhibit an insulating-like trend at lower temperatures with a broad minimum (T_R is definded as the minimum of the R-T curve) at $T_R = 25 \pm 10\,\mathrm{K}$ $T_R = 120 \pm 10\,\mathrm{K}$, $T_R = 170 \pm 10\,\mathrm{K}$ and T_R = 95±10K for x=0.14, x=0.24, x=0.55 and x=0.98 respectively. In addition, they also show a more metallic-like behavior as temperature increases. Obviously, the change of the slope in ρ is not abrupt and there is an uncertainty in accurately determining the transition temperature at T_R. The change of the slope may correspond to FM-PM phase transition due to changes in

spin-related scattering. It is noted that GeTe is a p-type degenerate semiconductor with the Fermi-level ~0.3-0.5 eV lying inside the valence band [22] and show a metallic conduction, i.e. the resistivity increases with increasing temperature [23]. This metallic conduction may well describe our electrical transport in $Ge_{1-x}Mn_xTe$ for $T > T_R$ as it is evident from the positive temperature coefficient. The small change in the magnitude of ρ as a function of temperature indicates that the samples may be disordered.

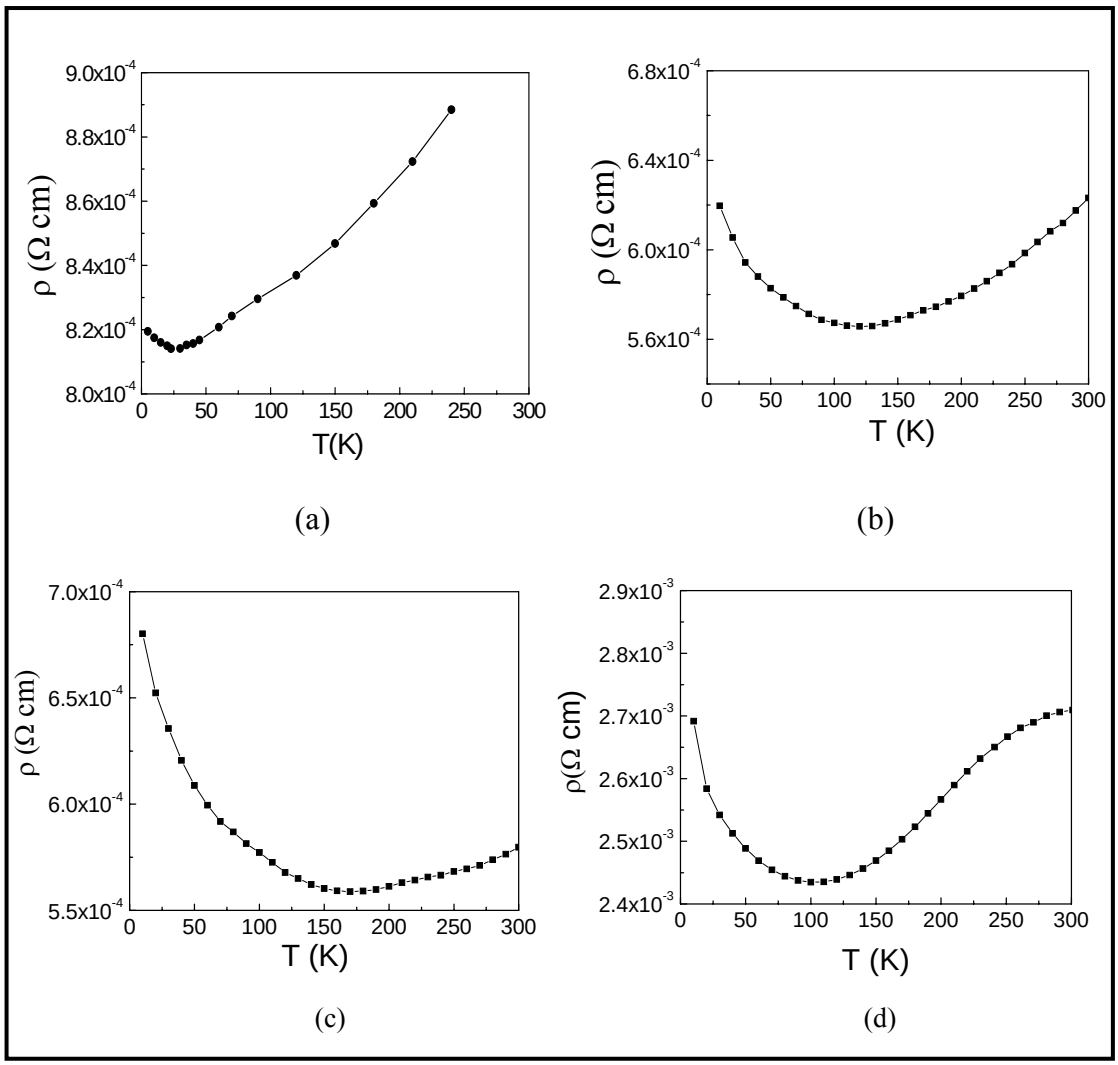

Figure 6-12 Resitivity as functions of temperatures for $Ge_{1-x}Mn_xTe$ films (a) x=0.14, (b) x=0.24 (c) x=0.55 and (d) x=0.98.

The low temperature range in the fitting curve can be fitted using the function

$$\rho = \rho_o \exp\left(\alpha T^{-\frac{1}{n}}\right), \text{ with n = 2, 3 or 4} \quad (6\text{-}16).$$

Our experimental data can be fitted with n=3 or n=4 with the experiment error bar. Figure 6-13 is an example of the fit of ρ for $Ge_{1-x}Mn_xTe$ films x=0.98 sample with n=3 (a) and n=4 (b). It shows that both n=3 and n=4 give very good fitting in the temperature range from 10-100K. n = 3 is the characteristic of variable range hopping (VRH) formula, which is valid when phonon-assisted hopping is dominated [24]. Whereas n=4 indicates that the hopping conduction within an impurity band might dominate at low temperatures [25].

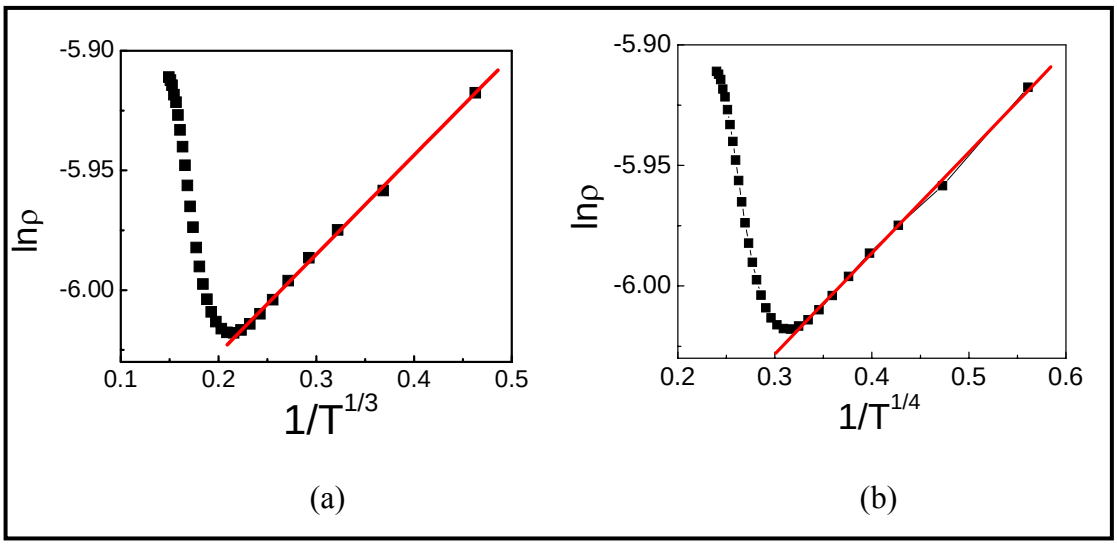

Figure 6-13 The fit of ρ for $Ge_{1-x}Mn_xTe$ films x=0.98 sample with n=3 (a) and n=4 (b).

Figure 6-14 shows the temperature dependent resisitivity of $Ge_{0.02}Mn_{0.98}Te$ sample with different in-plane applied field: zero field, 10K Oe and 30K Oe. It shows that the minima of the R-T curve decreases with the increase of the magnetic field,

indicating a negative in-plane magnetoresistance (MR). This negative MR is caused by the formation of the bound magnetic polarons. More detailed discussion of this negative MR will be presented in the section 6.2.3.

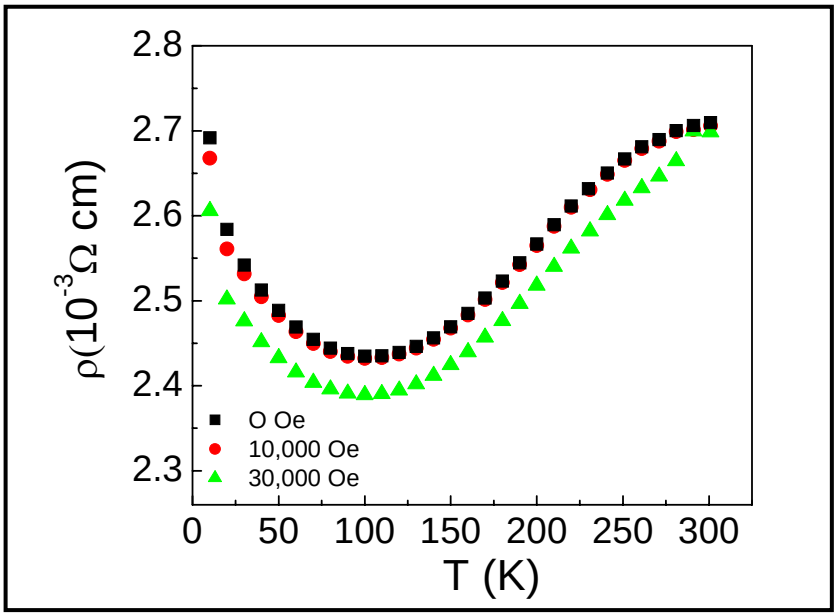

Figure 6-14 Temperature dependent resisitivity of the $Ge_{0.02}Mn_{0.98}Te$ film at applied field 0 Oe (square), 10 KOe (round) and 30 KOe (triangle).

6.2.2 Anomalous Hall Effect

Anomalous Hall effect (AHE) is measured in a Van der Pawer configuration illustrated in section 4.3.2. The Hall resistance R_H can be written as a sum of ordinary and anomalous Hall terms [26],

$$R_H = \frac{R_o}{d} B + \frac{R_s}{d} M_\perp \qquad (6\text{-}17)$$

where R_o and R_S are the ordinary and anomalous Hall coefficients, respectively; d is the film thickness; $M_\perp$ is the component of magnetization perpendicular to the sample surface. The first term in Eq. (6-17) denotes the ordinary Hall effect (OHE) that is inversely proportional to the carrier density, and the second term denotes the anomalous Hall effect (AHE) that is proportional to the magnetization.

Figure 6-15 presents the Hall resistance R_H curves of $Ge_{1-x}Mn_xTe$ (a) x=0.14, (b) x = 0.24, (c) x=0.55 and (d) x=0.98 samples at various temperatures. The magnitude of the AHE decreases with the increase of the temperature. All four samples show the slow increase of R_H with the increase of magnetic field in the high field region which corresponds to the OHE in *p*-type GeTe. The AHE curves of x=0.24 and x=0.55 samples at low temperatures show the similar hysteresis loops as MH loops.

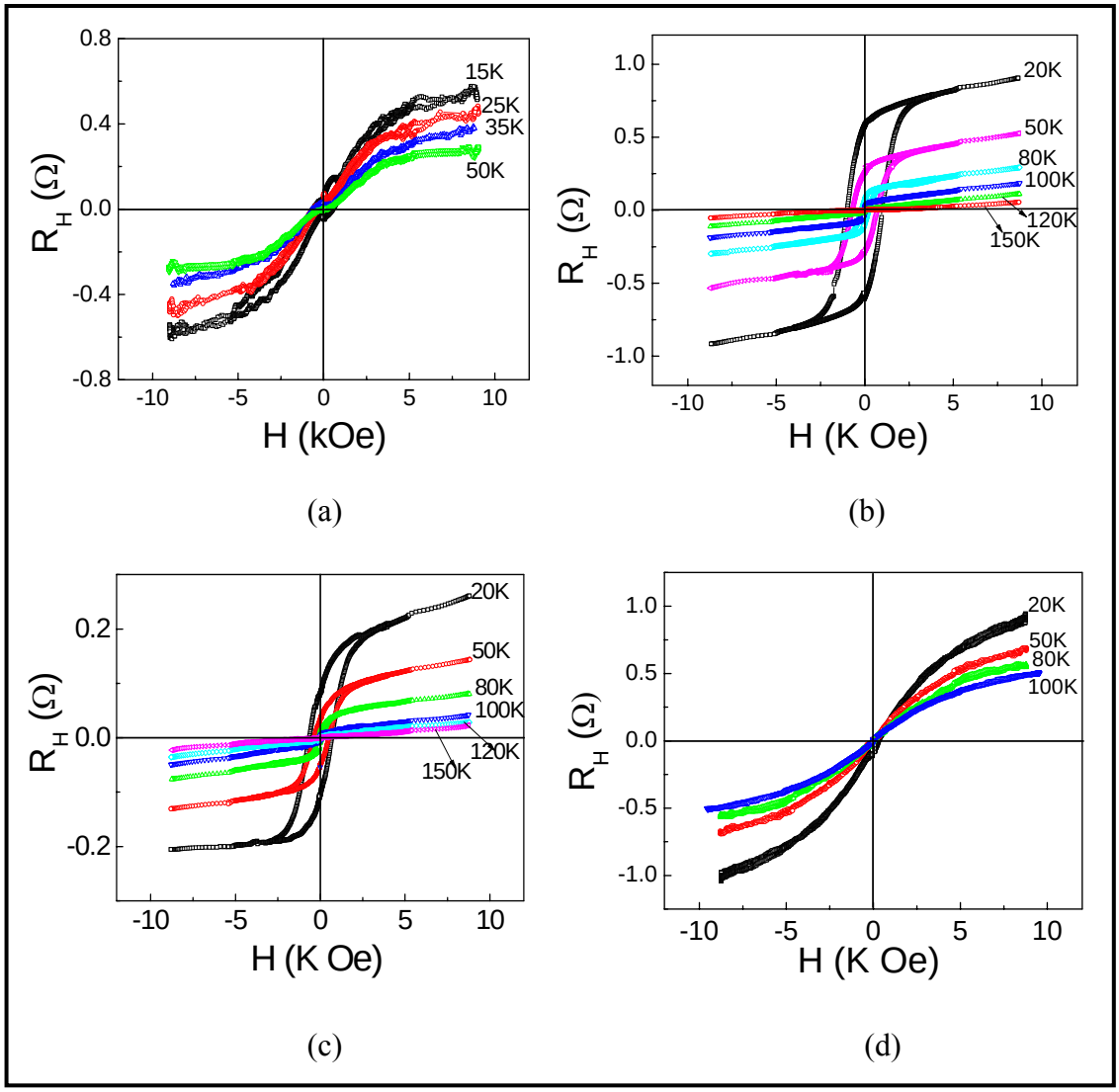

Figure 6-15 Temperature dependence of Hall Resistance (R_H) for $Ge_xMn_{1-x}Te$ (a) x=0.14, (b) x=0.24, (c) x=0.55 and (d) x=0.98 films.

Figure 6-16 shows the AHE curves of $Ge_{1-x}Mn_xTe$ (a) x = 0.24 and (b) x=0.55 at 20 K with respect to the M-H SQUID measurement, sharing the same horizontal field-axis. The field-dependencies of the R_H curves are in good agreement with the measured M-H curves. The Hc obtained from the two measurements are almost the same for both of the samples.

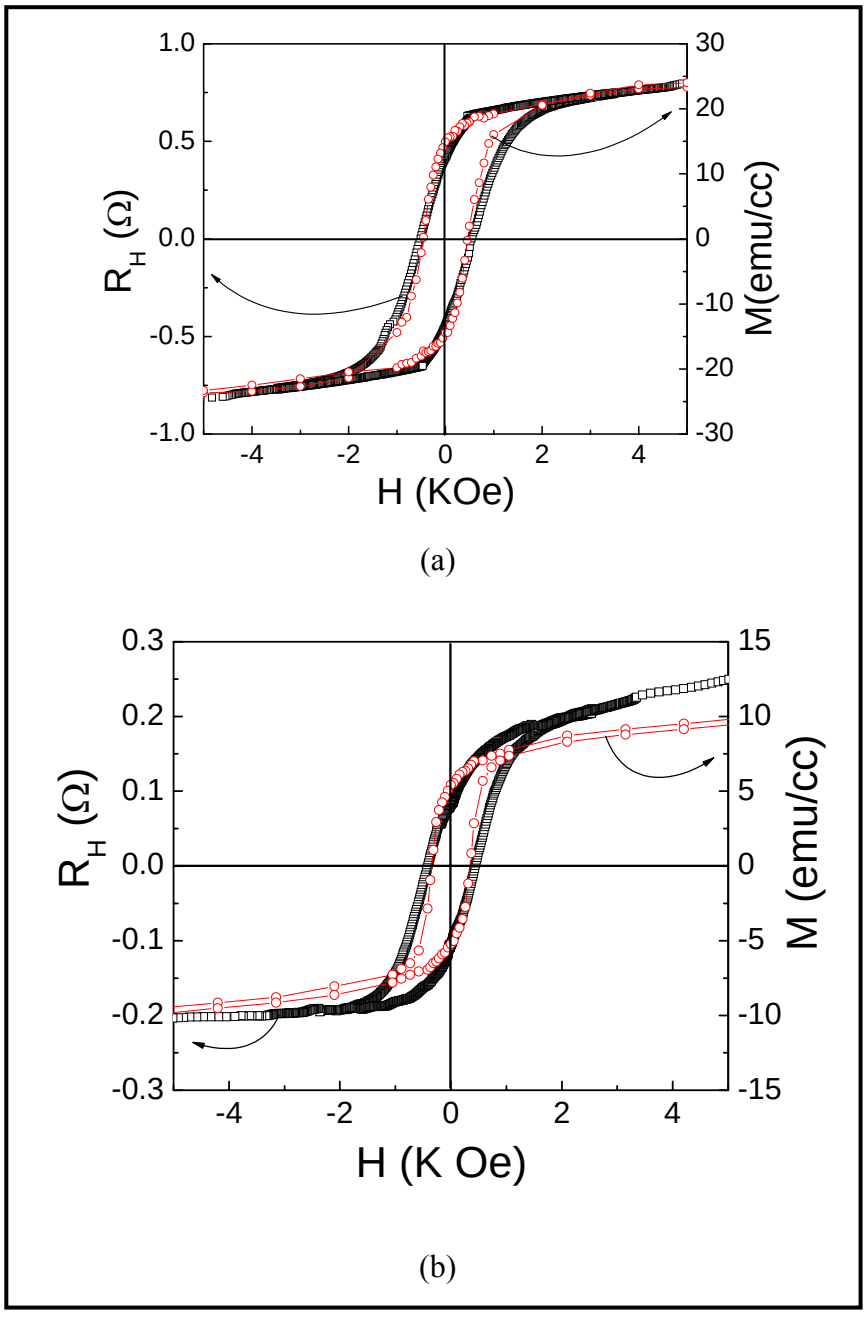

Figure 6-16 The M-H curves and R_H -H curves at 20K for (a) x = 0.24 and x = 0.55.

The observation of the AHE is usually recognized as a confirmation on the existence of intrinsic carrier induced ferromagnetism of the FM semiconductors since AHE represents ferromagnetic spin polarization of the charge carriers [27]. However, the AHE has also been observed for nonmagnetic material embedded with magnetic clusters such as $TiO_{2-\delta}$ films containing cobalt clusters [8]. From the HRTEM investigation, the non-uniformity is found to exist in the $Ge_{1-x}Mn_xTe$ film. The high Mn composition samples contain clusters and grains due to the phase segregation. Therefore, the observed AHE of $Ge_{1-x}Mn_xTe$ thin film is the combination of the carrier-induced ferromagnetism with the effect of the clusters. We note that the magnitude of the R_H is the highest for x=0.24 among four samples, indicating the better the sample uniformity, the stronger the AHE signal can be achieved.

In Eq. (6-17), R_S is related to the strength of spin-orbit coupling, which is proportional to ρ_{xx}^n with temperature-independent proportionality constant. Usually, n is either 1 or 2 depending on the origin of the effect; n = 1 reprents the skew-scattering mechanism, whereas n=2 represents the side-jump mechanism. The important role of AHE in carrier mediated ferromagnetism in DMS has been extensively discussed by Jungwirth et. al [28], and also demonstrated experimentally in the case of $Ga_{1-x}Mn_xAs$ [29]. To ascertain the origins of AHE, we examine the scaling relationship $\rho_{xy} \propto \rho_{xx}^n$ at 20 K, for $Ge_{1-x}Mn_xTe$ with x ranging from 0.14 to 0.98. The four points shown in Figure 6-17 are x=0.14, 0.24, 0.55 and 0.98 samples, the least-square fit gives a value of n = 1.06±0.16. The behavior of AHE could be due to hopping transport or extrinsic skew scattering [30] as both models predict linear

scaling behavior.

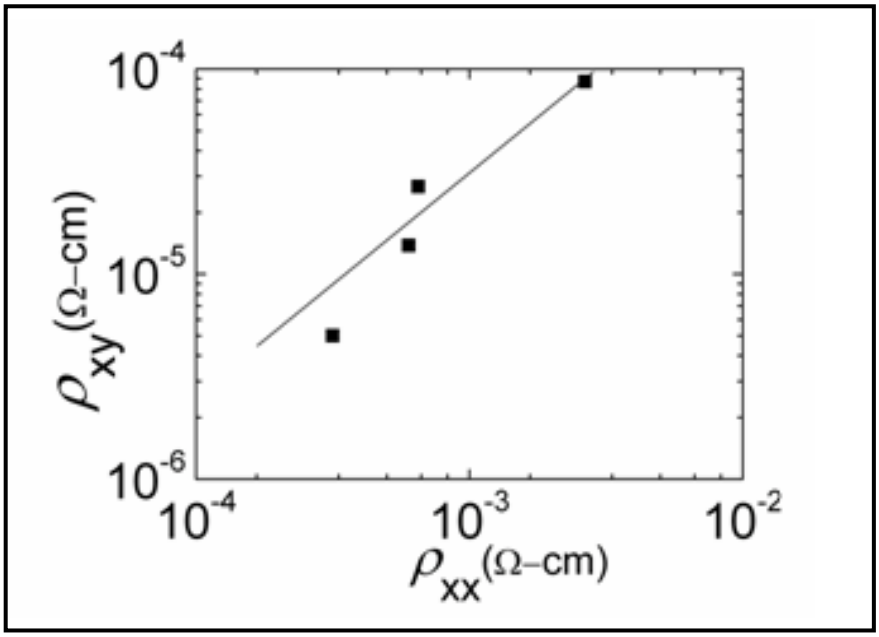

Figure 6-17 The scaling behavior between ρ_{xy} and ρ_{xx}^{n}, with n = 1.06 gives the least-squared fit.

6.2.3 Magnetoesistance

In Magnetoresistance (MR) measurement, a magnetic field is used to amplify or induce the magnetic interaction effects in the material. Therefore, by MR measurement, one can obtain information about the magnitude of the spin interactions in the materials and their effects on the transport properties. (MR) is defined as

$$MR = \frac{[\rho(H) - \rho(0)]}{\rho(0)}, \tag{6-18}$$

where $\rho(H)$ is the resisitivity when the magnetic field is applied and $\rho(0)$ is the resisitivity at zero magnetic field. The resistivity is measured by the four probe configuration as shown in section 4.3.2. The magnetic field is applied in-plane (H || plane) and perpendicular to sample plane (H ⊥ plane). We find that MR is isotropic

and its magnitude is not affected in both configurations.

Figure 6-18 shows the MR curves of $Ge_{1-x}Mn_xTe$ (x=0.24) measured in the case of H in-plane at temperature 20 K and 50 K with respect to the M-H measurement. The MR results show good correlation with the measured M-H curves, sharing the same horizontal field-axis. At T = 20 K, the MR shows a clear hysteresis loop. A magnetic field corresponding to the maximum in MR at 445 Oe, is almost equal to the coercivity (H_C) determined by magnetization measurements. With the increase of the temperature, the magnitude in MR decreases and at T = 50 K, the maximum in MR occurs at field which corresponds to a smaller H_C ~290 Oe in the M-H curve. Although the MR % in $Ge_{1-x}Mn_xTe$ is quite small, these MR features resemble those of GMR in granular solids [31].

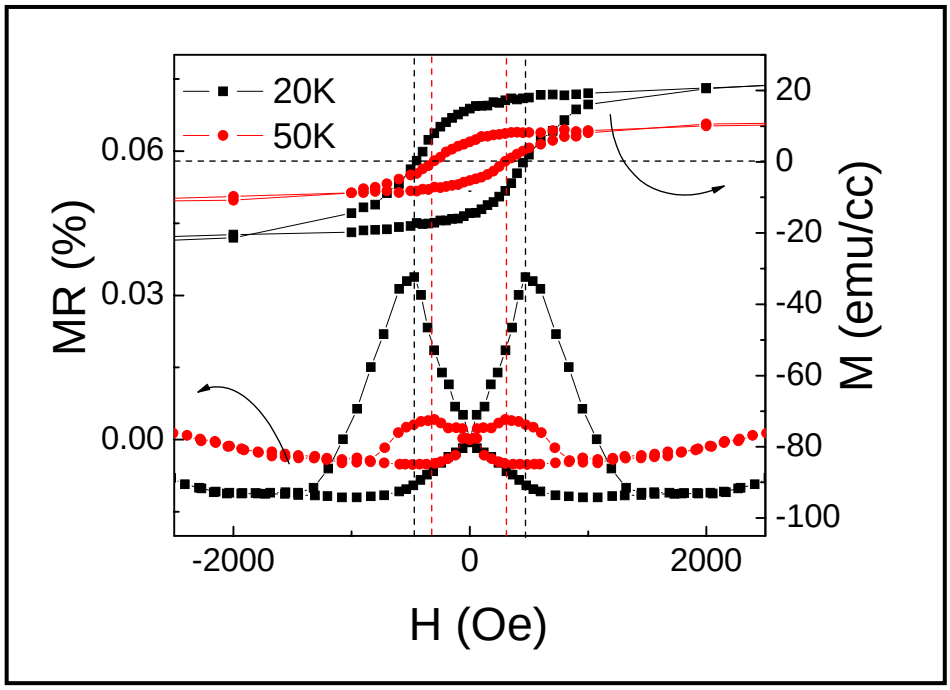

Figure 6-18 MR curves of $Ge_{1-x}Mn_xTe$ (x = 0.24) in the case of H || plane at temperature 20 K and 50 K with respect to the M-H results.

Figure 6-19 shows the temperature dependence of the MR effect for x = 0.14 (a) and x=0.24 (b) samples at various temperature with applied field up to 7 T. It is found that in the whole temperature range, the MR ratio is small. At 4 K, the MR effect decreases with increasing field and reaches a plateau at high field due to weak localization effect induced by disorder for both samples. With increasing temperature, the negative MR decreases and finally changes to a very small positive MR effect at 20 K and 50K for x = 0.14 and 0.24 samples, respectively. One expects proportionality to H^2 for diamagnetic semiconductors. This prediction is clearly observed at higher temperature ($T \geq 50$ K). Similar MR behavior are observed for x = 0.55 and x = 0.98 samples. The negative MR can be explained by the formation of bound magnetic polarons (BMP) by the exchange interaction between localized carriers and magnetic ions [6, 32]. With applied magnetic field, the impurities are polarized all over the sample and all Mn spins are progressively aligned, which makes the holes increasingly mobile and hence cause the resistance to decrease.

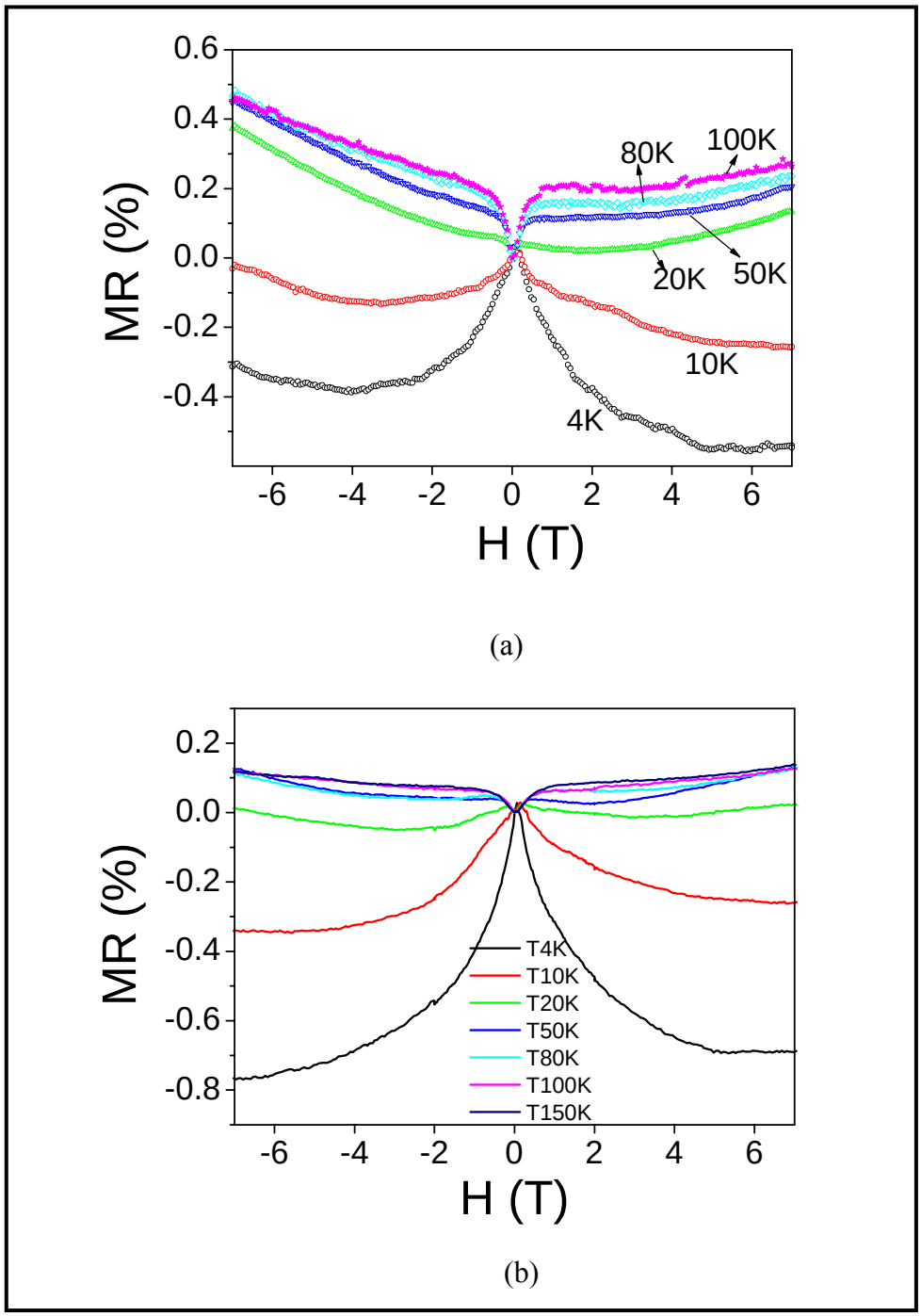

Figure 6-19 The MR curve as a function of temperature for x = 01.4 (a) and (b) 0.24 samples.

6.3 Origin of ferromagnetism in $Ge_{1-x}Mn_xTe$

Table 6-1 summarizes the experimental results obtained for $Ge_{1-x}Mn_xTe$ x=0.14, x=0.24, x=0.55 and x=0.98 samples. All the samples have relatively high hole concentrations in the range of 3×10^{20} to $2\times10^{21}\,cm^{-3}$. It has been proposed that in $Ge_{1-x}Mn_xTe$, the long-range RKKY interaction, which proceeds via a coupling between the magnetic ion and the mobile charge carriers, dominates the magnetic behavior at high carrier concentration. On the other hand, the HRTEM results suggest that the existence of inhomogeneity and nano-clusters in the Mn distributions at high doping concentration. We observe the occurrence of the superparamagnetic behavior that is exhibited in the M-T curves as well as the deviation of the FC curves from the Weiss mean-field theory. These strongly indicate the presence of the disorder localization and suggest the exchange interactions inside the samples may not be homogeneous. Additionally, we have determined that the paramagnetic Curie-Weiss temperature θ_p is larger than the Curie temperature T_C, which signifies that magnetic short range order remains even above T_C. The origin of short-range ordering could possibly come from FM clusters. Moreover, the isotropy of MR and M-H curves suggest the magnetic moments are not all in-plane but part of them are out of plane. The existence of the out-plane magnetic moments could be due to surface roughness which may induce spin disordering in the film surface.

Despite the fact that the magnetization measurements indicate the presence of superparamagnetism in the film, we clearly observed the AHE behavior. Our result is consistent with the recent report by S. R. Shinde *et. al.* on the co-occurrence of

superparamagnetism and AHE in Co doped rutile $TiO_{2-\delta}$ films due to the presence of cobalt clusters [8]. This raises the question regarding the use of the AHE as a test of the intrinsic nature of ferromagnetism in DMS. $\rho_{xy} \propto \rho_{xx}^{n}$ gives the least-square fit value of n = 1.06±0.16, which could be due to extrinsic skew scattering. No magnetic secondary phases such as Mn_5Ge_3 and $Mn_{11}Ge_8$ are found from both the structural and conductivity characterizations. It is possible that the spinodal decomposition in the form of coherent-phase FM nanoclusters may exist. Since spinodal decomposition does not involve the precipitation of another crystallographic phase, it is not easily detectable experimentally [33].

Last but not least, our resistivity behavior appears to be dirty metallic-like, which is likely due to the weak localization effect of disordering. This is similar to the case of $Ga_{1-x}Mn_xAs$ in the metallic phase for certain value of x [34]. It is noteworthy that antiferromagnetic interaction between the Mn ions and ZB MnTe phases could lower the T_C value when the Mn composition is high.

Table 6-1 Mn composition *x*; lattice constant *a*, hole carrier-concentration *p*; resistivity at room temperature ρ; blocking temperature T_B; Curie temperature T_C; T_R at $\rho_{\min}$; paramagnetic Curie-temperature θ_p; exchange integral J_{pd} and bandgap energy E_g.

x	0.14	0.24	0.55	0.98
a (nm)	0.5958	0.5939	0.5895	0.5823
p (cm^{-3})	3×10^{20}	1.2×10^{21}	2.1×10^{21}	1.0×10^{21}
ρ (Ωcm)	8.5×10^{-4}	6.2×10^{-4}	5.8×10^{-4}	2.7×10^{-3}
T_B (K)	50	90	130	70
T_C (K)	56	95	160	85
T_R (K)	25 ± 10	120 ± 10	170 ± 10	95 ± 10
θ_p (K)	100	135	180	120
J_{pd} [eV Å^3]	232.4	207.2	162.79	13.22
E_g (eV)	0.87	0.92	0.96	1.02

6.4 Summary

In summary, the magnetic and transport properties of $Ge_{1-x}Mn_xTe$ thin films are discussed in this chapter. The report mainly focused on 4 characteristic samples with Mn composition of x=0.14, 0.24, 0.55 and 0.98. The clear hysteresis loops are observed for these samples with the concurrence of the superparamagnetism. We determine the Curie temperature T_C using the data in the ordered region. The

dependence of T_C on the Mn composition follows a quadratic behavior, which ascribes to the increase of the antiferromagnetic interaction. We do not observe distinct magnetic anisotropy, indicating the magnetic moments are not all in-plane but part of them are out of plane.

The samples show high carrier concentration and tend to be on the metallic side of the metal-insulator transition. The temperature-dependent resistivity ρ(T) measurement exhibits an upturn at low temperature, which could relate to the ferromagnetic-paramagnetic (FM-PM) transition. At low temperature range, the hopping conduction tends to dominate the resistivity behavior. Anomalous hall effect (AHE) is clearly observed in the sample which indicates the extrinsic skew scattering may be involved. Our magnetoresistance (MR) displays a clear hysterestic loop at low temperature which reseumbles that of giant-magnetoresistance (GMR) granular system in solids. The temperature dependent MR behavior may be accounted for the BMPs model. We correlate the observation of the isotropy of MR and M-H curves with the formation of $Ge_{1-x}Mn_xTe$ FM clusters embedded in GeTe matrix.

References:

[1] T. Ohoyama, "X-ray and Magnetic Studies of the Manganese-Germanium System", J. Phys. Soc. Jpn., **16,** 1995 (1961);

[2] Y. Tawara and K. Sato, "On the Magnetic Anisotropy of Single Crystal of Mn_5Ge_3" J. Phys. Soc. Jpn., **18,** 773 (1963);

[3] N. Yamada, "Atomic Magnetic Moment and Exchange Interaction between Mn

Atoms in Intermetallic Compounds in Mn-Ge System " J. Phys. Soc. Jpn., **59** 273 (1990).

[4] T. Matsui, M. Shigematsu, S. Mino, H. Tsuda, H. Mabuchi and K. Morii, "Formation of unkown magnetic phase by solid state reaction of thin multilayered films of 75 at% Mn-25% Ge" J. Mag. Mag. Mat., **192,** 247 (1999) ;

[5] M. Berciu and R. N. Bhatt, "Mean-field approach to disorder effects on ferromagnetism in $Ga_{1-x}Mn_xAs$", Physica B-Cond. Mat., **312,** 815 (2002);

[6] A. C. Durst, R. N. Bhatt and P. A. Wolff , "Bound magnetic polaron interactions in insulating doped diluted magnetic semiconductors" Phys. Rev. B, **65,** 235205 (2002);

[7] R. N. Bhatt, M. Berciu, M. D. Kennett and X. Wan, "Diluted magnetic semiconductors in the low carrier density regime" J. of Supercond, **15, 7**1 (2002).

[8] S. R. Shinde, S. B. Ogale, J. S. Higgins, H. Zheng, A. J. Millis, V. N. Kulkarni, R. Ramesh, R. L. Greene, and T. Venkatesan "Co-occurrence of Superparamagnetism and Anomalous Hall Effect in Highly Reduced Cobalt-Doped Rutile $TiO_{2-\delta}$ Films**",** Phys. Rev. Lett., **92**, 166601 (2004).

[9] Charles Kittel "Introduction to Solid state physics" 7th edition, New York ; Singapore : John Wiley & Sons, c1996

[10] R. W. Cochrane, M. Plischke and J. O. Strom-olsen "Magnetization studies of $(GeTe)_{1-x}(MnTe)_x$ pseudobinary alloys", Phys. Rev. B, **9,** 3013 (1974);

[11] Y. Fukuma, H. Asada, N. Nishimura and T. Koyanagi, "Ferromagnetic properties of IV-VI diluted magnetic semiconductor $Ge_{1-x}Mn_xTe$ films prepared by radio frequency sputtering", J. Appl. Phys. **93,** 4034 (2003).

[12] Jiles, David., "Introduction to magnetism and magnetic materials"**,** London : Chapman & Hall, 1998, 2nd ed

[13] T. Jungwirth, J. Konig, J. Sinova, J. Kucera, and A. H. MacDonald, "Curie temperature trends in (III,Mn)V ferromagnetic semiconductors", Phys. Rev. B, **66**, 012402 (2002).

[14] J. E. Lewis, "Optical properties and energy gap of GeTe from reflectance studies**"** Phys. Status Solidi B, **59**, 367 (1973).

[15] W. Szuszkiewicz, B. Hennion, B. Witkowska, E. Lusakowska, A. Mycielski, "Neutron scattering study of structural and magnetic properties of hexagonal MnTe" Phy. Stat. Sol. (c), **2**, 1141 (2005).

[16] E. Uchida, H. Kondoh, N. Fukuoka, "Magnetic Properties of Nickel Telluride", J. Phys. Soc. Jap., **11,** 27 (1956).

[17] T. Story, R. R. Gałązka, R. B. Frankel, P. A. Wolff, "Carrier-concentration Induced Ferromagnetism in PbSnMnTe" Phys. Rev. Lett., **56,** 777 (1986).

[18] X. J. Xu, Q. L. Ye, G. X. Ye, "Temperature dependence of coercivity behavior in iron films on silicone oil surfaces", Physics Letters A, **361,** 429 (2007).

[19] Lake Shore 7500/9500 Series Hall System User's Manual

[20] N. F. Mott, Metal-Insulator Transitions (Taylor & Francis, London, 1974).

[21] N. E. Zein, V. I . Zinenko, and A. S. Fedorov, "Abinitio Calculations of Phnon Frequencies and Dielectric-constants in A4B6 compounds", Phys. Lett. A, **164**, 115 (1992).

[22] R. Tsu, W. E. Howard, and L. Esaki, "Optical and Electrical Properties and Band

Structure of GeTe and SnTe", Phys. Rev., **172**, 779 (1968).

[23] S. K. Bahl and K. L. Chopra,. "Amorphous versus Crystalline GeTe Films. III. Electrical Properties and Band Structure", J. Appl. Phys**., 41**, 2196 (1970).

[24] S.J. Lee, J.B. Ketterson and N. Trivedi, "Metal-insulator transition in quasi-two-dimensional Mo-C films", Phys. Rev. B, **46**, 12695 (1992).

[25] R. Rosenbaum, "Crossover from Mott to Efros-Shklovskii variable-range-hopping conductivity in In_xO_y films", Phys. Rev. B, **44** , 3599 (1991).

[26] L. Berger and G. Bergmann (1979) the Hall effect and Its applications (Eds. Chien, C. L. and Westgate, C. R.) Plenum, New York

[27] T. Fukumura, H. Toyosaki and Y. Yamada, "Magnetic oxide semiconductors", Semicond. Sci. Technol., **20,** S103 (2005).

[28] T. Jungwirth, Q. Niu, and A. H. MacDonald, "Anomalous Hall effect in ferromagnetic semiconductors", Phys. Rev. Lett., **88**, 207208 (2002).

[29] H. K. Choi, Y. S. Kim, S. S. A.Seo, I. T. Jeong, Lee, W. O. Oh, Y. S Kim, J. C. Woo, T. W. Noh, Z. G. Khim, Y. D. Park, S. H. Chun, "Evidence of metallic clustering in annealed Ga1-xMnxAs from atypical scaling behavior of the anomalous Hall coefficient", Appl. Phys. Lett. **89,** 102503 (2006).

[30] N. Nagaosa, "Anomalous Hall effect - A new perspective", J. Phys. Soc. Jpn. **75**, 042001, (2006).

[31] J. Q. Xiao, J. S. Jiang, and C. L. Chien, "Giant magnetoresistance in nonmultilayer magnetic systems", Phys. Rev. Lett., **68,** 3749 (1992).

[32] A. Kaminski and S. Das Sarma , "Magnetic and transport percolation in diluted

magnetic semiconductors", Phys. Rev. B., **68,** 235210, (2003).

[33] T. Dietl, "Self-organized growth controlled by charge states of magnetic impurities", Nat. Mat., **5**, 673 (2006).

[34] F. Matsukura, H. Ohno, A. Shen and Y. Sugawara, "Transport properties and origin of ferromagnetism in (Ga,Mn)As", Phys. Rev. B., **57,** R2037 (1998).

CHAPTER 7 SUMMARIES AND RECOMMENDATIONS

7.1 Summaries

The work reported in this thesis focus on the fabrication and characterization of $Ge_{1-x}Mn_xTe$ ferromagnetic semiconductors. Structural, magnetic, and transport properties are investigated in details. The important findings and conclusions are summarized as follows.

(1) MBE method is used to synthesize $Ge_{1-x}Mn_xTe$ thin films. A few monolayers of MnTe are grown as a buffer to compensate the substrate surface defects. Two critical parameters namely the flux ratio and the growth temperature are optimized during the growth. The optimum growth condition is found to be with flux ratio of Te/Ge~1.5 to 2, Te/Mn~13 to 70 and the growth temperature ~200^{o}C. We observe the spot-like RHEED pattern at the end of the growth indicating the island growth mode. The Mn composition is varied by the change of Mn cell temperature. The $Ge_{1-x}Mn_xTe$ films with composition range of $0.14<x<0.98$ are successfully grown.

(2) $Ge_{1-x}Mn_xTe$ films crystallize in rocksalt structure with (111) orientation preferred. No secondary phases such as Mn_5Ge_3 and $Mn_{11}Ge_8$ are observed from the XRD measurement. The peak of GeMnTe (222) shifts towards the larger angle with the increase of the Mn composition. The lattice constant deduced from the GeMnTe (222) peak has a linear relationship with the Mn composition.

(3) The HRTEM results show that the non-uniformity exists in the film. The samples are not homogeneous and may contain clusters or grains with different sizes and compositions. Moreover, ZB and NaCl structures are distinguished in the high Mn composition sample, which may be subject to the phase segregation. We observe the bright and the dark area in the HRTEM picture. The dark area has a higher Mn content as compared to the bright area. This strongly suggests the bright region consists mainly of GeTe matrix and thus it does not contribute significantly to the magnetic properties.

(4) The direct band-gap (E_g) values of the $Ge_{1-x}Mn_xTe$ films are deduced from the optical absorption measurement. The results show that the band-gap of magnetic semiconductor $Ge_{1-x}Mn_xTe$ with $0.14<x<0.98$ in a manner qualitatively similar to the nonmagnetic semiconductor counterpart GeTe and MnTe. All the E_g values all fall in the range of 0.7 eV to 1.3 eV, which is the bandgap of rocksalt GeTe and NiAs MnTe, respectively.

(5) The field-dependent magnetization (M-H) measurements of $Ge_{1-x}Mn_xTe$ thin films show the clear hysteresis loop. The temperature dependent magnetization measurements reveal that the FC curves of some samples deviate from the Weiss mean-field theory, which suggest that the shape of M-T curves is controlled by disorder in the sample. Moreover, the deviation of the ZFC and FC curves at a lower magnetic field demonstrates superparamagnetic behavior, which may indicate the existence of ferromagnetic clusters inside the film.

(6) The ferromagnetism can be realized for $Ge_{1-x}Mn_xTe$ $0.14<x<0.98$ thin films. We determine the Curie temperature T_C using the data in the ordered region. The T_C value increases with the increase of Mn composition and shows a maximum value around 150 K at x=0.55 and beyond this point it decreases. The dependence of T_C on x tends to follow a quadratic behaviour, which ascribes to the increase of the antiferromagnetic interaction between the Mn ions and ZB MnTe phases.

(7) Both the M-H and M-T curves have been measured with magnetic field applied parallel and perpendicular (H ⊥ plane) to the sample plane. We do not observe distinct magnetic anisotropy, which indicate that the magnetic moments are not all in-plane but part of them are out of plane. The existence of the out-plane magnetic moments could be due to the surface roughness which may induce spin disordering in the film surface.

(8) The carrier concentration of $Ge_{1-x}Mn_xTe$ films ($0.14<x<0.98$) are in the range of 1×10^{20} cm^{-3} to 1×10^{22} cm^{-3} and tend to be on the metallic side of the metal-insulator transition according to Mott's criterion. The temperature-dependent resistivity ρ(T) measurement exhibits an upturn at low temperature, which could relate to the ferromagnetic-paramagnetic (FM-PM) transition. At low temperature range, the hopping conduction tends to dominate the resistivity behavior.

(9) The observed AHE of $Ge_{1-x}Mn_xTe$ thin film is the combination of the carrier-induced ferromagnetism with the effect of the clusters. To ascertain

the origins of AHE, we examine the scaling relationship $\rho_{xy} \propto \rho_{xx}^{n}$ at 20 K, for $Ge_{1-x}Mn_xTe$ with x ranging from 0.14 to 0.98. The behavior of AHE could be due to hopping transport or extrinsic skew scattering.

(10) Our magnetoresistance (MR) measurement displays very clear hysterestic loop at low temperature which reseumbles that of giant-magnetoresistance (GMR) granular system in solids. The negative MR behaviors may be accounted for the BMPs model. We correlate the observation of the isotropy of MR and M-H curves with the formation of $Ge_{1-x}Mn_xTe$ FM clusters embedded in GeTe matrix.

(11) Compared with the previous work, we successfully grow $Ge_{1-x}Mn_xTe$ with Mn solubility up to 98% by MBE growth method for the first time. The lattice constant deduced from XRD experiment is consistent with Fukuma's fitting line, revealing the similar crystalline properties of the films. The HRTEM pictures of the Ge1-xMnxTe are reported for the first time and show the crystalline but nonuniformity in the film so that the magnetic properties of our samples can be linked with the structural properties of the film. The dependence of Curie temperature on the Mn composition for our samples show the similar trend as Fukuma's result that it reaches the highest value when x~0.5. Moreover, in the thesis, the disorder and clustering effects are first discussed with the evidence of structural, magnetic and transport measurement, which are rarely reported in the previous work.

7.2 Recommendations

Recommendations for future work are as follows:

(1) To study magnetic and transport properties of MBE grown $Ge_{1-x}Mn_xTe$ thin films with low Mn concentrations ($x<0.1$). Although some preliminary results have been published by other groups, detailed studies of magnetic and transport properties have not been done yet. This would require the further decrease of the Mn cell temperature.

(2) To improve the structural quality of the film so that to avoid the cluster effects in the films. Current ferromagnetic properties of $Ge_{1-x}Mn_xTe$ thin films in this thesis are observed coming from the combination of the carrier-induced ferromagnetism with the effect of the clusters. It would be good to analyze these two effects separately. The structural uniformity can be improved by optimizing the growth conditions. It requires more accuracy control of the flux and growth temperature during the film growth.

(3) To study the effects of the carrier concentrations on the ferromagnetism of the $Ge_{1-x}Mn_xTe$ thin films. It is known that the carrier concentrations of a film can be changed through annealing. It would be interesting to study the properties of same sample with different carrier concentration before and after annealing.

(4) To investigate the phase change properties of the $Ge_{1-x}Mn_xTe$ thin films. It is well known that GeTe has a fast phase change feature and different optical and electrical properties between amorphous and crystalline states. Thus, it

has been widely used in rewritable optical data storage such as DVD and phase change random access memory (PCRAM). If adding a new degree of freedom associated with the spin of carriers in this phase change material, it may have magnetic property leading to a new application in data storage and multi-functional spintronic devices. We can investigate different optical and electrical properties between amorphous and crystalline states of the $Ge_{1-x}Mn_xTe$ ferromagnetic thin films.

(5) To further fabricate spin valves structure using the $Ge_{1-x}Mn_xTe$ and MnTe layers since one is ferromagnetic material and the other is an antiferromagnetic material. It requires the very smooth interface between these two layers. Therefore, the surface roughness of the grown films needs to be improved.

List of Publications

Journal articles:

1. "Diluted magnetic semiconductor $Ge_{1-x}Mn_xTe$ films prepared by molecular beam epitaxy" W. Q. Chen, K.L. Teo, M.B.A. Jalil, Y.F. Liew and T.C. Chong, Thin Solid Films, **505**, 145 (2005).

2. "Compositional dependencies of ferromagnetic $Ge_{1-x}Mn_xTe$ grown by solid-source molecular-beam epitaxy", W. Q. Chen, K. L. Teo, M. B. A. Jalil, and T. Liew, J. Appl. Phys. **99**, 08D515 (2006).

3. "Magnetic and transport behaviors in $Ge_{1-x}Mn_xTe$ with high Mn composition"， W. Q. Chen, K. L. Teo, S. T. Lim, M. B. A. Jalil, T. Liew, and T. C. Chong, Appl. Phys. Lett. **90**, 142514 (2007).

4. "$Ge_{1-x}Mn_xTe$ ferromagnetic semiconductors grown by solid-source molecular-beam epitaxy", W. Q. Chen, S. T. Lim, C. H. Sim, J. F. Bi , K. L. Teo , T. Liew and T. C. Chong, submitted to Journal of applied physics (2008).

Conference Presentations:

1. "Dilute magnetic semiconductor $Ge_{1-x}Mn_xTe$ films prepared by molecular beam epitaxy technique", W. Q. Chen, K. L. Teo, M. B. A. Jalil, Y. F. Liew and T. C. Chong, 3rd International Conference on Materials and Advanced Technology , July 3-8, 2005, Singapore.

2. "Molecular-beam epitaxial growth of dilute magnetic semiconductor $Ge_{1-x}Mn_xTe$ films" W. Q. Chen, K. L. Teo, M. B. A. Jalil, Y. F. Liew and T. C. Chong, Spintech III,

August 1-5, 2005, Awaji Island, Japan.

3. "Compositional dependencies of ferromagnetic $Ge_{1-x}Mn_xTe$ grown by solid-source molecular-beam epitaxy", W. Q. Chen, K.L. Teo, M. B. A. Jalil, T. Liew and T.C. Chong, 50th Magnetism and Magnetic Materials Conference, Oct 30-Nov 3, 2005, San Jose, California, USA.

4. "The effect of annealing on magnetic properties of $Ge_{1-x}Mn_xTe$ thin films grown by molecular-beam epitaxy", W. Q. Chen, K.L. Teo, M. B. A. Jalil, T. Liew and T.C. Chong in 28th International Conference on the physics of semiconductors, July 24-28, 2006, Vienna, Austria.

5. "Magnetotransport studies in ferromagnetic $Ge_{1-x}Mn_xTe$", C. H. Sim, W. Q. Chen, S. T. Lim, J. F. Bi, K. L. Teo, T. Liew and T. C. Chong, submitted to International Conference on Electronic Materials, 28th July to 1st August 2008, Sydney, Australia.